

**The Vertical and Temporal Characteristics of Winter Orographic  
Clouds as Assessed by Vertically-Pointing Radar**

by  
Joseph S. Greeson

Department of Atmospheric Science  
Colorado State University  
Fort Collins, Colorado



**Department of  
Atmospheric Science**

Paper No. 368



THE VERTICAL AND TEMPORAL CHARACTERISTICS OF WINTER OROGRAPHIC  
CLOUDS AS ASSESSED BY VERTICALLY-POINTING RADAR

By

Joseph S. Greeson

This report was prepared with support provided by National  
Science Foundation Grants ATM 7819261 and ATM 8109490  
Principal Investigator, Lewis O. Grant

Department of Atmospheric Science  
Colorado State University  
Fort Collins, Colorado

May 1983

Atmospheric Science Paper No. 368



## ABSTRACT

This study uses data from three vertically-pointing radars with different wavelengths to describe the vertical and temporal characteristics of mountain clouds during winter storms. Corresponding patterns of radar reflectivity, upper air temperatures and surface precipitation are displayed for six storm cases. In one study Doppler data was used to develop profiles of vertical motion. These Doppler profiles of vertical motion were contrasted to profiles of vertical motion expected from a simple crystal terminal fall velocity profile. The Doppler radar was also used in a Velocity-Azimuth-Display (VAD) mode to determine horizontal air motions at several elevations. In all of these six cases, the highest cloud tops occurred early in the storm with cloud tops lowering in later stages. In two cases the final stage of the storm was characterized by a low cloud regime lasting more than eight hours.

In two case studies, a periodicity within the reflectivity pattern of around two hours suggested the passage of cloud features organized into waves or bands: no evidence of deep or strong instability was associated with these reflectivity patterns.

Persistent downward motions were detected within one storm. These were inconsistent with modelled crystal fall velocities, and were probably representative of sustained downward air motions even at the windward mountain slopes where observed. VAD horizontal wind velocities generally agreed well with rawinsonde determined wind velocities.



During one period of intercomparison, the K-band radar detected cloud top heights above 200 m higher than those determined with the Ku-band, and the Ku-band radar cloud top heights were about 200 m higher than those determined with X-band.

Joseph Greeson  
Department of Atmospheric Science  
Colorado State University  
Fort Collins, Colorado 80523  
Spring, 1983

## ACKNOWLEDEMENTS

The X- and K-band radars used to augment the CSU Ku-band radar in this study were used by permission of NOAA's ERL Wave Propagation Laboratory. Special thanks go to Dr. Faustean Passqualucci and Dr. Robert Kropfli and Dr. William Moninger for their interest and counsel in the completion of this project. A personal note of thanks is extended to all of Professor Lewis Grant's group at Colorado State University, mostly for moral support. Technicians Don Cobb and Randy Horn should be cited for outstanding work in maintaining very complex equipment. Jan Davis did much more than can be recorded here, including typing this report, along with Ruta Radziunas. Lyle Lilley of Science Associates originally assembled the Ku-band radar and provided on-going advice as to its operation. Professor Lewis Grant provided the opportunity for this research and was extremely accomodating in regard to my educational goals. Thanks to Professors William Cotton and William Marshall for serving on the thesis committee and using valuable time to review this manuscript.

Finally, I must reaffirm my individual belief in the Lord God, whose creative hand I saw not only in the lives of the people I worked with, but also in the clouds that I sought to understand.

Research supported by the Experimental Meteorology Program, Division of Atmospheric Sciences, National Science Foundation, Grant No. ATM-7819261.



## TABLE OF CONTENTS

Abstract . . . . .	iii
Acknowledgements . . . . .	v
Table of Contents . . . . .	vi
List of Figures . . . . .	viii
List of Tables . . . . .	xi
I. Introduction . . . . .	1
A. Overview . . . . .	1
B. Focus . . . . .	2
C. Scales of Measurement . . . . .	8
D. Relevant Previous Radar Studies . . . . .	9
E. Objectives . . . . .	13
II. Method . . . . .	16
A. Basic Operational Strategy . . . . .	16
B. Instrumentation . . . . .	19
C. Data Analysis . . . . .	22
III. Results . . . . .	33
A. Objective 1 . . . . .	33
1. Case 1 . . . . .	34
2. Case 2 . . . . .	38
3. Case 3 . . . . .	43
4. Case 4 . . . . .	47
5. Case 5 . . . . .	52
6. Case 6 . . . . .	57
7. Summary of Case Studies . . . . .	63
B. Objective 2 . . . . .	68
1. Vertically Pointing Doppler Observations . . . . .	69
2. VAD Scan Observations . . . . .	81

C. Objective 3 . . . . .	89
1. Aircraft Visual Comparisons . . . . .	89
2. Co-located Radar Cloud Top Observations . . . . .	91
3. Validity of the Rayleigh Approximation . . . . .	93
IV. Conclusions. . . . .	97
A. Major Conclusions . . . . .	97
B. Additional Observations . . . . .	99
C. Suggestions for Future Research . . . . .	100
References . . . . .	103
Appendix I - Derivation of the Radar Equation . . . . .	106
Appendix II - Synoptic Charts and Satellite Photographs for the Six Case Studies under Objective 1 . . . . .	111
Appendix III - Description of the Model Used for Objective 2b. . . . .	136
Appendix IV - CSU's APS-104 Ku-band Radar Calibration . . . . .	141

## LIST OF FIGURES

Figure 1.	Distribution of the concentration of natural primary ice nuclei as a function of environmental temperature . . . . .	3
Figure 2.	Formation of snow in mountain clouds . . . . .	6
Figure 3.	Example of "cell and trail" snowflake trajectories in plane and projected on the vertical . . . . .	11
Figure 4.	Examples of vertical particle velocity profiles as a function of riming . . . . .	14
Figure 5.	The COSE Study Area . . . . .	17
Figure 6.	Basic layout for CSU's Ku-band APS-104 radar and its associated data system . . . . .	20
Figure 7.	Distribution of receiver noise for the Ku-band radar . . . . .	23
Figure 8.	Threshold (minimum detectable) reflectivity as a function of range for the Ku-band radar . . . . .	24
Figure 9a.	Example of reflectivity data printed at one minute intervals . . . . .	26
Figure 9b.	Example of reflectivity data printed at three minute intervals . . . . .	27
Figure 10.	Ku-band radar reflectivity and guage precipitation records for Case 1 . . . . .	35
Figure 11.	Cloud top temperature distribution for Case 1 . . . . .	37
Figure 12a.	Ku-band radar reflectivity and guage precipitation records for Case 2 . . . . .	39
Figure 12b.	Ku-band radar reflectivity and guage precipitation records for Case 2 . . . . .	40
Figure 13.	Cloud top temperature distribution for Case 2 . . . . .	42
Figure 14.	Ku-band radar reflectivity record for Case 3 . . . . .	44
Figure 15.	Cloud top temperature distribution for Case 3 . . . . .	45

Figure 16.	Equivalent Potential Temperature profiles for Case 3 . . .	48
Figure 17a.	Ku-band radar reflectivity and guage precipitation records for Case 4 . . . . .	50
Figure 17b.	Ku-band radar reflectivity and guage precipitation records for Case 4 . . . . .	51
Figure 18.	Cloud top temperature distribution for Case 4 . . . . .	53
Figure 19.	Ku-band radar reflectivity and guage precipitation records for Case 5 . . . . .	55
Figure 20.	Cloud top temperature distribution for Case 5 . . . . .	56
Figure 21.	K-band radar cloud top height and guage precipitation in the period following Case 5 . . . . .	58
Figure 22a.	Ku-band radar reflectivity and guage precipitation records for Case 6 . . . . .	60
Figure 22b.	Ku-band radar reflectivity and guage precipitation records for Case 6 . . . . .	61
Figure 23.	Cloud top temperature distribution for Case 6 . . . . .	62
Figure 24.	Ku-band radar sensitivity loss as a function of height . .	65
Figure 25.	Vertical profiles of $\hat{w}$ and model predicted crystal fall velocities for the first Doppler observation period . . .	70
Figure 26.	Vertical profiles of reflectivity corresponding to periods displayed in Figure 25 . . . . .	72
Figure 27.	Vertical profiles of $\hat{w}$ and model predicted crystal fall velocities for the second Doppler observation period . . .	74
Figure 28.	Vertical profiles of reflectivity corresponding to periods displayed in Figure 27 . . . . .	76
Figure 29.	Vertical profiles of $\hat{w}$ and model predicted crystal fall velocities for the third Doppler observation period . . .	77
Figure 30.	Vertical profiles of reflectivity corresponding to periods displayed in Figure 29 . . . . .	79
Figure 31.	Vertical profiles of horizontal wind <u>direction</u> as assessed by Doppler radar in VAD mode and by rawinsonde for the first VAD period . . . . .	82
Figure 32.	Vertical profiles of horizontal wind <u>speed</u> as assessed by Doppler radar in VAD mode and by rawinsonde for the first VAD period . . . . .	83

Figure 33.	Vertical profiles of horizontal wind <u>direction</u> as assessed by Doppler radar in VAD mode and by rawinsonde for the second VAD period . . . . .	85
Figure 34.	Vertical profiles of horizontal wind <u>speed</u> as assessed by Doppler radar in VAD mode and by rawinsonde for the second VAD period . . . . .	86
Figure 35.	Vertical profiles of horizontal wind <u>direction</u> as assessed by Doppler radar in VAD mode and by rawinsonde for the third VAD period . . . . .	87
Figure 36.	Vertical profiles of horizontal wind <u>speed</u> as assessed by Doppler radar in VAD mode and by rawinsonde for the third VAD period . . . . .	88
Figure 37.	Cloud top heights as determined by co-located X, Ku, and K-band radars . . . . .	92
Figure 38.	Eta values as assessed by K and X-band radars and the ratio of K/X Eta values . . . . .	95

LIST OF TABLES

Table 1.	Altitudes of COSE precipitation guages (inset in Figure 5) . . . . .	17
Table 2a.	Descriptive Radar Parameters . . . . .	21
Table 2b.	Final Form of the Raw Data . . . . .	21
Table 3.	Determination of critical downward velocities below which blowover is feasible at the Highway Camp guage for Case 3 . . . . .	47
Table 4.	Cloud top height visual from aircraft compared to radar . . . . .	90

## I. INTRODUCTION

### A. Overview

This study was conducted over two winter seasons as a component of Colorado State University's Colorado Orographic Seeding Experiment (COSE I and COSE II) in the region near Steamboat Springs, Colorado. The three areas of primary focus in this study were as follows:

- 1) Time variation and characteristic behaviour of cloud top height and cloud top temperature. Cloud top temperature is of interest because it serves as an indicator of microphysical composition, and therefore modification potential within the cloud.
- 2) Vertical velocities of crystals. Assessing vertical crystal velocities is important in estimating the relative roles of environmental motion and crystal fall velocity in the final trajectory of the crystal.
- 3) Time variation and characteristic behavior of zones of relatively high reflectivity ( $>20$  dBz). Radar reflectivity can be shown to be primarily dependent on crystal size, so that zones of high reflectivity should theoretically represent regions of relatively large particles.

Although most of the parameters examined in this study could have been measured or estimated using other instruments, vertically pointing radars were used because of their ability to sample over the entire depth of the cloud and sample over time scales sufficient to cover the entire storm sequences. The radars used in this study were NOAA's X-band (M-33;  $\lambda=3.2$  cm, freq.=9.4 GHz; optional Doppler); CSU's Ku-band (APS-104;  $\lambda=1.8$  cm, freq.=16.7 GHz); and NOAA's K-band (TPQ-11;  $\lambda=0.8$  cm,

freq.=37.5 GHz). In this report, the radars will be referred to as the X-band, Ku-band, and the K-band sets, respectively.

## B. Focus

### 1. Cloud top temperature

The association between cloud top temperature and cloud composition is related to the number and size of ice crystals contained in the cloud. The number of natural ice nuclei which can be activated has been found to be on exponential function of temperature, which varies somewhat according to location (see Fig. 1). Therefore, the temperature of the coldest portion of the cloud can be used as an indication of the number of natural ice nuclei which have been activated and are already available for ice crystal growth within the cloud. The coldest portion of a cloud is usually its highest vertical extent. The point at which radar return signal falls below a certain threshold value is assumed to be near the maximum vertical extent of the cloud. (The goodness of this assumption varies with individual radar sets, primarily as a function of wavelength). Note that the direct relationship between cloud top temperatures and concentrations of ice crystals may break down under conditions suitable for significant ice multiplication, if and when these conditions occur.

The concentration of ice crystals in cloud is an important factor in the production of precipitation from the cloud. Bergeron (1933) and Finndeisen (1938) postulated that the more rapid growth of ice particles relative to supercooled water droplets led to the dominance of the ice phase in precipitation processes. Thus a relationship exists between the concentration of ice crystals existing within a cloud and the efficiency of conversion of cloud condensate to precipitation particles.



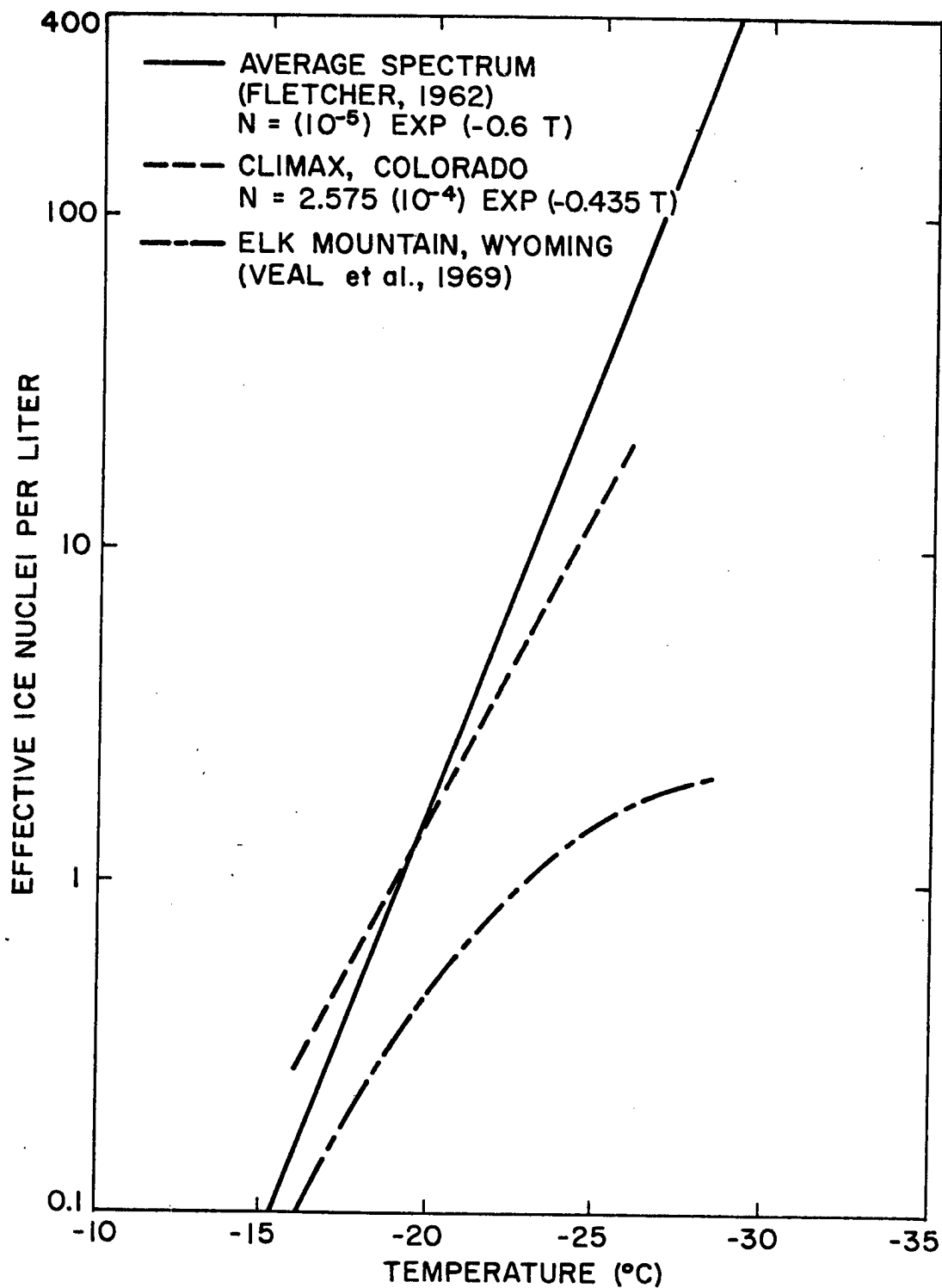


Figure 1. Distribution of the concentration of natural primary ice nuclei as a function of environmental temperature (from Chappell (1970)).

Bergeron (1949) subsequently suggested that under certain conditions the precipitation production of cold orographic clouds could be increased by the introduction of artificial nuclei into the cloud. He indicated that an optimum concentration of ice crystals for precipitation production can be determined, such that the available vapor supply in the cloud would be efficiently consumed. In a case where a deficiency of natural ice crystals exists, the introduction of artificial ice nuclei could serve to restore the optimum crystal concentration for precipitation production. Because the concentration of activated natural ice nuclei is a function of temperature (see Fig. 1), deficiencies in crystal concentrations from the optimum for precipitation production are more likely to exist in clouds whose maximum vertical extent is not in a relatively cold temperature region. Thus, cloud top temperature can also be used as an indication of seedability.

Observations in support of the conceptual connection between cloud top temperature and seedability were reported by Grant and Mielke (1967) in analyzing the results of the Climax randomized orographic cloud seeding experiment. The Climax experimental cases were stratified using the 50 KPa temperature (determined by upwind rawinsonde) as an index for the average cloud top temperature. The largest ratio of seeded to non-seeded precipitation occurred in the warmest 50 KPa temperature category ( $> -20^{\circ}\text{C}$ ), while the experimental cases in the coldest 50 KPa temperature category ( $< -27^{\circ}\text{C}$ ) exhibited seeded to non-seeded precipitation ratios less than one. Grant and Mielke attributed results for the warm cases to an insufficient number of natural ice nuclei existing to efficiently utilize the vapor supply. In the cold cases, a sufficient number of activated natural ice nuclei already existed, and the additional

vapor depletion caused by the introduction of artificial nuclei may have only reduced the size of the precipitation particles; thereby reducing their fall velocities and allowing them to escape the target area.

## 2. Precipitation vertical velocities

The ability to accurately model precipitation fall velocities is also desirable from the perspective of seedability assessment. Ludlam (1955) expanded upon Bergeron's orographic seeding suggestion and began to take into account precipitation particle trajectory. Specifically, Ludlam noted that generating additional ice particles could increase precipitation efficiency only if trajectories of the additional particles impacted the ground in the target area (see Fig. 2). Particles blowing over the ridge crest evaporate or contribute to runoff in a watershed downwind from the target.

Observational support for the importance of particle trajectory in assessing seedability can also be found in the Climax analysis (Grant and Mielke, 1967) as well as the reanalysis of the Colorado River Basin Pilot Project (CRBPP) by Elliott et al. (1978). At Climax the observed seeded increases varied with 70 KPa wind speed and direction. Medium-range 70 KPa wind speeds (12-14 m/s) produced the most significant seeded increases, perhaps indicating an overshooting effect at higher wind speeds and insufficient orographic lift at very low velocities. In the reanalysis of the CRBPP the experimental cases were stratified using a "barrier trajectory index" (BTI). The BTI represents a time difference between the characteristic time during which the artificial ice nuclei can interact with the upslope cloud and the time span for a precipitation particle to fall from cloud top to ground. In general, high

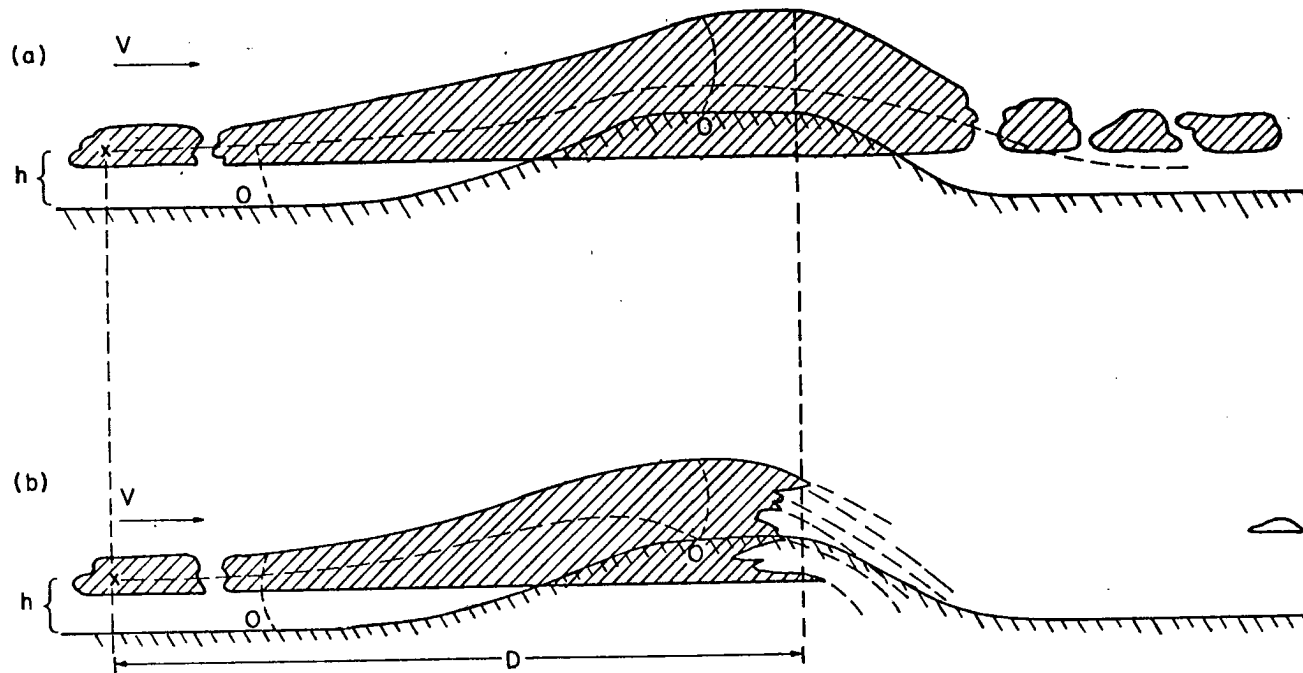


Figure 2. Formation of snow in mountain clouds. An ice crystal forms at height  $h$  above the ground, and horizontal distance  $D$  from the ridge crest. It is advected through the orographic lift region (0-0) with a mean wind speed  $v$ . Depending on the magnitudes of these factors (in addition to the integrated terminal velocity of the crystal), the crystal will either blow over the top of the ridge crest and evaporate (as in a.) or fall as precipitation on the mountain (as in b.). (from Ludlam (1955))

winds and deep clouds generate negative BTI values; while light winds and low clouds create positive BTI values. For the CRBPP data (which was taken in the San Juan Mountains of Colorado), conditions with positive BTI values led to relatively greater increases in seeded precipitation than conditions with negative BTI values for equivalent categories of stability and lifted cloud top temperatures. Again in this experiment, it appears that in conditions allowing significant blowover (Negative BTI), the introduction of artificial ice nuclei could not enhance the efficiency of the precipitation process.

### 3. High reflectivity zones

Another area of focus in this study concerned the location in the vertical and time behavior of relative maxima of radar reflectivity. Because of the nature of microwave reflectivity from particles (see App. I), a relative maximum in radar reflectivity probably arises from the existence of the largest particles rather than the highest concentration of particles. Under conditions in which the Rayleigh approximation is valid (that is, when the diameters of the reflecting particles are much less than the wavelength of the incident radiation), radar reflectivity is proportional to the sixth power of the particles' diameters, and only linearly proportional to the concentration of particles. Thus, for example, a two fold increase in average particle concentration yields a two fold increase in radar reflectivity; while a two fold increase in average particle diameter yields a sixty-four fold increase in radar reflectivity. A relative maximum in the vertical profiles of radar reflectivity in this study, then, should indicate at what level above the radar the largest particles existed.

### C. Scales of Measurement

Although several types of instruments can measure the parameters outlined in the previous section, radar can sample on space and time scales which are inaccessible to other instrumentation systems. Specifically, radar can sample continuously over the entire depth of the cloud during an entire storm sequence.

Aircraft mounted instrumentation have the major advantage of obtaining in situ measurements. Also aircraft mounted instruments can sample directly on scales useful for microphysical studies. However, measurement systems mounted on aircraft usually sample small volumes along horizontal lines; and vertical cloud structure must be obtained by conceptually integrating discrete observations and assuming that the cloud remains steady state in time. Due to safety considerations, aircraft in storm conditions in mountain terrain cannot sample at low altitudes or fly at night. The time during which aircraft can actually sample cloud in one flight is limited by fuel consumption; and this limitation can be particularly severe when the aircraft is based far from the experimental area.

Satellite mounted radiometers can measure cloud-top temperatures directly; in contrast to the radar method of measuring cloud top height and comparing it to the vertical temperature structure taken from rawinsonde data. However, satellite mounted radiometers only detect the temperature at the top of the uppermost cloud deck; which, in the case of intervening cirrus, may not be the deck of interest. Conventional satellite instrumentation cannot yield data pertinent to in-cloud structure. Commonly available satellite data have minimum horizontal resolution on the order of a few square kilometers.

The advantages gained by radar in space and time scales of measurement are partially offset by the problems and costs in reducing the huge resultant volumes of data. In this experiment, for example, CSU's Ku-band radar recorded in digital form  $1.1 \times 10^6$  data points per hour while in a mode sampling every 30 seconds. Unlike other methods of measurement, radar systems can maintain this sampling density for many hours, making the cost of data reduction considerable.

#### D. Relevant Previous Radar Studies

##### 1. Radar Observations of Snow Patterns

The earliest extensive observations and analyses of snow by radar were performed by scientists at McGill University in the region near Montreal. One of these studies (Douglas et al., 1957) used vertically pointing X-band radar to describe characteristic features in snow producing clouds associated with fronts near Montreal. They noted and interpreted two major patterns.

a. "Stalactities" or downward protrusions of cloud base. These appeared near the onset of the storm and were associated with crystals falling into a region subsaturated with respect to ice.

Evaporative cooling was thought to have created an unstable layer below the region of evaporation causing convective overturning.

b. "Cell and trail" precipitation. Cellular snow generating regions had been identified in previous McGill University radar studies in the vicinity of Montreal (Marshall, 1953; Gunn et al., 1954; Langleben, 1956). This study postulated that the cells were regions of local turbulence where large collision rates existed. The subsequent "trail" was attributed to agglomerate particles.

The calculated shape of the trail in the horizontal and vertical are given in Fig. 3.

## 2. Reflectivity Patterns in Mountainous Areas

Grant et al. (1965) noted that cellular snow patterns had been easily and consistently observed by X-band radar in the Climax region of the Central Colorado Rockies, sometimes embedded in lighter more widespread precipitation.

Radar patterns produced by storms in the Climax region of the Colorado Rockies were described by Furman (1967). From PPI observation he concluded that the highest reflectivity regions were near ridge and mountain summits. Furman found evidence for convective bands similar to those observed by Elliott and Hovind (1964) using an X-band radar in both a vertically-pointing and a PPI mode. The period of convective bands in this region (Central Colorado) was found to be about 165 minutes.

Yaw (1972) used X-band radar to monitor winter precipitation changes brought about by seeding in the Bridger Mountain Range in southwestern Montana. Using a PPI display, a precipitation "parcel" was observed to persist in a subsidence region which obliterated the "background" precipitation in an area between ridges. In contrast to surface precipitation, Yaw found that precipitation at upper levels is characterized by high variability in time and space. Yaw concluded that only suitably averaged precipitation at upper levels could be used to assess the effects of seeding.



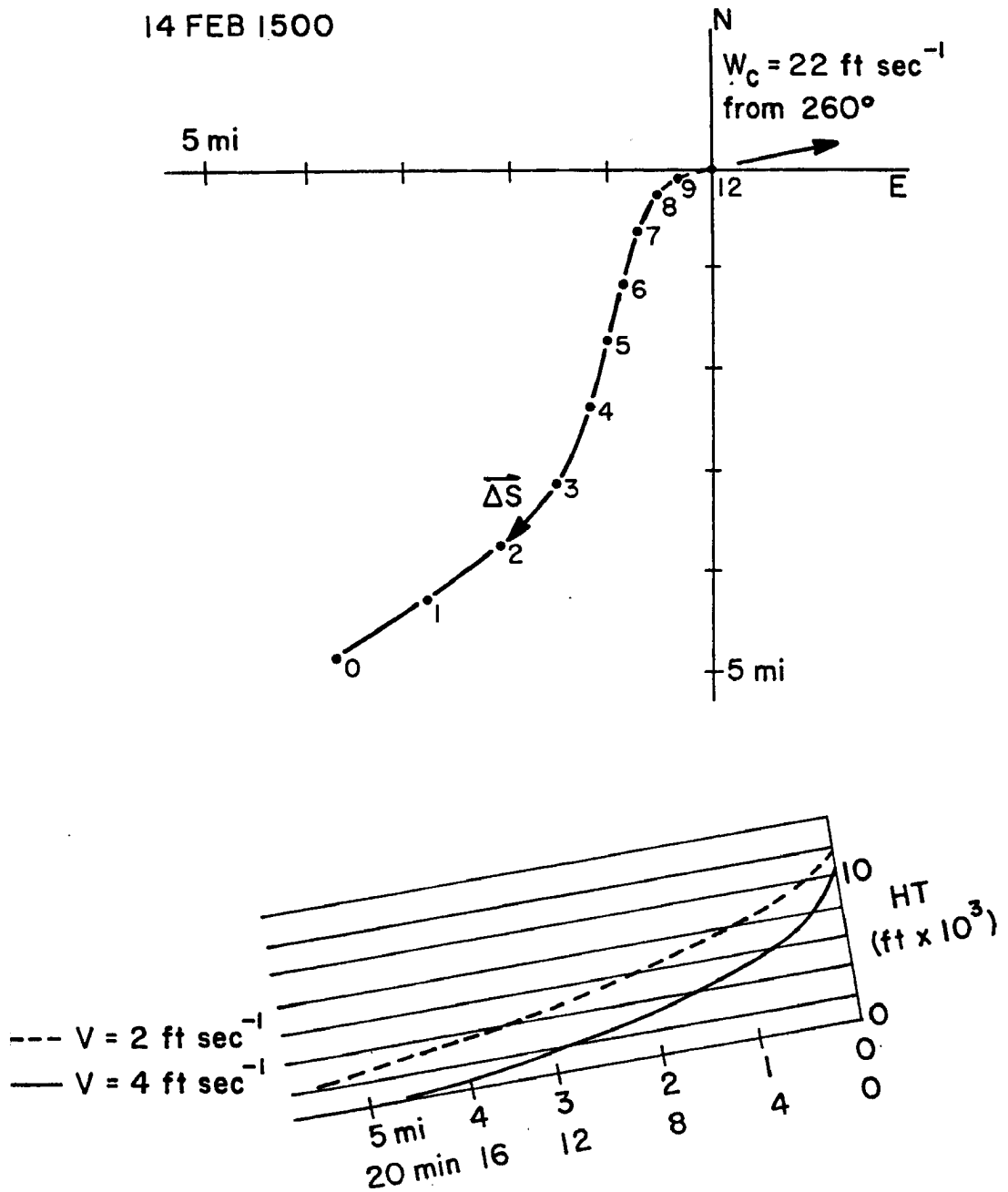


Figure 3. Example of 'cell and trail' snowflake trajectories in plan and projected on the vertical. Top: plan trajectory with constant terminal fall velocity ( $V = 4 \text{ ft sec}^{-1}$ ); heights indicated at thousand foot intervals along the 'trail'. Bottom: projection of plan trajectory on a vertical plane containing cell velocity  $W^c$ .  $\Delta s$  is the displacement vector. (from Douglas et al., (1957))

### 3. Optimum Wavelength

Grant et al. (1965) have indicated the special requirements of radar systems to accurately monitor winter orographic precipitation in the Colorado Rockies. Specifically, they point out that the predominance of ice and small snowfall rates found in the Climax region both allow (from an attenuation perspective) and require (from a detection perspective) short wavelength radar systems. The unique nature of winter orographic storm characteristics in the Colorado Rockies must be taken into account when considering the applicability to the present case of studies made in other locations.

Hartzell and Crow (1976) mention the inadequacy of an X-band radar system for accurately detecting winter orographic cloud tops in the Colorado River Basin Pilot Project in the San Juan Mountains of Colorado. They suggest that the use of the K wavelength would improve the capability to detect cloud top height in the region.

The comparative performances of co-located X-band and K-band radars were assessed by Weiss et al. (1979). This study in the Cascade range in Washington found the X-band wavelength unsuitable for detecting cloud top height, with the X-band radar underestimating cloud top height as detected by the K-band radar by as much as two kilometers. The authors point out that particularly in weather modification research, the X-band wavelength has been widely used for cloud top height detection. Below the "bright band" region the X-band data was concluded to be superior because of the validity of the Rayleigh approximation and less attenuation effects at the longer X-band wavelength. The melting region associated with the radar bright band is not commonly observed in winter storms in the Colorado Rockies.

#### 4. Doppler Studies of Winter Orographic Precipitation

Vertically-pointing pulsed Doppler radar was used by Hobbs et al. (1975) in the Cascades to determine particle fall velocities under conditions when the environmental vertical velocities were considered negligible. Calculated profiles of vertical velocities were constructed by integrating the appropriate growth equations in conditions representative of different growth environments (see Fig. 4). A significant difference in line slopes between particles growing primarily by riming was evident. Using this model, riming (deduced from Doppler observed vertical velocity profiles) was found to decrease during a period which was known to be seeded.

Moninger (1980) summarized the initial results from triple-Doppler observations of winter storms in the Sierras. He concluded that (contrary to observations of summer convective storms on the High Plains) high reflectivity regions were strongly correlated to updraft regions.

#### E. Objectives

In view of the research to date, the major objectives of this study were as follows:

1. To investigate the behavior of cloud top and regions of high reflectivity in the domains of space, time, and temperature.
2. Estimate vertical and horizontal motions in cloud from a knowledge of cloud particle movement.
3. To observe differences in echo detection patterns among three colocated radar sets, differing primarily in wavelength ( $\lambda=3.2$  cm, 1.8 cm, and 0.8 cm).

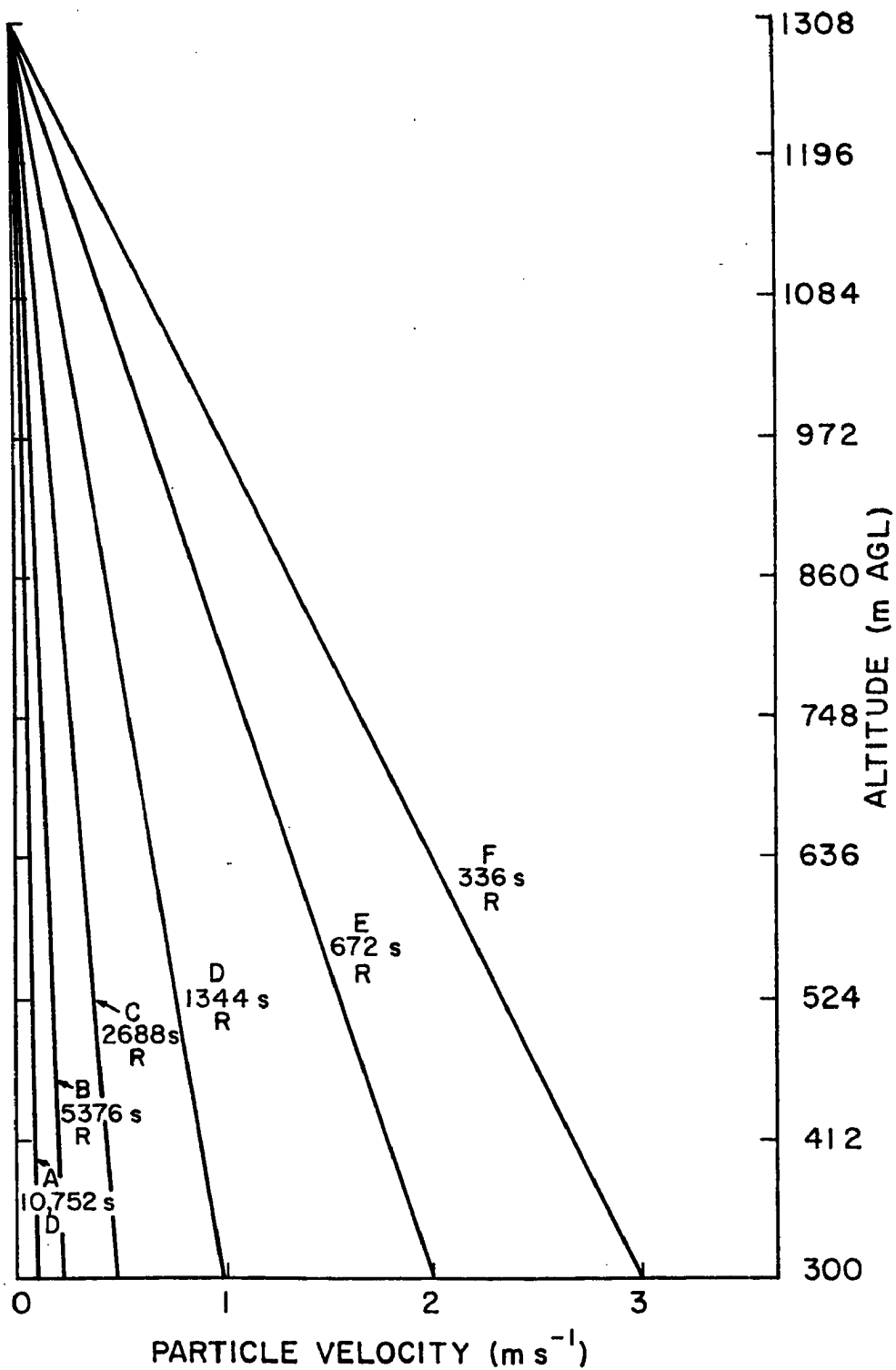


Figure 4. Examples of vertical particle velocity profiles as a function of riming. Curve A is an example of diffusional growth (D) while the remaining curves represent progressively higher riming rates (R). Below each label is the calculated time necessary in seconds for the particle to impact the ground from a height of 1308 m AGL. (from Hobbs et al., 1975)

To achieve the above objectives, the study was constructed around nine subobjectives:

- 1-A. To define the continuous variation of cloud top height as assessed by cloud wavelength (Ku or K-band) radar for six orographic storm periods.
- 1-B. To examine cloud top temperature for the six case studies by comparing the radar-derived cloud top heights with the rawinsonde-derived temperature field.
- 1-C. To perform similar height-temperature analysis for zones of relatively high reflectivity ( $> 20$  dBz).
- 1-D. To compare vertically-pointing radar records to hourly precipitation data taken at 6 gauges distributed at various elevations over the barrier.
- 2-A. To construct vertical profiles of downward particle velocity for one storm case from vertically-pointing Doppler radar data and estimate the impact of the dynamic component on observed fall velocity.
- 2-B. To construct vertical profiles of horizontal velocity by using the Doppler radar in VAD (Velocity-Azimuth-Display) mode and compare the profiles to those obtained from an upwind rawinsonde.
- 3-A. To compare Ku, K, and X-band detected cloud top heights to aircraft observations.
- 3-B. To examine the differences in detected cloud top height and temperature as detected by the three radar sets for one storm case.
- 3-C. To identify areas of non-Rayleigh returns as determined by the K-X-band ratio of radar reflectivity factor.

## II. METHOD

### A. Basic Operational Strategy

The radars used in this project were installed as a component of CSU's Colorado Orographic Seeding Experiment (COSE) in the vicinity of Steamboat Springs in northwestern Colorado. The placement of the radars at the base of Mt. Werner near Steamboat Springs ski area was chosen primarily in an effort to monitor the cloud which would produce the precipitation that actually impacted on the windward side of the ridge (see Fig. 5). Placement farther up the ridge may not have sufficiently monitored the zones of origin for the precipitation which fell on the ridge. CSU's Ku-band radar was operational at the ski area site 26 January to 3 March 1979, and again 7 December to 17 December 1979. The Ku-band set was moved to the Milner site 17 December 1979 and was operational there until 23 December 1979. NOAA's K-band and X-band radars were operational at the ski-area site 25 November to 23 December 1979.

The method for achieving Objective 1 (Examining space, time and temperature variability of cloud top and regions of high reflectivity) was to first gather digital reflectivity data using the Ku-set in a vertically pointing mode. The data was then displayed in a time series made using a cloud boundary finding routine, and contoured to reveal reflectivity patterns within the cloud. Vertical temperature fields were constructed using data from rawinsondes launched at Craig (see Fig. 5). When overlaid, the graphical representations indicated the temperature at cloud top level and at levels within the highest reflectivity contour.

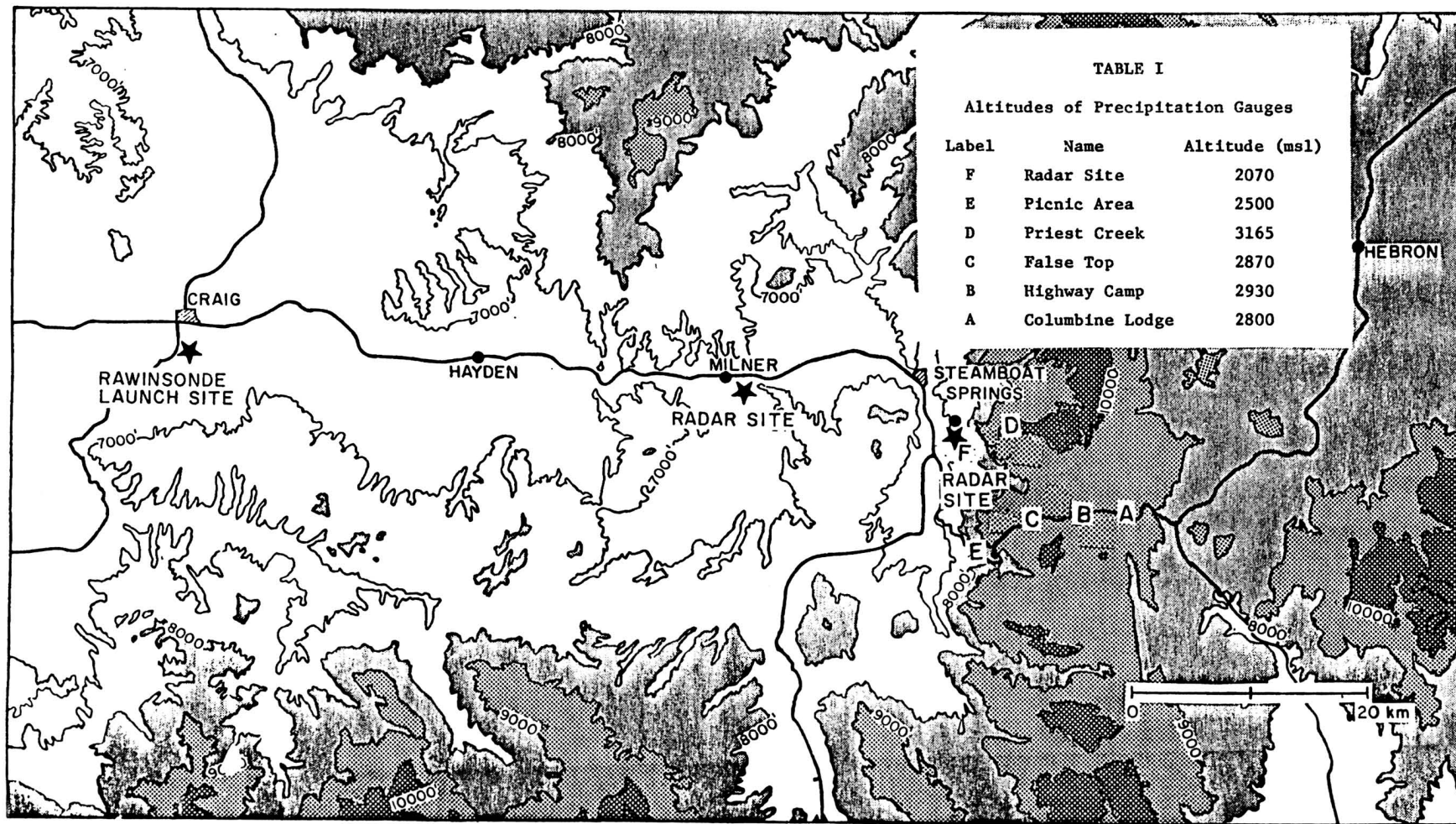


Figure 5. The COSE study area. Letters correspond to precipitation gauges listed in inset.

The data for Objective 2 (Estimating vertical and horizontal motions in cloud) was obtained using the X-band set in Dopplerized mode and processed using a pulse pair algorithm. Vertical profiles of vertical velocity were obtained while the dish was locked in vertically-pointing mode. The profiles were then compared to model-derived crystal fall velocities to estimate the magnitude of dynamic effects. Vertical profiles of horizontal velocity were obtained using VAD (Velocity-Azimuth-Display) processing from data obtained while the dish was scanning conically. The VAD profiles were then compared to vertical profiles of horizontal velocity derived from rawinsonde data.

The conclusions for Objective 3 (Observation of differences in echo detection patterns among three different wavelength radars) were based on three kinds of analyses:

1. A comparison of cloud top height detection levels for each radar set during a brief period when all three radars were colocated and operational.
2. A comparison of Ku-detected cloud top heights with visual reports from aircraft.
3. Identification of non-Rayleigh regions in the cloud accomplished by ratioing the effective radar reflectivity factors as detected by the X-band and K-band sets and comparing the ratio to the theoretical value for a true Rayleigh scattering region.

Six different storm cases during 1979 were examined for Objective

1. The storm of 10 and 11 December 1979 contained the most extensive Doppler coverage and was therefore selected for study under Objective 2. Data was drawn from a survey of the six cases described above as well as the storm of 10-11 December for Objective 3.



## B. Instrumentation

The essential characteristics of each radar set used in this study are given in Table 2a. A diagram of the layout of the Ku radar set and its data system is given in Fig. 6. Although the radars differed in several aspects, the most significant difference among the sets regarding sensitivity is wavelength. The relationship between wavelength and sensitivity is illustrated along with the derivation of the radar equation in Appendix I. Although shorter wavelength radars tend to be more sensitive, their use is limited to conditions which do not result in large attenuation and under which the Rayleigh approximation generally is valid. Conditions in winter orographic clouds in the Rocky Mountains are generally characterized by relatively low liquid water contents and relatively low precipitation rates (Grant et al., 1965; Walsh, 1977). Since, for a given radar set, attenuation is proportional to liquid water content and precipitation rate, attenuation can be shown to be negligible for each of the frequencies used in this study. Under summer conditions, or in other regions, attenuation from larger precipitation rates, higher cloud liquid water contents, and greater path lengths might severely limit the use of shorter radar wavelengths.

The final resolution of the raw data for each radar set is given in Table 2b. NOAA's X and K-band radars shared a single data processing system. Non-Doppler data from the X-band set was recorded simultaneously with K-band data; however, the data system could not record K-band data while the X-band set was operating in Doppler mode. Because of the resolution of data in both space and time, considerable reduction of the data was necessary to produce a meaningful overview of the storm periods.

APS - 104

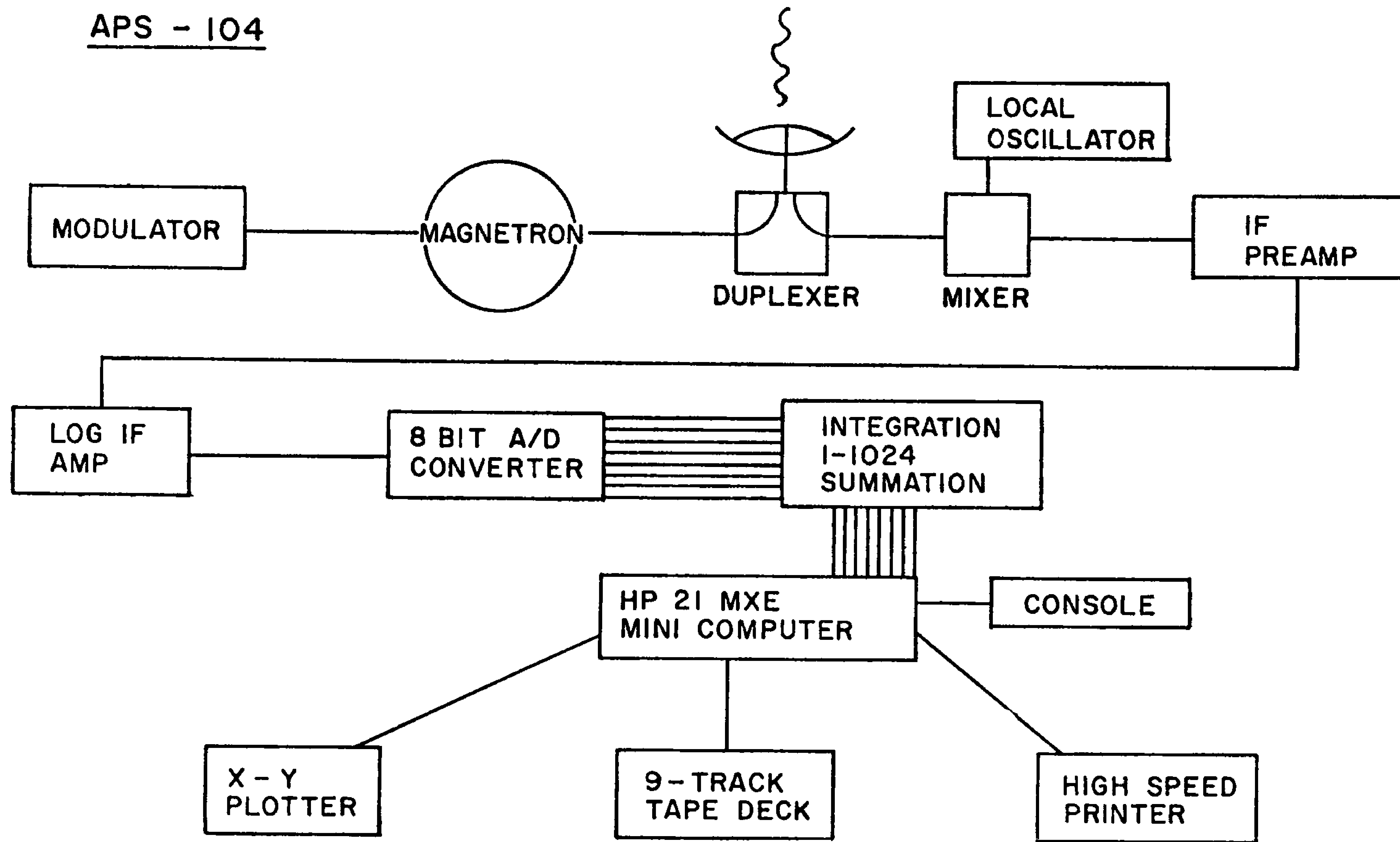


Figure 6. Basic Layout for CSU's Ku-band APS-104 radar and associated data system.

Table 2a.  
Descriptive Radar Parameters

	X-band	Ku-band	K-band
Wavelength (cm)	3.22	1.8	0.86
Frequency (GHz)	9.3	16.7	34.9
Power transmitted (KW)	25	120	120
$P_r$ (dBm) *	-103	-100	-99
$\eta$ (Eta) ( $m^{-1}$ ) *	$1.9 \times 10^{-11}$	$2.1 \times 10^{-11}$	$2.2 \times 10^{-11}$
$C_n^2$ ( $cm^{-2/3}$ ) *	$7.2 \times 10^{-13}$	$6.6 \times 10^{-13}$	$5.4 \times 10^{-13}$
$z$ ( $mm^6 m^{-3}$ ) *	$7.15 \times 10^{-2}$	$7.7 \times 10^{-3}$	$4.2 \times 10^{-4}$
$\tau$ (pulse length) (microsec $^{-1}$ )	0.5	1.0	0.5
Antenna diameter (m)	3.05	2.14	2.14
Antenna configuration	movable	fixed vertical	fixed vertical bistatic
Beam width ( $^\circ$ )	0.86	0.59	0.25

\* Minimum Detectable

Table 2b.  
Final Form of the Raw Data

	X (non-Doppler) and K-band	Ku-band
Number of pulses per sample	64	46
Time intervals between samples (sec)	10	60 or 30
Range bin size (m)	75	50
Range in the vertical (km)	10	10
Number of range bins	selectable	200

An RD-65 rawinsonde unit was installed at Craig airport (see Fig. 5) during the COSE experimental period. Rawinsondes were launched every 12 hours during clear periods and every 3 hours during storms.

### C. Data Analysis

To achieve Objective 1 (Examining space, time, and temperature variability of cloud top and zones of higher reflectivity) it was necessary to distinguish between meteorological return and system noise in the radar data. For the Ku set, this was done in the following manner. Continuous wave signal was injected into the receiver-data system complex and attenuated until the digital output was no longer dependent on attenuation. The digital output at this point was considered to be entirely due to system noise. The average and standard deviation for this digital output for 398 range bins during 46-pulse samples were determined (see Fig. 7). In order to be consistent with the analysis algorithms for the K and X-band sets, a threshold value of three standard deviations above the mean digital value was set as the demarcation between meteorological return and system noise. (dashed line in Fig. 7). After conversion to dBz, this threshold value is range dependent as is illustrated in Fig. 8.

Having chosen a threshold for designating cloud boundaries, a method to display the data in time series was constructed. Although CSU's Ku-band radar was equipped with a data system which was capable of recording in 50 meter range bins, the data was displayed in 100 meter range intervals for economy of space. Reflectivity values were displayed only if the reflectivity exceeded the threshold value for a corresponding range and an adjacent 50 meter range bin exceeded

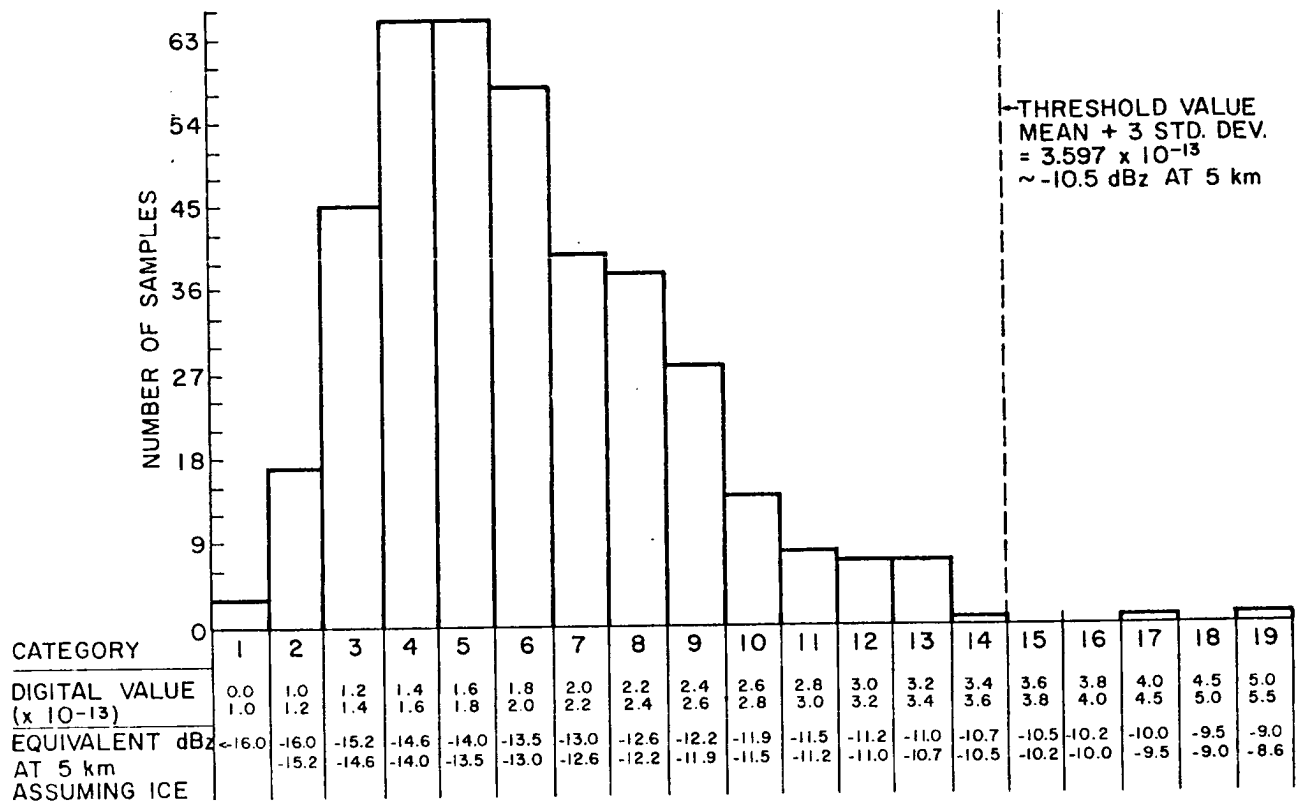


Figure 7. The sampled distribution of receiver noise for the Ku-band radar in digital integrator values and dBz values assuming ice at 5 km. Dashed line represents threshold value for discriminating between meteorological return and system noise.

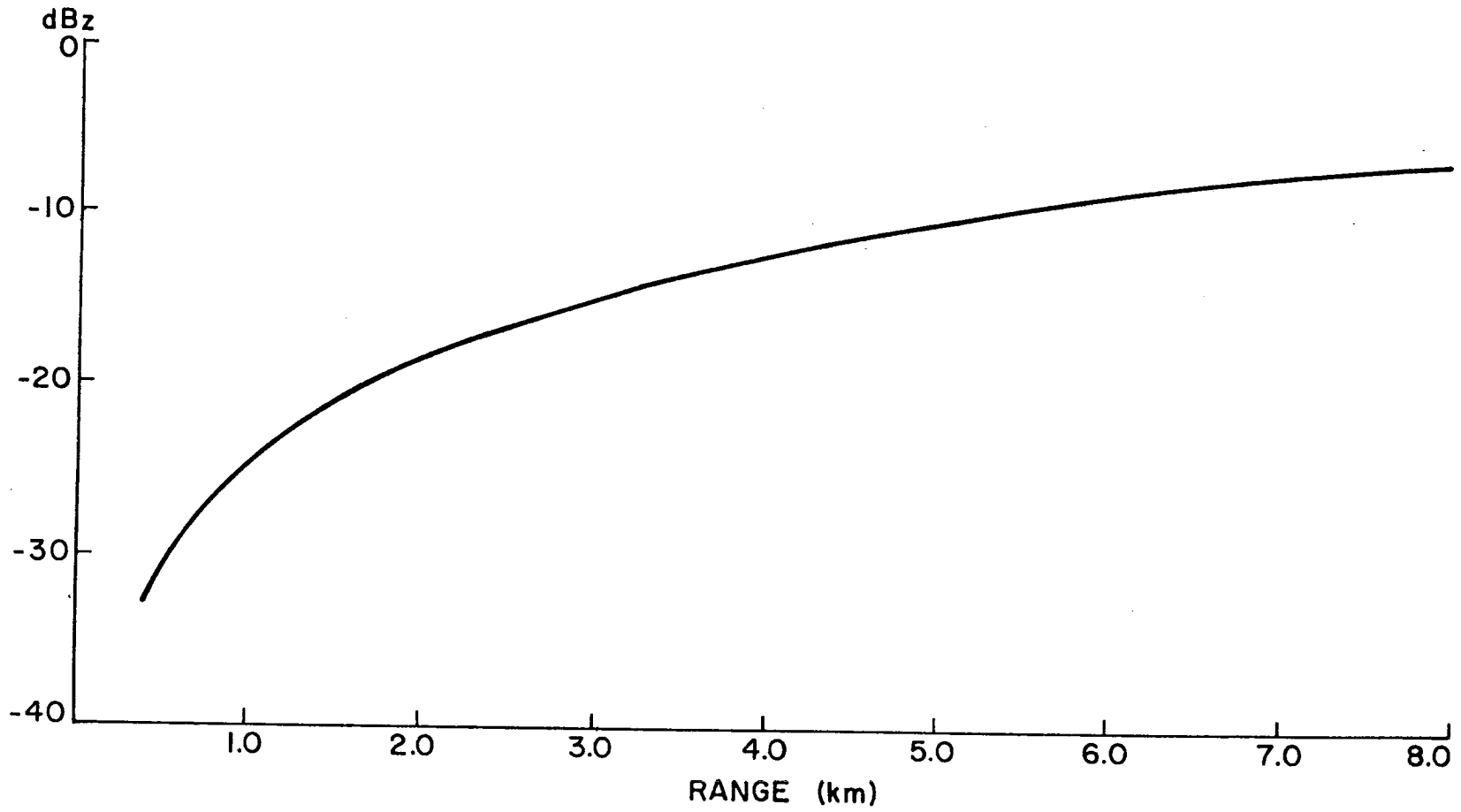


Figure 8. Minimum detectable (threshold) reflectivity as a function of range for CSU's Ku-band radar.

threshold value. Isolated range bins exceeding threshold value were not displayed because most of them probably represented noise instead of small scale ( $< 100$  m) meteorological features. Using this display routine, meteorological information may have also been eliminated, but the characteristic scale of this information was probably not critical to this study.

The Ku-band radar recorded data every 60 seconds or, in some cases, every 30 seconds. Again, in an effort to present the data in a more concise form, data were displayed in three-minute intervals. As can be seen from a comparison of Figures 9a and 9b, data displayed in the three-minute interval mode retained the primary features of cloud top change as indicated by the one-minute interval mode. The period presented on February 23, 1979 was the most extreme in temporal variation.

In interpreting the data displayed in this way, the reader should be cautioned that it is only representative of a time series of vertical structure. It is tempting to mentally transform the axes on the graphical display into height and horizontal distance instead of height and time. The graphs do not represent "snapshots" of the actual two-dimensional cloud appearance except in the vertical dimension. The actual morphology of the clouds can only be deduced by realizing that the graphs depict cloud features which are advected over a point on the ground. Thus the apparent "horizontal distances" will be distorted depending on the choice of time interval for display and, to a lesser extent, on the advection speed (environmental wind speed). The degree to which the choice of time interval selected for the graphical display affects the apparent shape of the "horizontal features" in the cloud

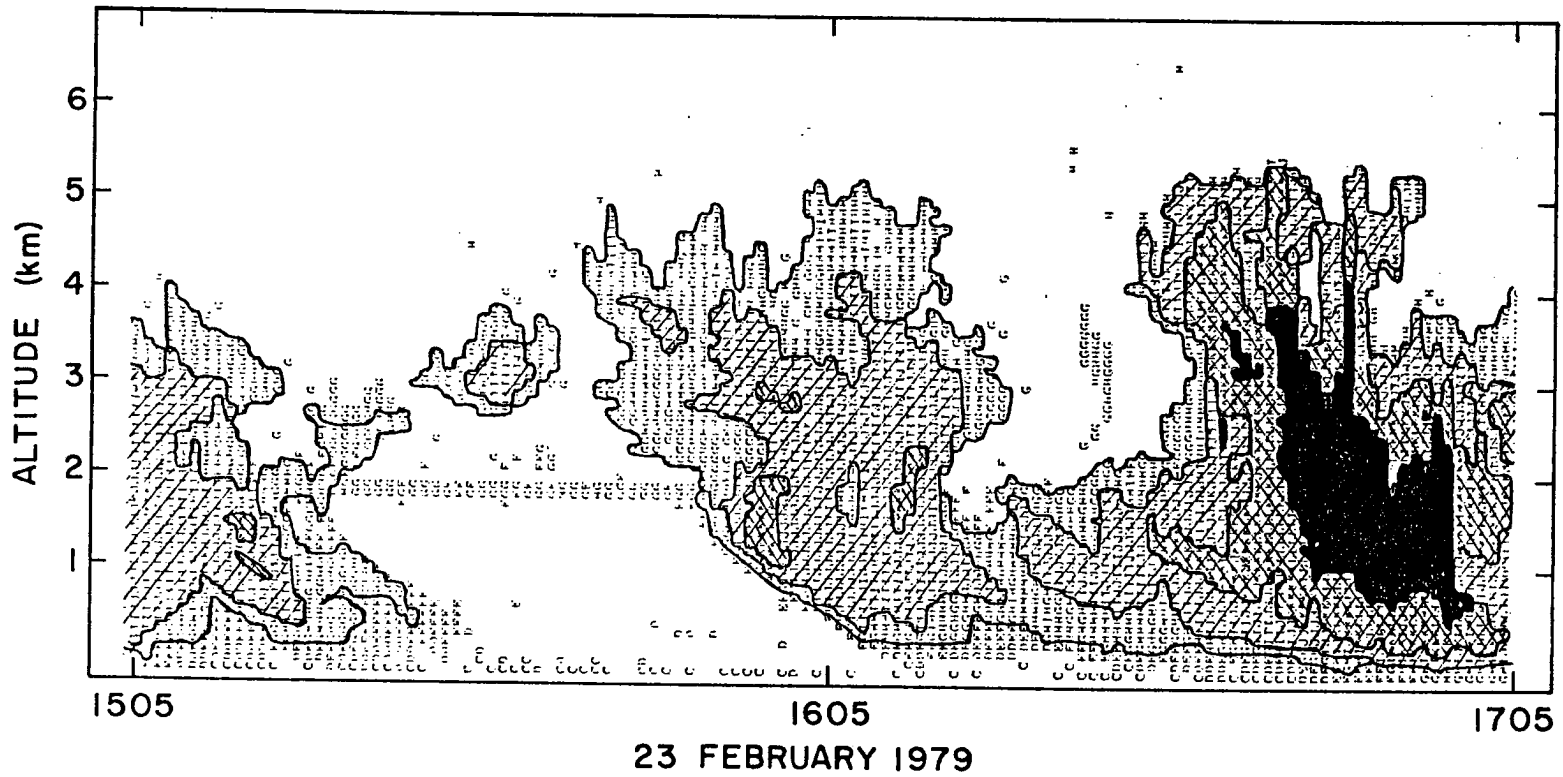


Figure 9a. Reflectivity data printed with each vertical line representation a one-minute interval from the storm of 23 February 1979, 1505 - 1705 MST.



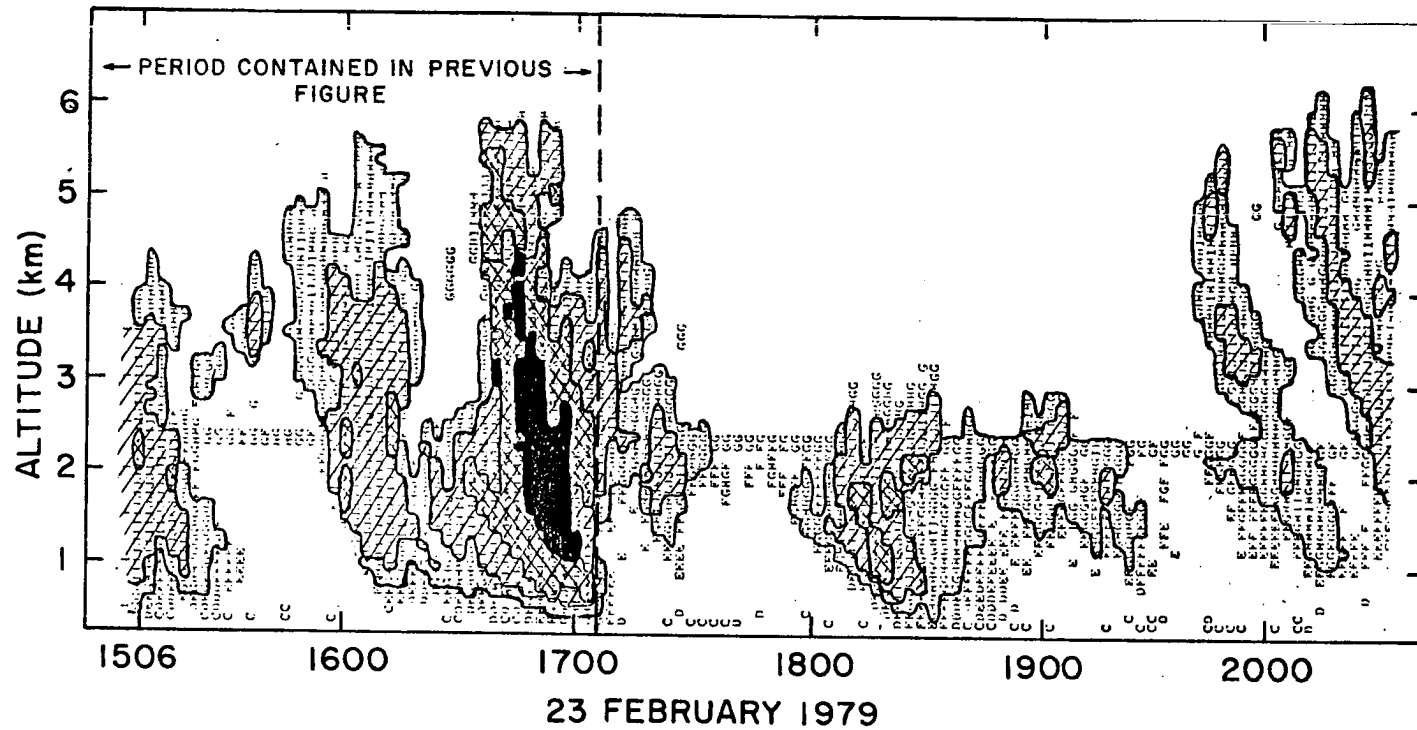






Figure 9b. Reflectivity data printed with each vertical line representing a three-minute interval from the storm of 23 February 1979, 1506 - 2033. The period to the left of the dashed line is represented in fig. 9a.

can also be seen in a comparison of Figures 9a and 9b, in which a three-fold change in time interval is represented.

Reflectivity values which exceeded the meteorological threshold were assigned a certain letter value according to the following scheme:

<u>Reflectivity in DBz</u>	<u>Letter Value</u>
-35 < Z ≤ -30	B
-30 < Z ≤ -25	C
-25 < Z ≤ -20	D
-20 < Z ≤ -15	E
-15 < Z ≤ -10	F
-10 < Z ≤ -5	G
-5 < Z ≤ 0	H
0 < Z ≤ 5	I
5 < Z ≤ 10	J
10 < Z ≤ 15	K
15 < Z ≤ 20	L
20 < Z ≤ 25	M
25 < Z ≤ 30	N

If reflectivity in an adjacent 50-meter range bin also exceeded the threshold value (see previous paragraph) the letter for the original range bin was printed in display. For quick interpretation, isoechoes were superimposed by hand in intervals of 10 dBz and the enclosed areas were shaded according to the following scheme:

<u>Reflectivity in DBz</u>	<u>Shading</u>
$-10 < Z \leq 0$	
$0 < Z \leq 10$	
$10 < Z \leq 20$	
$20 < Z$	

Time series consisting of hourly observations of precipitation from functional COSE precipitation gauges were displayed below the radar reflectivity time series. The data from the precipitation gauges are ordered to yield a profile of distribution across the main barrier.

When the reflectivity data had been displayed the vertical temperature field was determined and superimposed. The vertical temperature field was constructed from data taken by the rawinsondes launched at Craig. While attempting to develop a suitable method for adjusting the temperature values to be representative of the vicinity of the radar the following observations were made:

1. Simply lifting the entire airmass by the elevation difference between the Craig rawinsonde launch site and the radar site (cooling all levels by the corresponding adiabatic lapse rate) would result in less than a  $2^{\circ}\text{C}$  change because the net elevation difference was less than 200 meters.

2. Spot checks of aircraft data at several levels over the radar did not support a consistent interval between the rawinsonde and radar sites in temperature. Occasionally temperatures over the radar site were actually warmer than those measured by rawinsonde for the same level at the same time. Generally, the observations agreed to within  $3^{\circ}\text{C}$ .

3. The actual amount and vertical distribution of lift between the sites is a function of the flow characteristics of a valley area west of a major barrier. The flow characteristics of such a region are not yet well understood.

4. At upper levels, the prevailing winds would most often carry the rawinsonde balloon close to the vicinity of the radar.

Based on these observations it was concluded that the unmodified temperatures taken from the rawinsonde would probably be as representative of temperatures over the radar site as a subjectively adjusted temperature field, therefore the actual temperature levels as sampled by rawinsonde are displayed. Temperature levels are indicated in 5°C intervals on the displays at times corresponding to rawinsonde launch times. Isotherms were drawn based on a linear interpolation between launch times. Histograms of the distribution of cloud top temperature for each case study were constructed.

The main analysis technique for Objective 2 (Estimating vertical and horizontal motions in cloud from cloud particle movement) was to display vertical profiles of vertical velocity above the radar for various times during the storm of December 10 and 11, 1979. The profiles represent five minute averages of samples recorded at ten second intervals. The data were averaged to reduce the effect of motions of characteristic time scale much less than five minutes. Vertical profiles of reflectivity obtained from the Doppler data and averaged over the corresponding five minute sample periods were also displayed. Since reflectivity is critically dependent on crystal size (see Appendix I,  $\Sigma nD^6$ ), a comparison of the vertical reflectivity profiles and the vertical velocity profiles would indicate to what extent the shape of the

vertical velocity profiles were influenced by the vertical distribution of average crystal size. The periods selected for analysis were intervals of approximately 30 minutes during which the radar was operating in Doppler mode.

An attempt was made to estimate the contribution of the average terminal fall velocities of the crystals compared to the environmental flow component of vertical velocity. This was done by superimposing on the Doppler observed downward velocity profiles a profile of terminal fall velocities predicted by a simple crystal growth model. The model simulated the growth of a hexagonal plate initialized as a  $30\mu$  crystal at Ku-band radar detected cloud height assuming no environmental motion. The model crystal growth environment in the vertical was constructed from rawinsonde data closest in time to the profile considered. The growth equations and assumptions contained in the model are given in Appendix III. Riming was not simulated by the model because accurate modelling is critically dependent on the liquid water content and droplet spectra which were unknown for this case. The impact of the variation of liquid water content and droplet spectra on fall velocity profiles under riming conditions can be seen in Fig. 4 in the various profiles labeled "R". Thus discrepancies between model generated vertical velocities and observed vertical velocities could be interpreted as evidence of either riming or environmental motion.

Vertical profiles of horizontal velocity were created using the Doppler radar in VAD (Velocity-Azimuth-Display; Battan, 1973) mode. The analysis technique essentially fits an azimuth to radial velocity curve to the Doppler data at a certain altitude, from which the average horizontal wind speed and direction at that level can be ascertained.

Error bars around the points on the profiles are derived from an estimate of the accuracy of the curve fit relative to the actual data. The three profiles determined for this study were taken with the dish tilted at a 45° elevation angle. This elevation was chosen in order to maximize the component of radial velocity due to horizontal velocity while minimizing ground return at low elevation angles.

Rawinsonde-derived vertical profiles of horizontal velocities are displayed for purposes of comparison. Discrepancies in wind speed and direction can be interpreted as differences in flow characteristics between the rawinsonde launch site and the radar site.

The storm of December 10 and 11, 1979, also formed the best period for intercomparison of the cloud detection characteristics of the three radars, as all three sets were operational and located on the same site. Intercomparison is only possible during the times when the X-band was not operating in Doppler mode because the data system was capable of recording digital data from the K-band set only during these times. Time series were constructed of radar detected cloud top height at time intervals of twelve minutes during the storm for intercomparison periods.

The goodness of the Rayleigh approximation was tested and profiled in the vertical for one case. Values of  $\eta$ , the radar reflectivity factor, were displayed in the vertical for the K-band and X-band sets. If the Rayleigh approximation is good at an individual level, the ratio of the eta values should be a constant 24.08 dB (the inverse ratio of the fourth power of the wavelengths).

### III. RESULTS

#### A. OBJECTIVE 1

##### - Behaviour of Cloud Top and Reflectivity Patterns in Space, Time and Temperature

The six periods of observations analyzed under this objective were as follows (times are Mountain Standard).

	<u>Radar On</u>	<u>Radar Off</u>
Case 1	2/22/79 1550	2/23/79 0135
Case 2	2/23/79 1506	2/24/79 1156
Case 3	3/01/79 1253	3/01/79 2314
Case 4	3/02/79 0940	3/03/79 1121
Case 5	12/10/79 1807	12/11/79 0611
Case 6	12/22/79 1730	12/23/79 0930

For each case study, a brief summary of the synoptic conditions existing during the time of observation is presented. The synoptic maps from which the summaries were constructed are contained in Appendix II. The time series of reflectivity and temperature field, and precipitation data are then displayed; followed by a histogram of the distribution of cloud top temperatures for each case. A key to the alphabetical values and shading patterns in the time series of reflectivity is presented on pages 28 and 29. Following each case presentation is a short discussion of the characteristics of the individual storm period pertaining to general reflectivity patterns, cloud top height variation, cloud top temperature variation, and distribution of high reflectivity zones (> 20

dBz). A summary discussion on the characteristics of all six cases is then presented.

1. Case 1 2/22/79 1550 to 2/23/79 0135

The 2/23 0Z 70 KPa chart shows a cutoff low pressure center over the Dakotas. The COSE study area lies between two surface cold fronts extending down from the low as analyzed by the NMC. The 0Z 70 KPa chart shows height rises in the region near the COSE study area associated with a ridge between the trough to the east of the Rockies and another trough developing off the West Coast. The 3Z 2/23 satellite photo shows that the clouds detected by the radar were part of a system extending throughout Northern Colorado and Western Wyoming.

The most striking feature concerning general reflectivity patterns in case one is the periodicity in time of both cloud top height and higher reflectivity regions (see Fig. 10). It is observed, for example, from features centered 1605, 1838, and 2102 that a periodicity in the vertical of about 2.5 hours exists in the first part of the storm. This is in agreement with periodicities observed in the Climax region (Furman, 1967). After 2200 a periodicity of about 1 hour can be seen in the reflectivity pattern (features centered at 2220, 2323, 0020) and to a lesser extent in the cloud top height pattern. "Separation" regions of lower reflectivity ( $< 5$  dBz) and relatively lower solid cloud top heights occur centered at 1730, 2002, 2156, 2241, and 2347. The same periodicities exist in the reflectivity pattern in the lowest detectable range bin (350 m). A second feature in the general reflectivity pattern is the relatively rapid lift of cloud base associated with the clearing over the radar starting 0100.



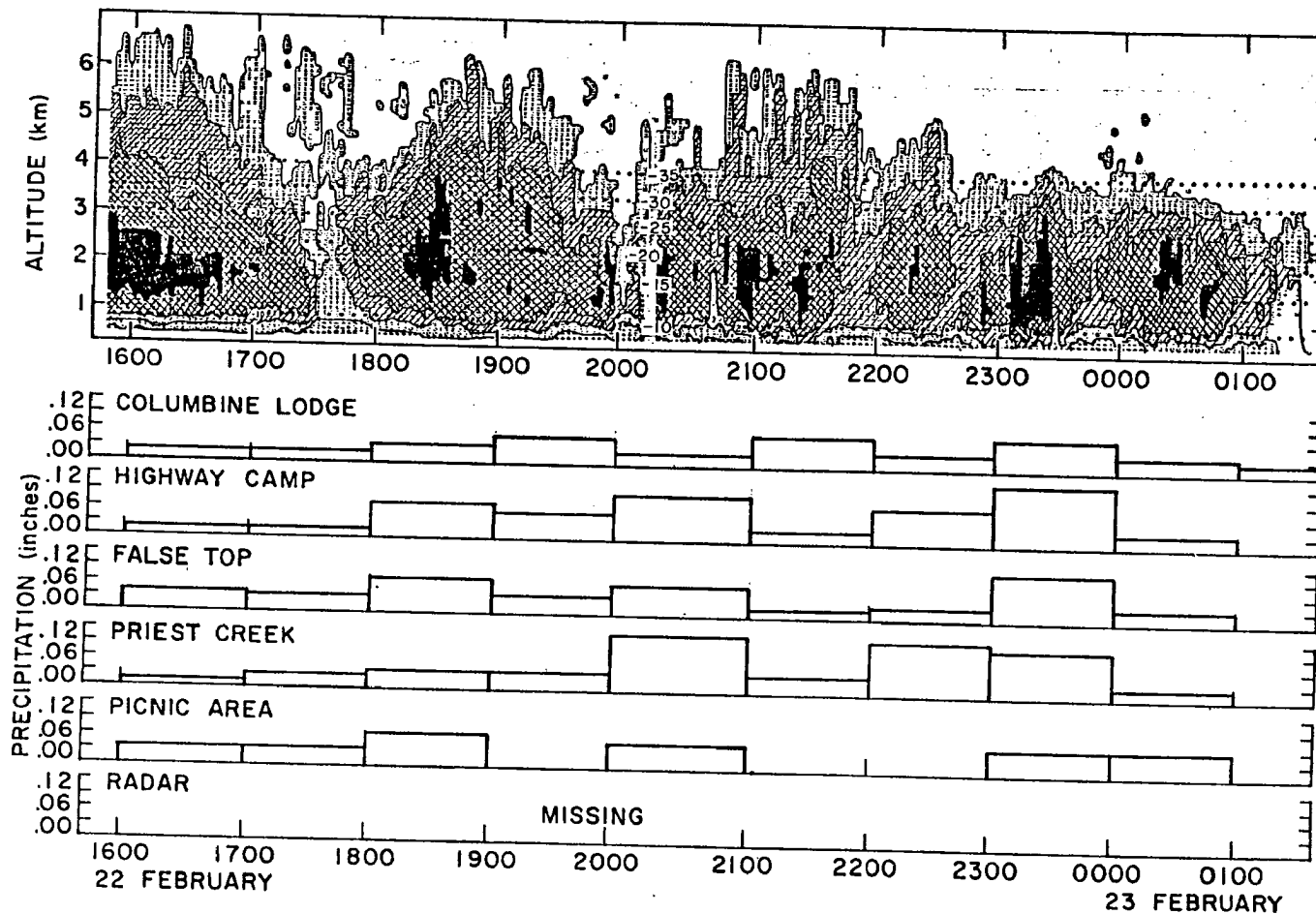


Figure 10. Ku-band radar reflectivity and gauge precipitation records for the storm 22-23 February, 1979, 1550 MST 2/22 to 0135 MST 2/23. Each line in the reflectivity record represents a three-minute interval. Dotted lines represent isotherms as derived from rawinsonde data. Each precipitation bar represents the total recorded during that hour at the gauge indicated.

The solid cloud tops varied most strongly with the periodicities described in the previous paragraph. What appears to be multiple decks and short-time scale isolated features above the solid tops occurred near "separation" periods. The maximum extent of the radar detected cloud tops was 6.5 km AGL (Above Ground Level; all heights are recorded AGL unless otherwise indicated) in the first part of the storm, and cloud top height seemed to reach a steadily decreasing maximum with each semi-hourly "pulse" in the second part of the storm. Before the cloud advected out of the radar detection region, cloud top heights had lowered to less than 3 km AGL.

From Fig. 11 it can be concluded that the cloud top temperature during most of the storm was colder than  $-35^{\circ}\text{C}$ . In the first part of the storm, radar cloud top heights were more than 2.5 km above the  $-35^{\circ}\text{C}$  isotherm, therefore the actual cloud tops were probably much colder than  $-35^{\circ}\text{C}$ . In the later stages of the storm, after 2235, the solid cloud tops lowered to below the  $-35^{\circ}\text{C}$  isotherm, and after 0059, below the  $-30^{\circ}\text{C}$  isotherm.

Regions of reflectivity greater than +20 dBz appeared primarily near the center of the periodic "pulses" described above. The regions displayed no strong correlation with temperature, except that all of the regions were contained between the  $-35^{\circ}\text{C}$  and  $-10^{\circ}\text{C}$  isotherms. Regions of high reflectivity were primarily associated with increases in cloud top height.

Generally, the precipitation records are characterized by 3 relatively high-rate periods (1800-1900, 2000-2100, 2200-0000). The record at Columbine Lodge displays a lag in time in the first two high-rate periods. A correlation between changes in precipitation rate and

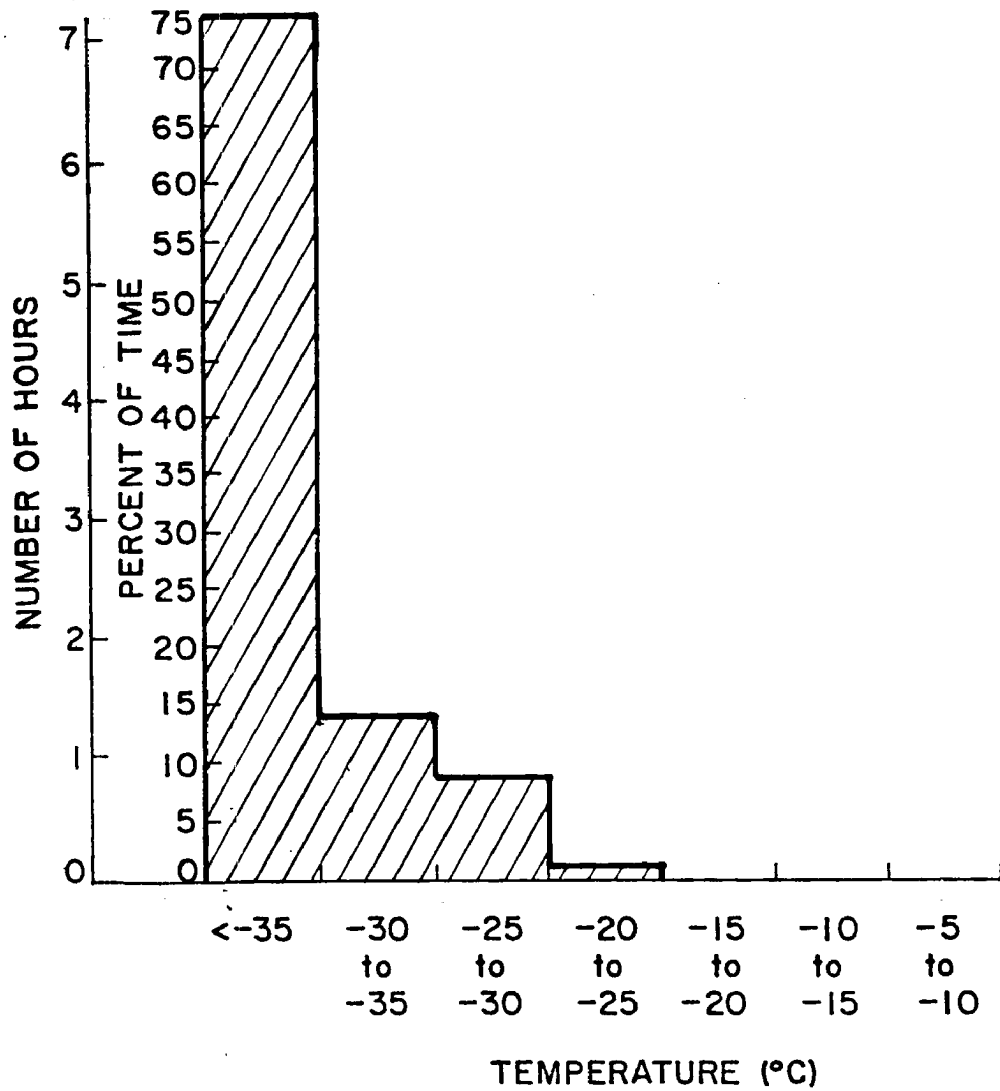


Figure 11. Cloud top temperature distribution for the storm of 22 February 1550 to 23 February 0135 MST, 1979.

changes in cloud top height or reflectivity pattern appears to exist in this case, but is difficult to confirm because the time scale of the precipitation data makes intercomparison difficult.

2. Case 2 2/23/79 1506 to 2/24/79 1156

The 2/24 0Z 70 KPa chart shows a trough over the Great Basin and the Southwest. The 09Z 2/24 surface map shows that the surface front had just previously passed through the COSE study area at 09Z (0200 MST). Satellite data was not available for this case.

A "line" which exceeds threshold reflectivity extends throughout the storm at 2.3 and 2.4 km AGL (see Figs. 12a and 12b). This line is most evident just before 1600, before 1800, before 0000, and persists after 0600 when no other return is detected around the 2.3 km AGL region. This feature is thought to be of non-meteorological origin based on the following observations:

1. The line persists at the same level throughout the storm when other cloud features display rather large height variation in time.
2. The line can be intermittantly observed at the same elevations in other storm periods (see, for example, 2/22/79 1726-1729, 2/23/79 0132-35, 03/02/79 0940-1100, 03/02/79 1331-1649).
3. Notes in the radar log book identify several periods with an unusual "spike" on the A-scope centered at about 2.4 km. Occasionally this feature appeared when the A-scope indicated no other return at any level. The radar operator also noted that this feature appeared "less grassy" (less high frequency time variability) on the A-scope than characteristic meteorological return.

This unusual reflectivity pattern is probably the result of energy from a side-lobe beam intersecting any of the surrounding hills. The

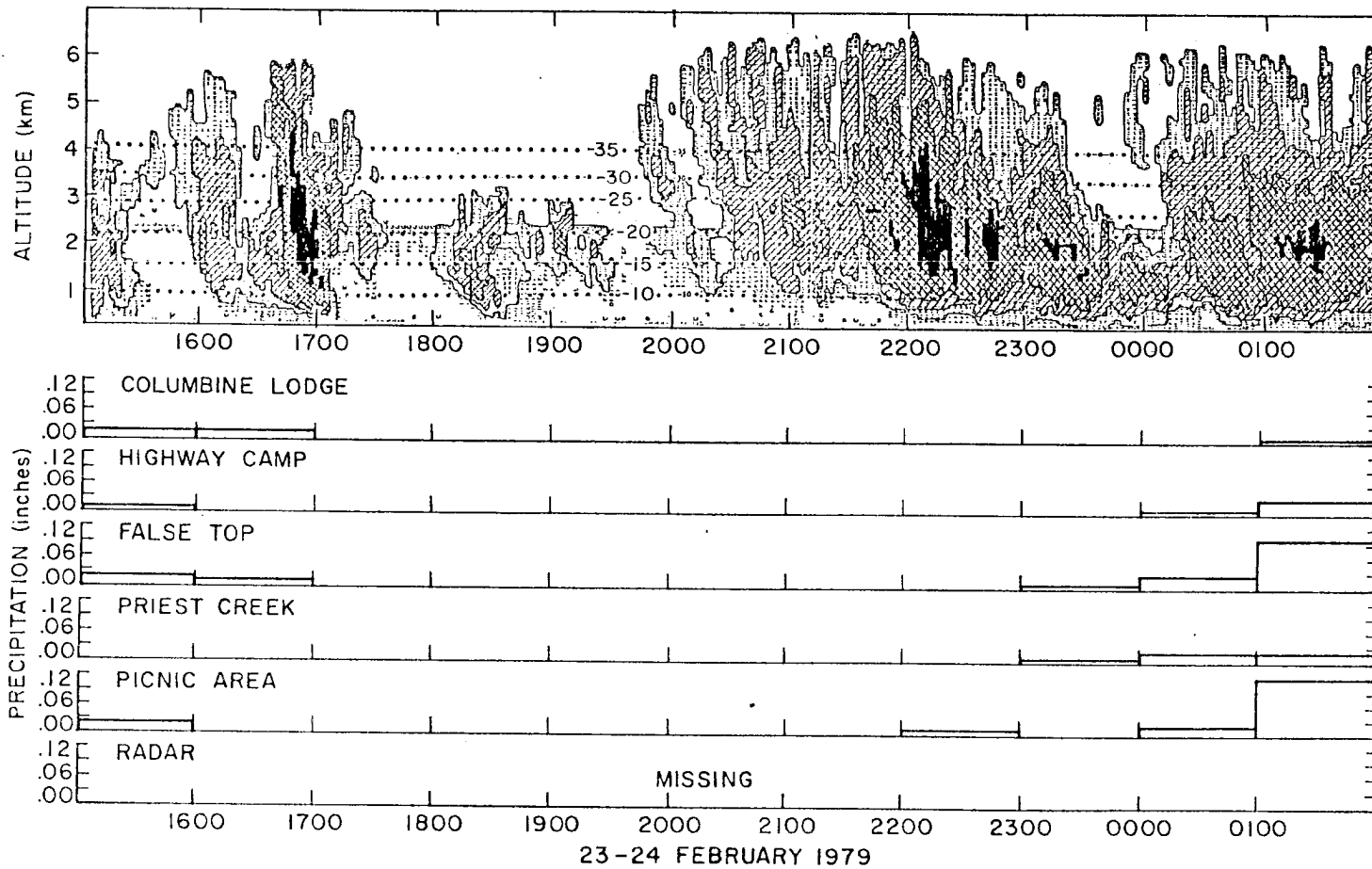


Figure 12a. Ku-band radar reflectivity and gauge precipitation records for 23 February 1506 to 24 February 0158 MST, 1979.

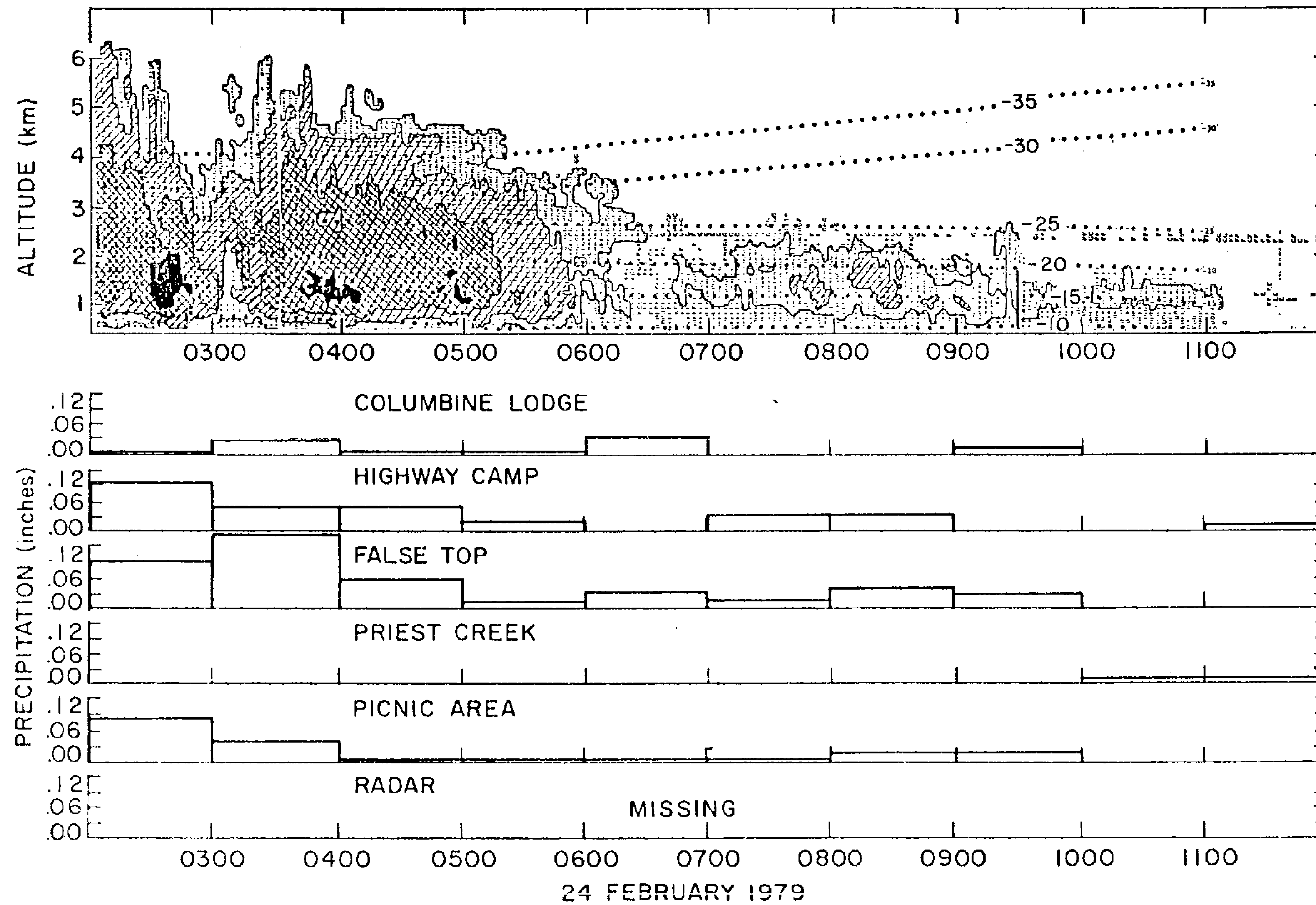


Figure 12b. Ku-band radar reflectivity and gauge precipitation records for 24 February 0200 to 1156 MST, 1979.

feature did not appear in the data taken during December 1979.

Periodicity in the reflectivity patterns can again be observed on the order of 2 to 3.5 hours, although not as consistent or as regular as in case 1 (note features centered 1642, 1824, 2155, 0143, and 0401). "Separation periods" can also be observed centered 1536, 1742, 1939, midnight, and 0310. The non-meteorological echo is most easily distinguished in the separation periods. Between 0500 and 1100 an inversion develops above 2.5 km and the cloud diminishes.

Cloud top height varies rapidly with time in the course of the storm until the inversion develops in the later stage. Maximum cloud top height reached about 6.5 km and fell to about 1.5 km before the radar detection area cleared.

Figure 13 shows that the majority of cloud top temperatures for this case were below  $-35^{\circ}\text{C}$ . The warmer cloud top temperatures ( $> -25^{\circ}\text{C}$ ) occurred primarily after the onset of the inversion.

The high reflectivity zones in case 2 were again associated with increases in cloud top height and increases in reflectivity at 350 m. Again, no zone of reflectivity higher than 20 dBz extended below the  $-10^{\circ}\text{C}$  isotherm, although, in two instances, the high reflectivity zones extended slightly above the  $-35^{\circ}\text{C}$  isotherm. After 0522, no region of the storm was observed to have reflectivity  $> 10$  dBz.

The highest precipitation rates during the storm sequence appeared in the period from 0100 to 0400 on 2/24. Light, intermittent precipitation occurred at various levels after 0400. The period from 1700 to 2200 on 2/23 contained no precipitation. This is rather surprising considering the relatively high cloud tops and strong reflectivities observed during this period. It may be that convective updrafts during

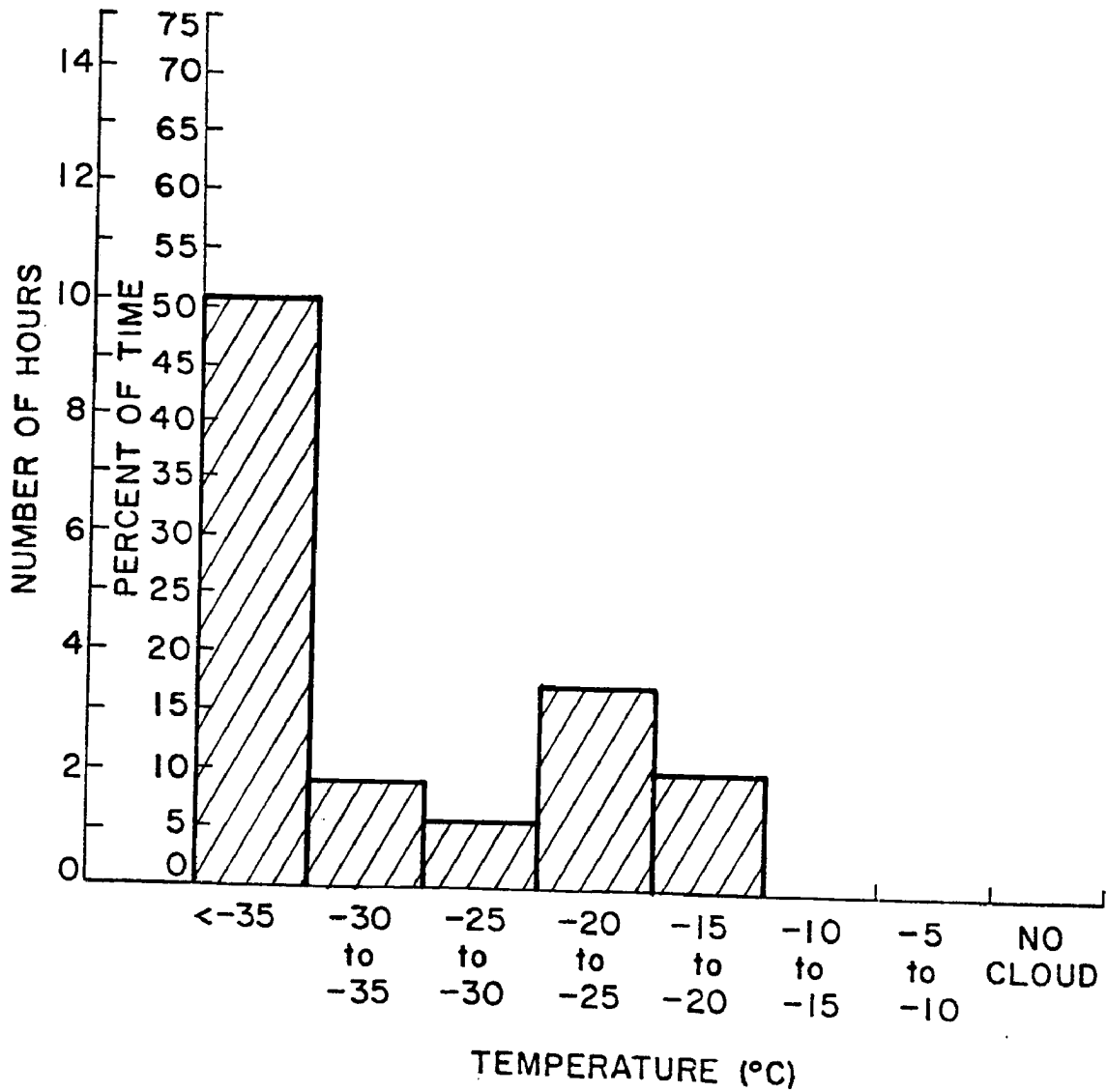


Figure 13. Cloud top temperature distribution for the storm 23 February 1506 to 24 February 1156 MST, 1979.



this period effectively lifted the crystals out of the COSE region. However, the Craig rawinsonde analysis of Lee (1980), showed only shallow and weak convective instability for this case. Perhaps the clouds detected by radar were producing precipitation of a "showery" local nature which did not impact on the COSE gauges. Note that the data for the radar precipitation gauge is missing, so that if localized precipitation existed it would remain undetected.

### 3. Case 3 03/01/79 1253 to 03/01/79 2318

The 0Z 03/02 70 KPa chart shows the trough axis still well to the west of the COSE study area. However, southwest flow leading the trough is advecting warm moist air into the area from the Pacific. The 03Z 03/02 surface map indicates a surface low pressure center over the Great Basin with associated cold front along the Nevada-Utah border. A stationary front is indicated through central Wyoming. The 03Z 03/02 satellite picture indicates extensive cloudiness in the western half of the U.S. associated with the moisture advection.

Although in portions of Case 3 very deep clouds exist, at no time during the period of observation does the cloud or precipitation pattern extend to the ground (see Fig. 14). Cloud base undulates around 1.5 km AGL with downward protrusions that may represent verga or snow showers which impact the ground outside the COSE precipitation network. Strongly periodic variations are not detected during this period although a feature resembling a separation zone existed centered 15:38. After 20:38 cloud bases and tops lower gradually.

Cloud top heights vary rather gradually with time, reaching a maximum of about 7 km AGL and a minimum of about 3.3 km AGL. The distribution of cloud top temperature in Fig. 15 indicates that the majority of

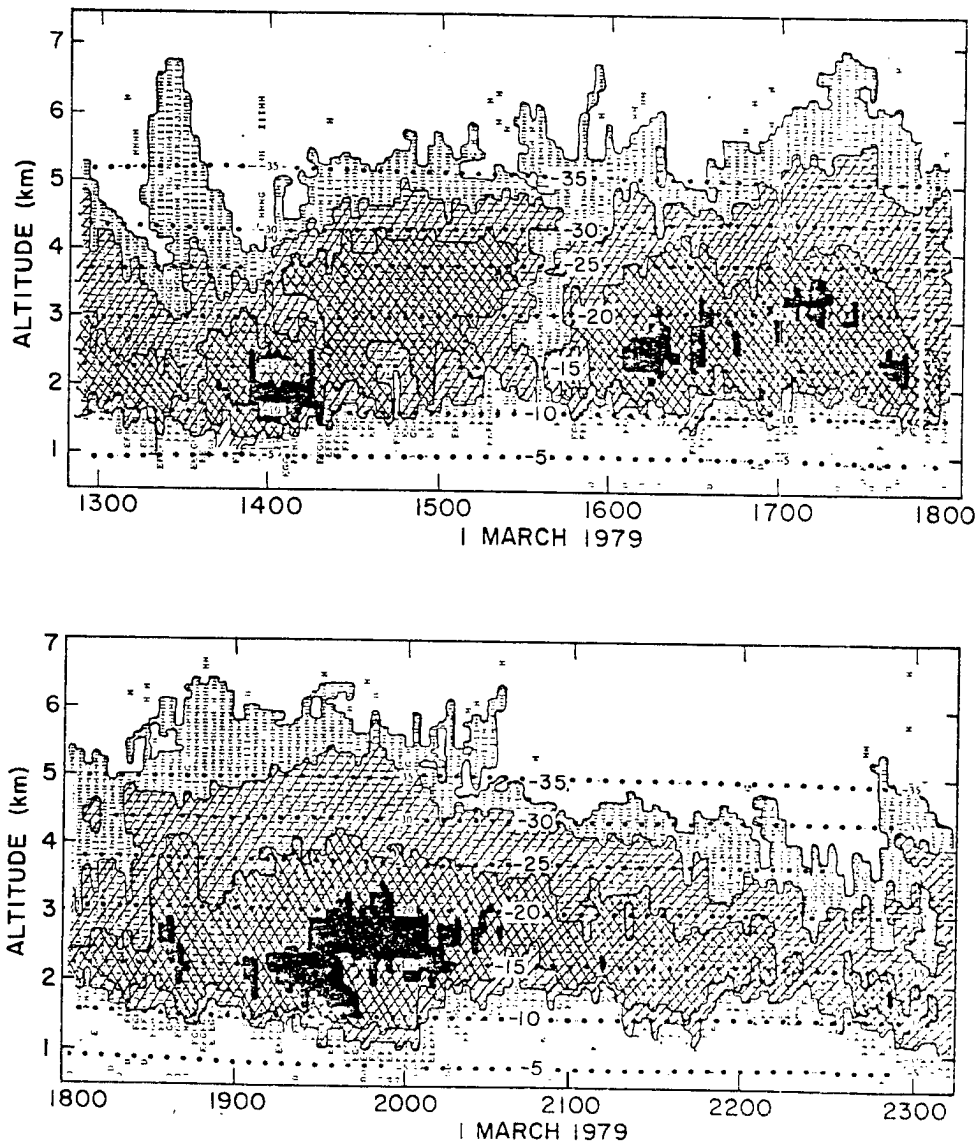


Figure 14. Ku-band radar reflectivity record for 1 March 1253 - 2318 MST. No precipitation occurred at any COSE gauge during this period.

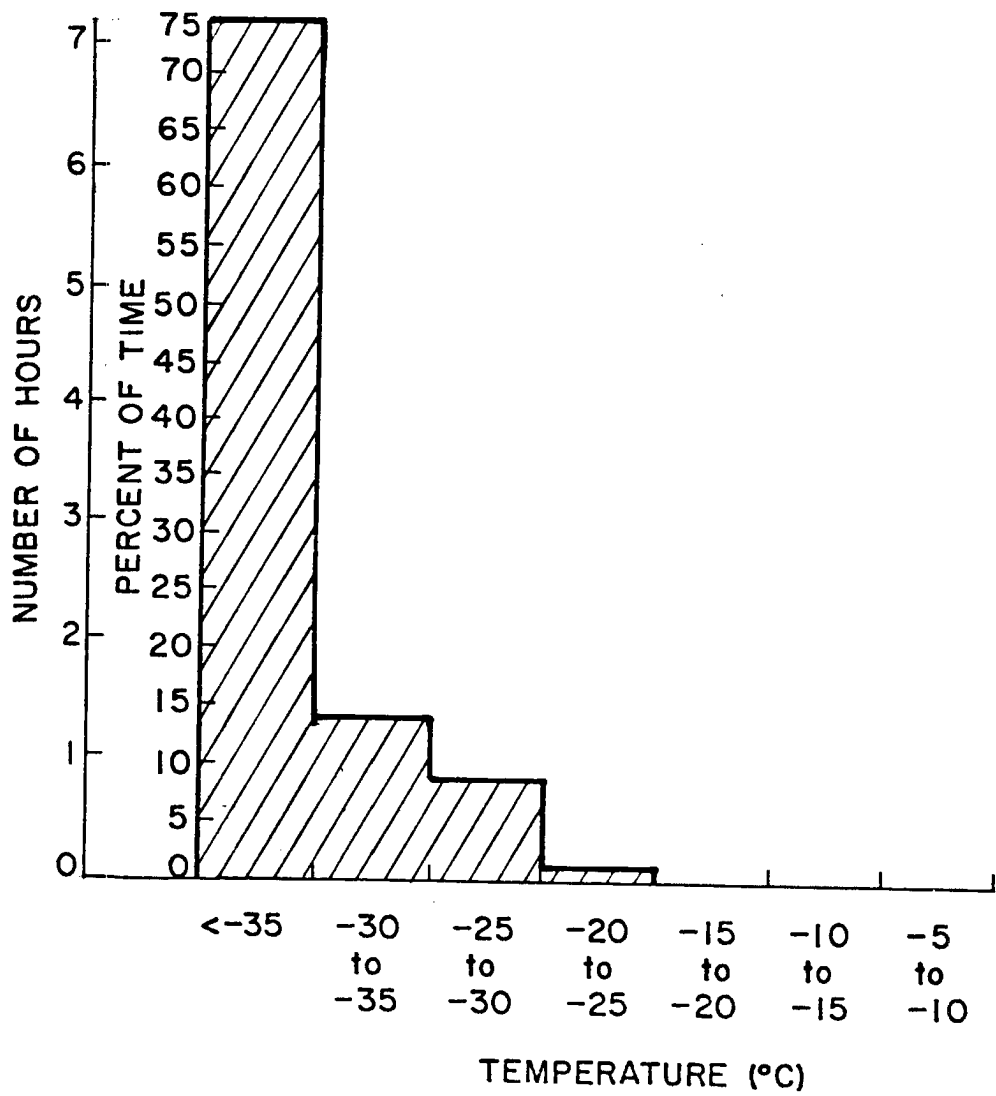


Figure 15. Cloud top temperature distribution for 1 March 1253 - 2318 MST, 1979.

the observations were in the  $< -35^{\circ}\text{C}$  category. At no time during the period of observation were the cloud top temperatures  $> -20^{\circ}\text{C}$ .

The high reflectivity zones are observed below the  $-25^{\circ}\text{C}$  isotherm. At 14:00 one high reflectivity zone extends slightly below the  $-10^{\circ}\text{C}$  isotherm.

No precipitation was occurring at any of the six precipitation gauge sites during this period, therefore the precipitation record is not displayed below the reflectivity record for this case. A rough calculation was made to estimate what average fall velocities would have existed if precipitation was blowing over the ridge. Cloud base was assumed to remain at 1.5 km AGL and the ridge-ward component of the wind at that level was determined from Craig radiosonde launches at 1400, 1700, 2000, and 2300 MST on 1 March. From Fig. 5 (page 17) it can be seen that the Highway Camp precipitation gauge (gauge B) is approximately 10 km east of the Steamboat Springs radar site. The approximate time necessary for cloud particles observed by the radar at cloud base to be advected eastward as far as the Highway Camp gauge was then determined. The Highway Camp precipitation gauge is approximately 650 m below the average cloud base observed at the radar. In order for significant blow over to occur, the average downward velocity of the particles ( $w$ ) would have to be such that the time taken to fall 650 m would be less than the characteristic time necessary to transverse the horizontal eastward component of distance between the radar site and the Highway Camp precipitation gauge. In this way a downward velocity for the particles at cloud base can be determined, below which precipitation blowing over the Highway Camp gauge would be feasible. The results of this analysis are presented in Table 3.

Table 3

Determination of a Critical Downward Velocity  
below which Blower is feasible at the Highway Camp Guage

Rawinsonde Launch Time (MST) on 1 March	Ridgeward Wind Component at Cloud Base (m/s)	Time Necessary to Advect Horizontally to Highway Camp Guage (sec)	Critical Downward Velocity (m/s)
1400	8.9	1127	.58
1700	8.0	1250	.52
2000	8.5	1176	.55
2300	8.5	1176	.55

From Table 3 it can be seen that average downward velocities ( $w$ ) less than about .55 m/s had to exist in order for precipitation particles to blow over the Highway Camp guage.

An indication of the role of upward convective components in the average downward velocities can be determined by an examination of the Equivalent Potential Temperature profiles during the storm sequence (see Fig. 16). Only one instance of convective instability can be seen below 2 km AGL above the radar in the rawinsonde data from the 2000 MST 01 March, yet this instability is weak and shallow. Upward motions due to convective instability probably did not contribute greatly to the reduction of precipitation fall velocities for this case.

#### 4. Case 4 03/02/79 0940 to 03/03/79 1120

The OZ 03/03 map shows the 70 KPa low centered over Southeastern Colorado with northerly flow and cold air advection into the COSE study area. The 03/03 06Z surface map indicates the precipitation activity

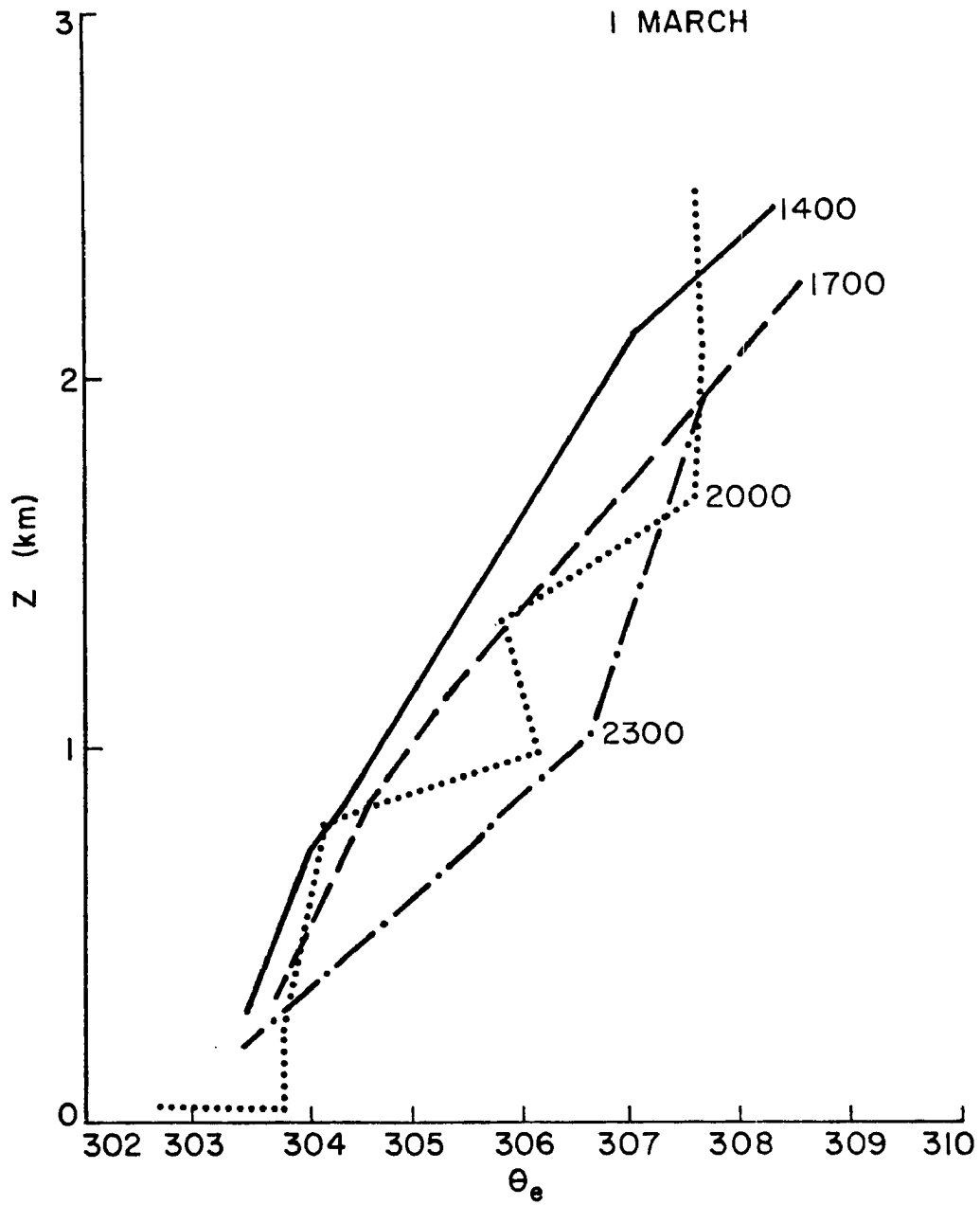


Figure 16. Equivalent Potential Temperature profiles in the vertical for rawinsonde launches at 1400, 1700, 2000, and 2300 on 1 March.

occurring primarily on the East Slope of the Rockies with a surface cold frontal boundary in the COSE area. The 03/03 03Z satellite photo also indicates the higher clouds existing east of the Rockies, while clouds in Northwest Colorado are barely distinguishable and very low. The 03/03 12Z 70 KPa chart shows the low intensifying and digging, centered at this time over Central Oklahoma. The northwesterly flow persists in the COSE study area, however the temperature gradient north of the COSE area has relaxed. The data for Grand Junction on the 06Z surface map, and the 0 and 12Z 70 KPa maps indicate relatively moist air at low levels in Western Colorado.

This case illustrates a long period of shallow cloud and relatively warm cloud top temperatures (see Figs. 17a and 17b). The first detected cloud in this period is below 1.5 km (under light return at 2.3 km which is probably non-meteorological; see discussion on p. 38). A brief cloud-free region sets up starting 1330 which is terminated with the onset of some isolated return patterns at 1410. A two-deck structure exists from 1528 to 1625, then the single shallow deck regime is established which persists throughout the rest of the period.

The maximum vertical extent attained by isolated features preceding the two-deck structure was approximately 4 km. Cloud top height at the onset of the shallow deck regime was approximately 2.5 km. Cloud top slowly lowers until about 0200 on 03/03/79 when cloud tops were about 1.5 km. Cloud tops then rose to about 2.7 km and slowly lowered until the end of the observation period when cloud tops were below 1.5 km. The sudden rise in cloud top at 0430 seems to be associated with the rise of the  $-25^{\circ}\text{C}$  isotherm between 0200 and 0500; however, the cloud top lowers as the  $-20^{\circ}\text{C}$  isotherm rises between 0800 and 1100.

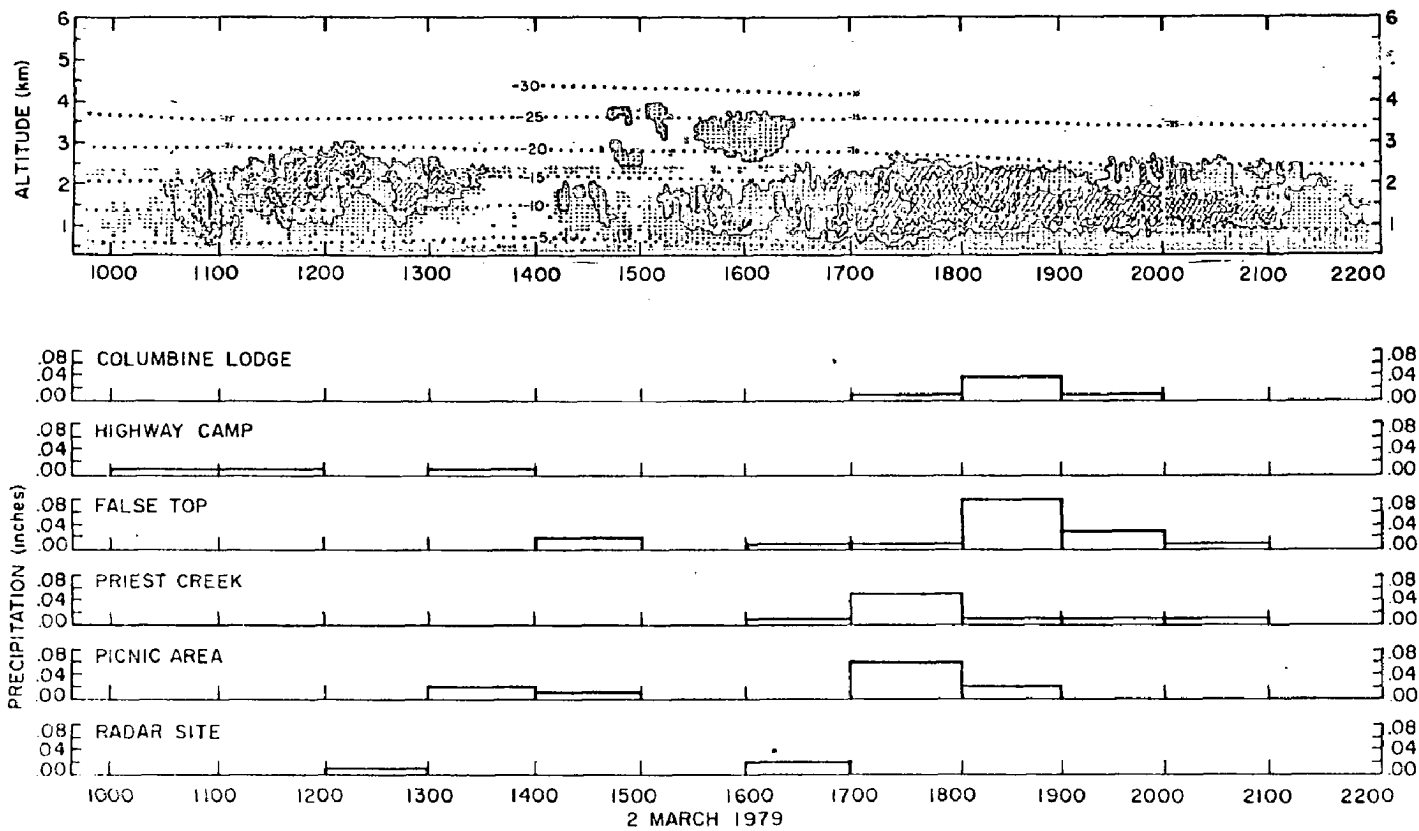


Figure 17a. Ku-band radar reflectivity and gauge precipitation for 2 March 0845 - 2200 MST, 1979.



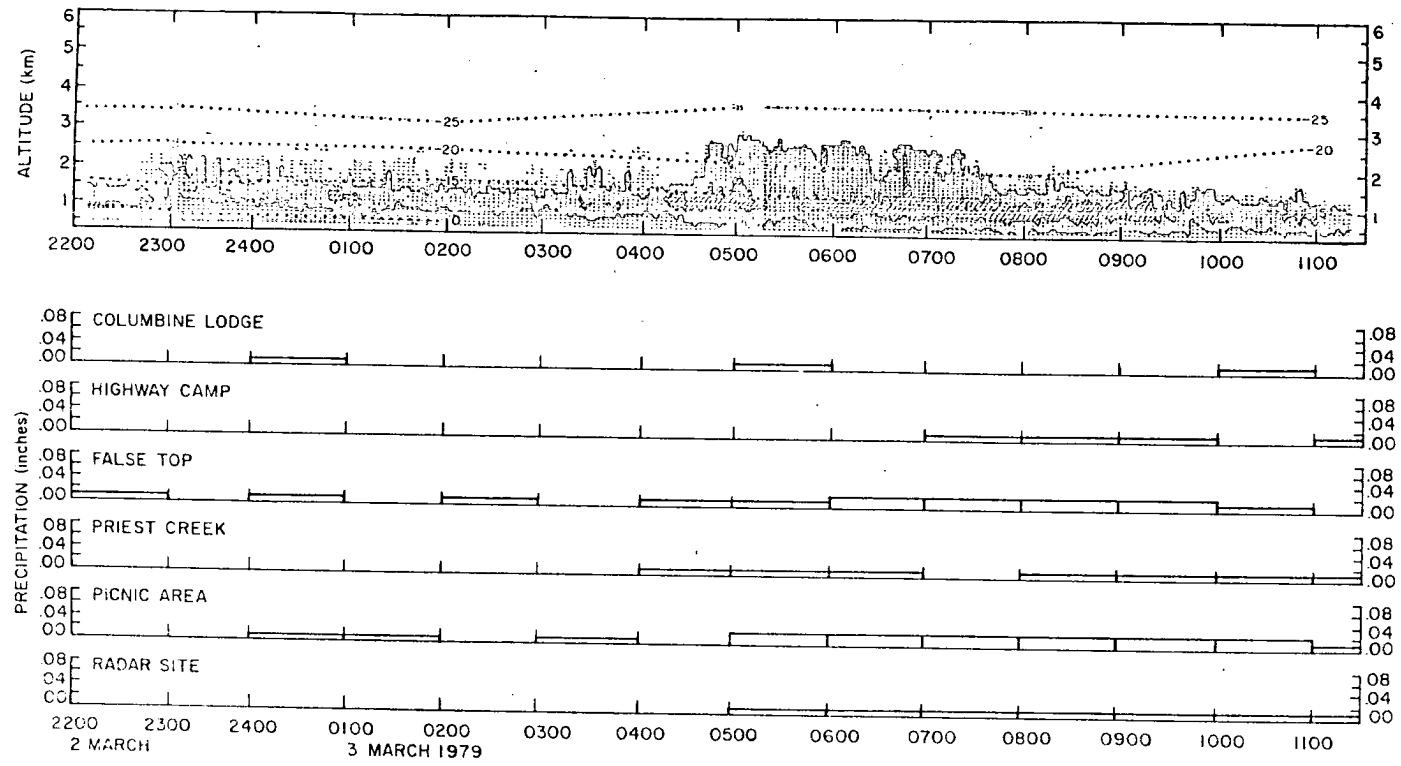


Figure 17b. Ku-band radar reflectivity and guage precipitation records for 2 March 2200 to 3 March, 1121 MST, 1979.

The histogram of cloud top temperatures (see fig. 18) reveals that cloud top temperatures were warmer than  $-25^{\circ}\text{C}$  for more than 17 hours during the period of observation. The longest period when cloud top temperatures were below  $-20^{\circ}\text{C}$  existed after the rise of the  $-25^{\circ}\text{C}$  isotherm starting about 0730 on 03 March.

Only three short-lived instances of the appearance of high reflectivity zones exist during this period of observation (03/02 1052, 03/02 1752, and 03/02 1946). In each case the high reflectivity zone appears below the  $-15^{\circ}\text{C}$  isotherm. The lowest reflectivity levels seem to be associated with the warmest cloud top temperatures.

Most of the period is characterized by light, intermittent precipitation at all gauges. The notable exception is from 1500-1900 on 02 March, when precipitation rates increased. During this time also, the strongest reflectivity zones appeared.

##### 5. Case 5 12/10/79 1807 to 12/11/79 0558

A short wave embedded in the mean flow is indicated by a vorticity maximum centered over Western Montana as indicated by the 12-hr barotropic 50 KPa prognosis valid 0Z 12/11. The 12/11 0Z 50 KPa chart shows a pressure pattern very similar to the forecast pattern with strong southwest winds over the COSE study area. The 70 KPa 12/11 0Z chart shows rapid height falls and isobar-isotherm crossing near the COSE study region indicating that the wave is digging. The 0Z 12/11 surface map indicates a stationary front just to the northwest of Colorado with a surface lee trough over Western Kansas and the Texas Panhandle. The 3Z satellite photo indicates that the high clouds over the COSE region were embedded in a band of high clouds ahead of the surface front. By 6Z the surface map indicates that the front had moved through the COSE

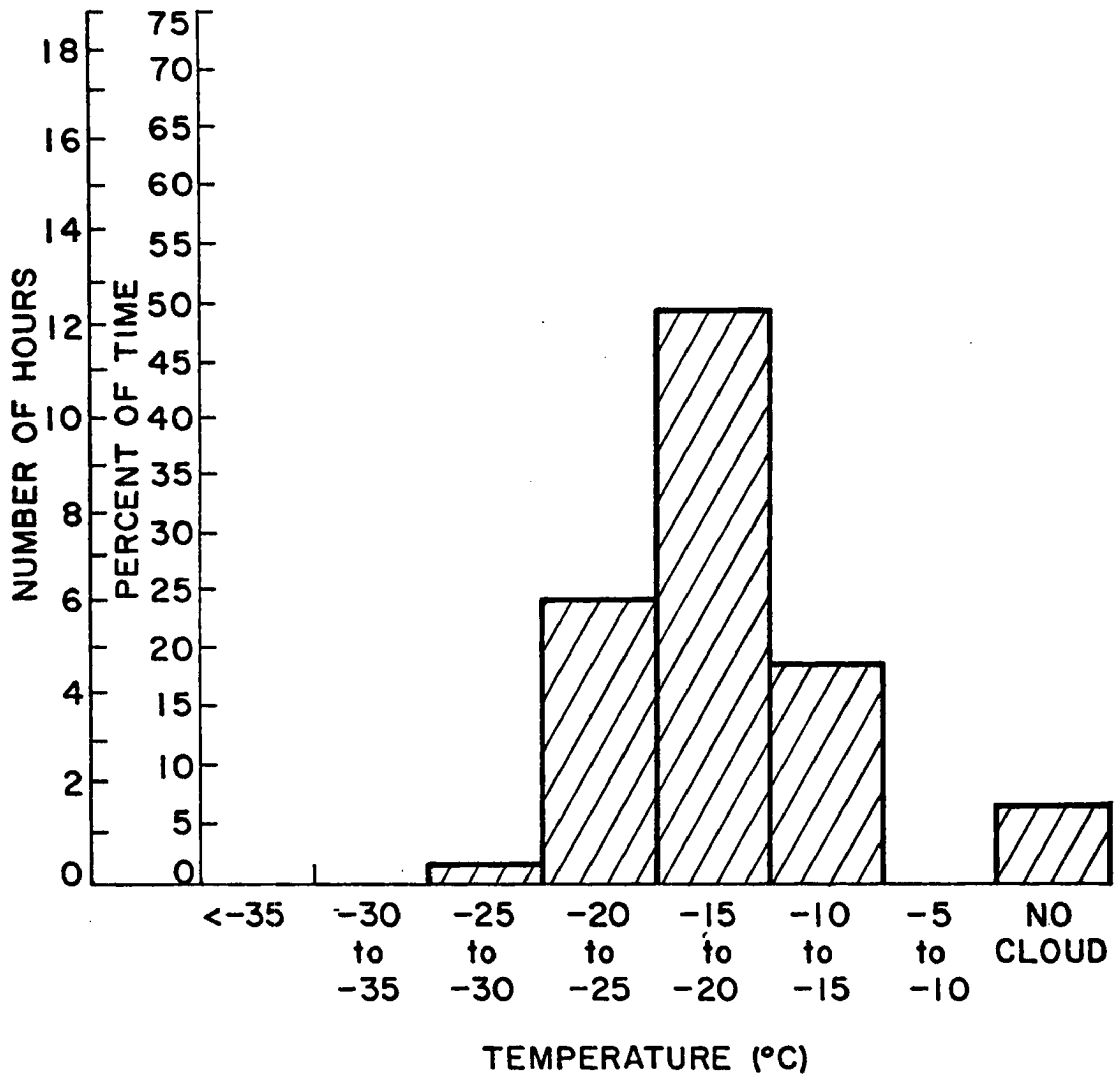


Figure 18. Cloud top temperature distribution for 2 March 0845 to 3 March 1121 MST, 1979.

region. By 12Z the 70 KPa chart shows cold air advection still persisting over the COSE region. The 12Z satellite photo shows low post-frontal cloudiness in the COSE vicinity. The 12/11 18Z surface map indicates that the front had moved well out of Colorado by this time.

A brief isolated feature first appears 1813-1828 centered about 5.2 km AGL followed by the onset of continuous cloud at 1849 (see Fig. 19). The first appearance of the cloud at 5.2 km is probably reflective of the first advection of moisture at that level. Thereafter, the cloud tops generally lower slowly while the bases lower relatively rapidly until 2110 when precipitation exists in the lowest radar detectable range gate (350 m). The behavior of the isotherm pattern indicates that the surface front passed through the area between 2000 and 2300. A period of increased reflectivity with relatively stable cloud tops exists from 2300-0200 during the period that the frontal boundary is rising through the cloud. Starting about 0200 12/11 the cloud tops begin to lower again and reflectivity values decrease.

Cloud top heights reach a maximum of 5.5 km at the beginning of the storm and attain approximately the same height at 2325. By the end of the observation period the cloud tops reach a minimum of 2.7 km.

The distribution of cloud top temperatures (see Fig. 20) shows that 48% of the observations fell between  $-25^{\circ}\text{C}$  and  $-30^{\circ}\text{C}$ . Cloud top temperatures below  $-30^{\circ}\text{C}$  occurred primarily near the onset of the cloud and during the period 2300 to 0200. The cloud top temperatures warmer than  $-25^{\circ}\text{C}$  occurred as cloud top heights lowered toward the end of the observation period.

One zone of high reflectivity appeared from 0010 to 0031 centered about 2.3 km. The characteristic temperature of this zone is probably

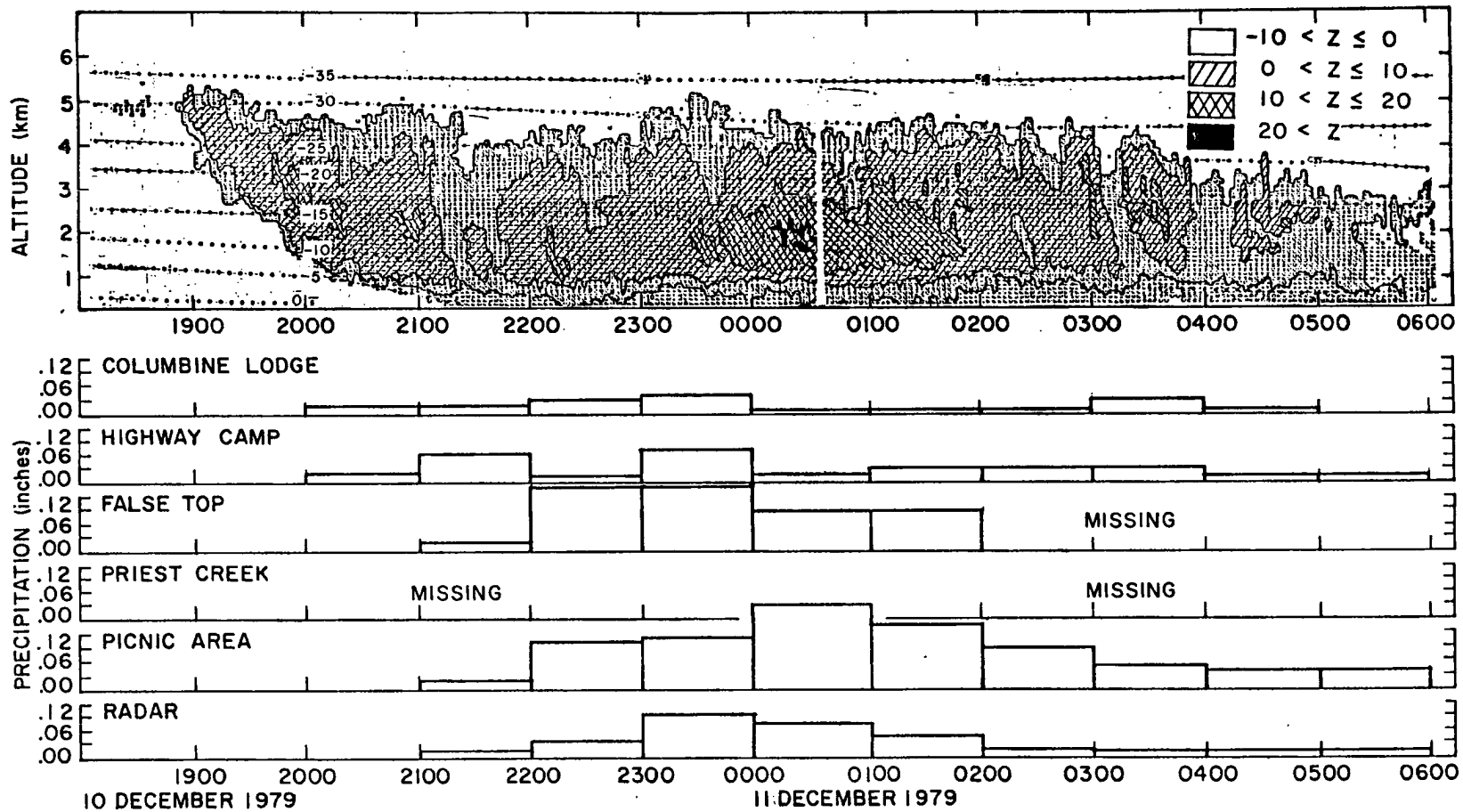


Figure 19. Ku-band radar reflectivity and gauge precipitation records for 10 December 1607 to 11 December 0601 MST, 1979.

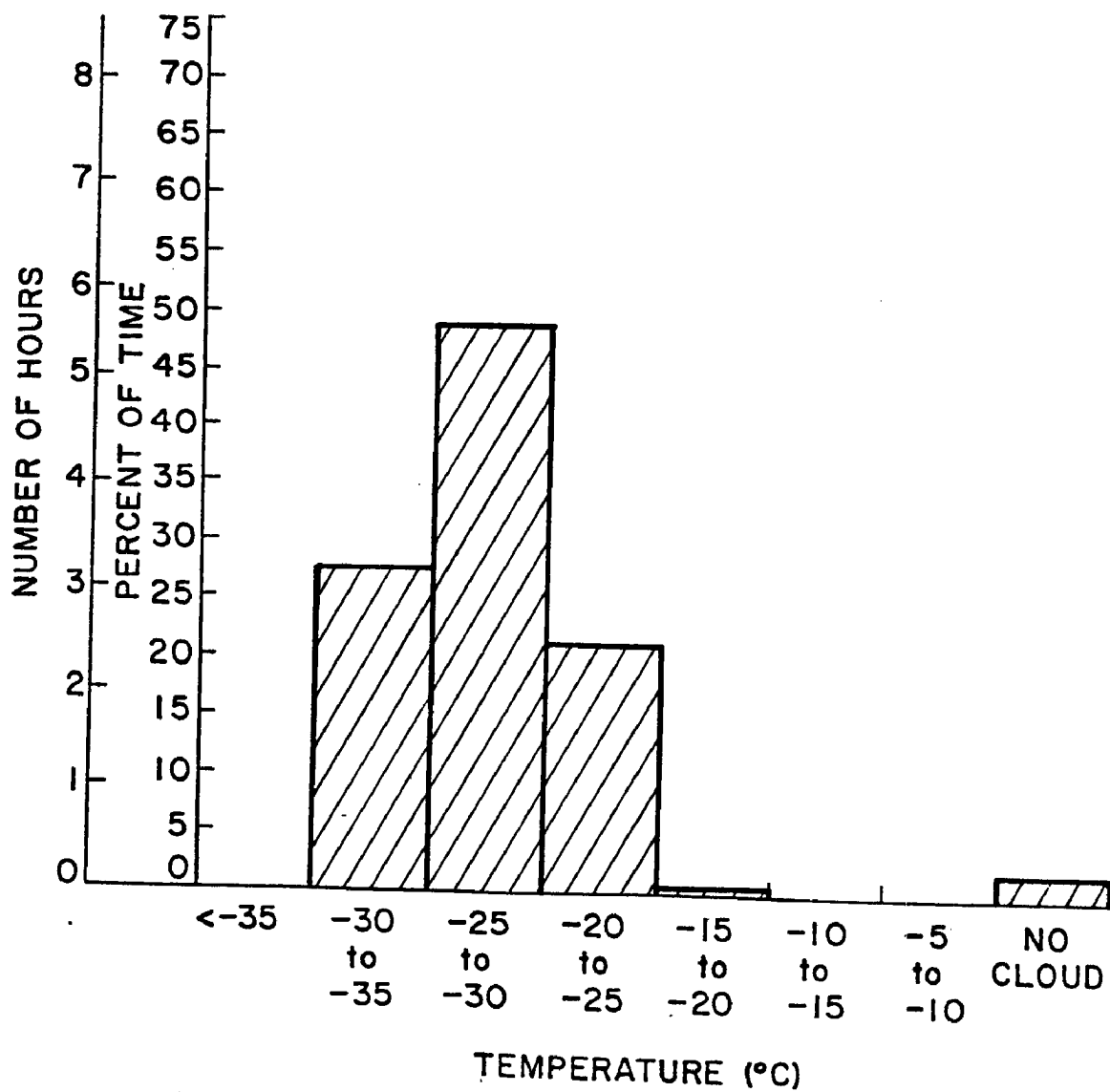


Figure 20. Cloud top temperature distribution for 10 December 1607 to 11 December 0601 MST, 1979.

around  $-15^{\circ}\text{C}$ . Further accuracy in the characteristic temperature of this region is hard to obtain because the linear interpolation scheme may not accurately represent the actual changes in temperature in this region during this time period.

Although the Ku-band set was out for maintenance after 0630, the data obtained by the K-band radar indicates that a period of low reflectivity shallow cloud existed from 0600-1430 (see Fig. 21) on 12/11. Several periods exist during this time during which the K-band radar detected two separate cloud decks. Craig rawinsonde data at 15Z and 18Z (0800 and 1100 MST) indicates a shallow inversion existed from about 1650 m AGL to about 2000 m AGL through which the detected temperature rose from  $-21.9^{\circ}\text{C}$  to  $-18.5^{\circ}\text{C}$ . This inversion apparently had a limiting effect on the cloud top height of the upper deck, such that the coldest portion of the system during this time was probably also about  $-22^{\circ}\text{C}$ . Strip chart records indicate that a two deck regime again appeared from 1453 to 1653 and that cloud persisted over the radar until after 1720.

The precipitation record indicates that precipitation started first at the Columbine Lodge and Highway Camp gauges before 2100 MST, then began at the lower elevation gauges. The highest observed precipitation rate during the six case studies (0.5 cm/hr) occurred at the Picnic Area gauge from midnight to 0100 on 11 December coinciding with the appearance of the high reflectivity zone. Relatively high precipitation rates occurred at False Top and the Radar Site as well, despite the scarcity of high reflectivity zones in this storm.

#### 6. Case 6 12/22 1730 to 12/23 0930

On 12/21-22 a surface low originally positioned over Central Utah moved directly over the COSE study area and reformed in Southeast

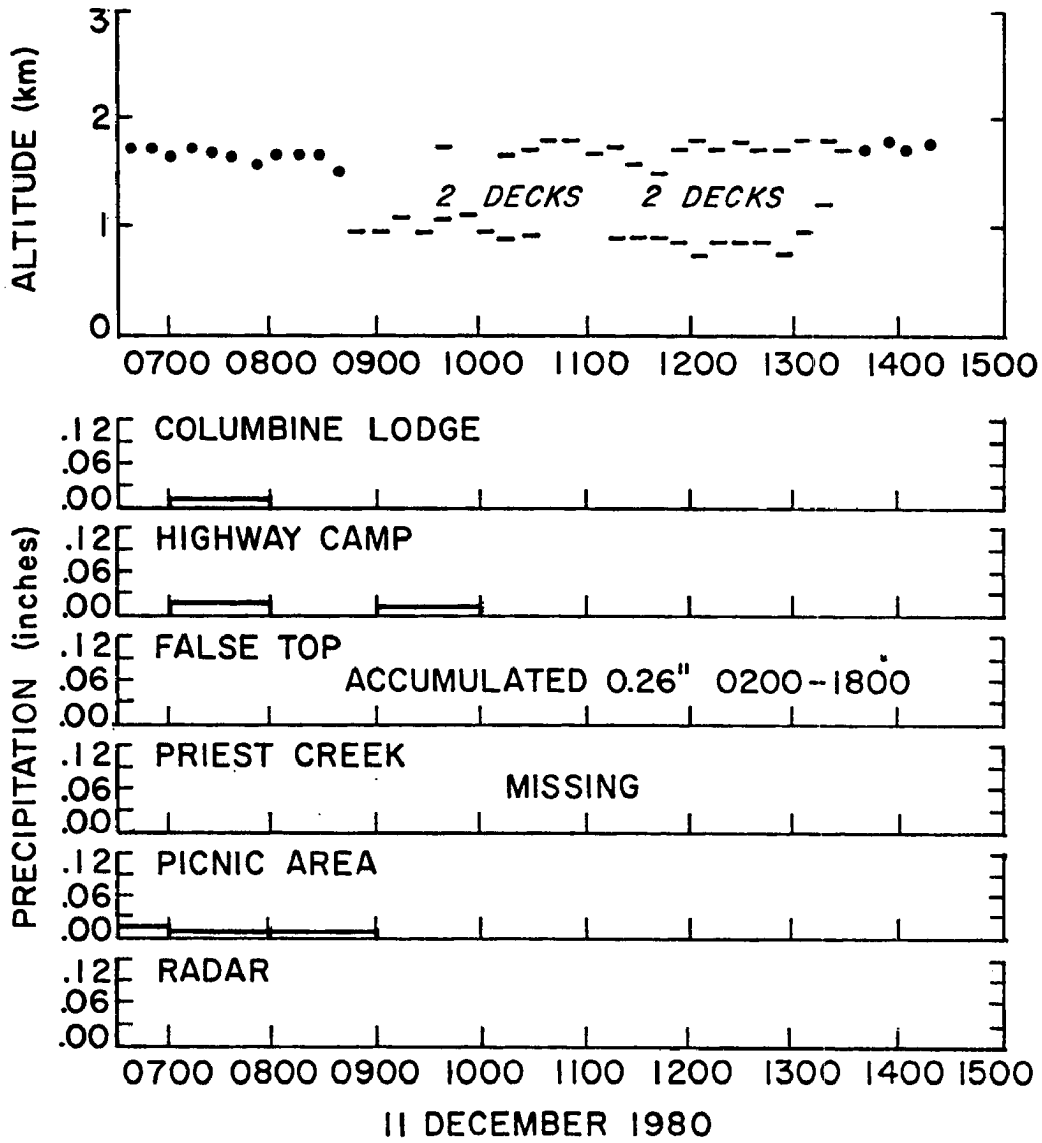


Figure 21. K-band radar cloud top heights and gauge precipitation for 11 December 0630 - 1435 MST, 1979. Note time and height scale different from fig. 19.



Colorado. By 0Z on 12/23 the surface low was positioned in Eastern Kansas and the 70 KPa low had cut off over Western Kansas. The 3Z 12/23 satellite photo indicates extensive cloudiness on the backside of the low with the highest (brightest) cloud regions in Northwest Colorado and Central Wyoming. The 12Z 12/23 70 KPa map shows a ridge building over the COSE study region, which is reflected as a surface high over Northern Utah in the 12Z surface map.

Prior to this period the Ku radar was installed at the Milner site about 40 km west of the original ski slope site (see Fig. 5). The data displayed indicate very deep cloud with low reflectivity (see Figs. 22a and 22b). After 0227 a two-deck structure develops and persists until 0733. The many isolated values printed throughout the display are probably noise due to a malfunction of the Automatic Frequency Control on the Ku set. The malfunction is not thought to have seriously affected the cloud top detection capabilities of the radar.

The maximum extent reached by cloud top during this period of observation was 6.8 km which was the highest cloud top observed in 1979. The cloud top persisted at this level until about midnight when cloud top started to decrease in altitude. By 0229 a two-deck structure developed with the top of the upper deck slowly lowering from 5 km to 4.5 km by 0712. Between 0712 and 0800 the upper deck top lowered and merged with the lower deck, below 2 km.

The temperature structure during this period remains remarkably homogeneous. Although no rawinsondes were launched at Craig after 0700, the distribution of cloud top temperature was obtained by projecting the 0700 temperature profile to the end of the observation period. Even if this technique is not representative, it is illustrated that over 80% of

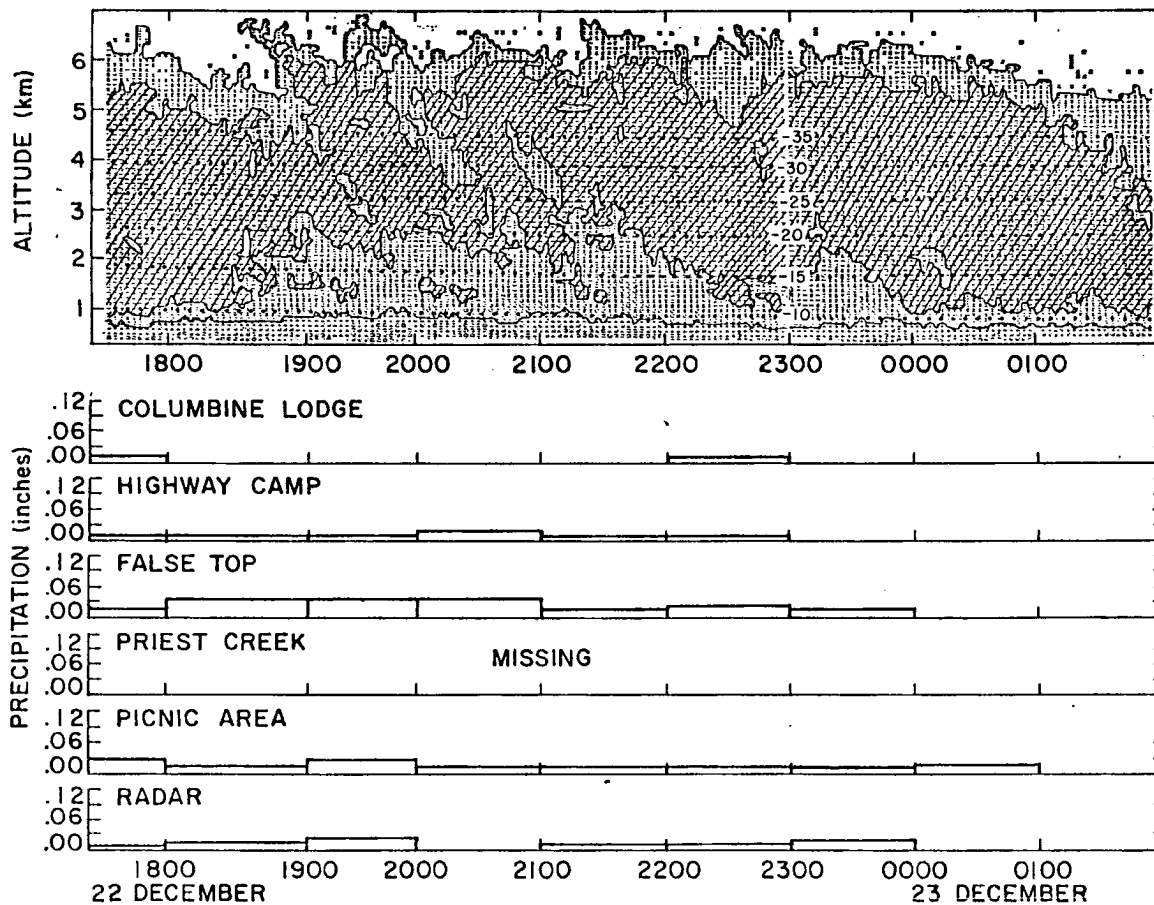


Figure 22a. Ku-band radar reflectivity and gauge precipitation records for 22 December 1730 to 23 December 0200 MST, 1979. Radar was positioned at the Milner site (see fig. 5).

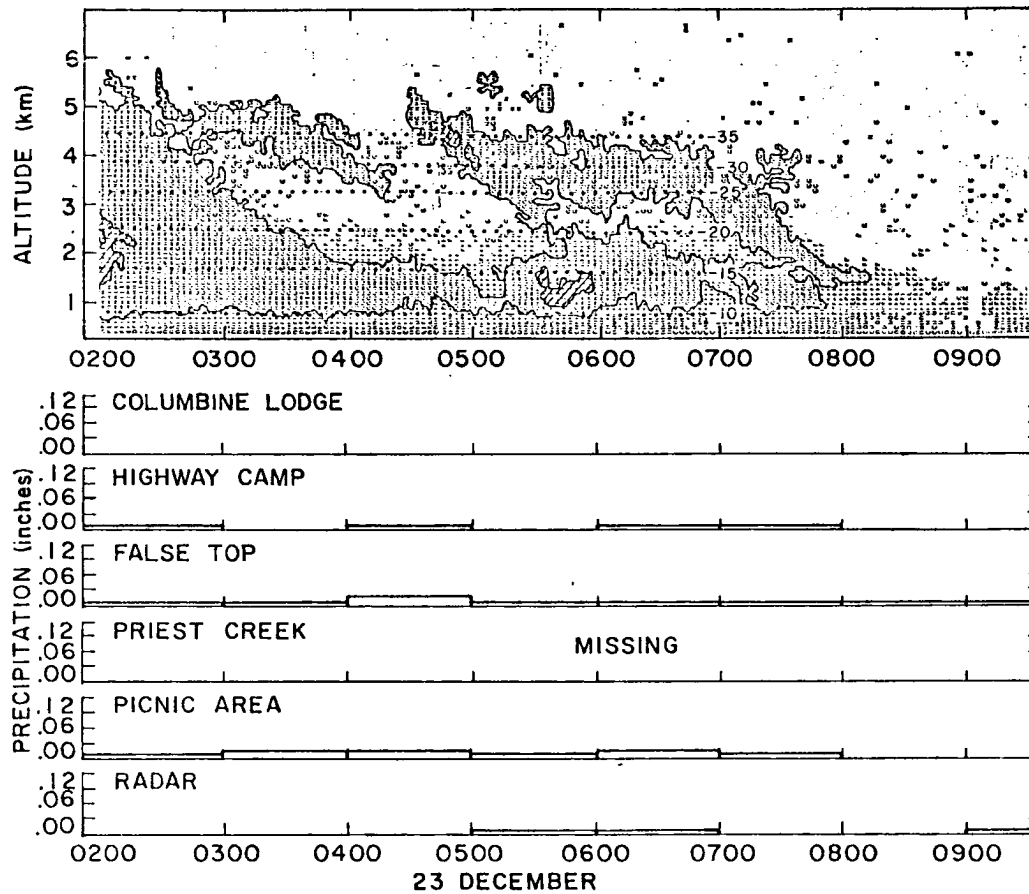


Figure 22b. Ku-band radar reflectivity and gauge precipitation records for 23 December 0200 to 0930 MST, 1979. Radar was positioned at the Milner site (see fig. 5).

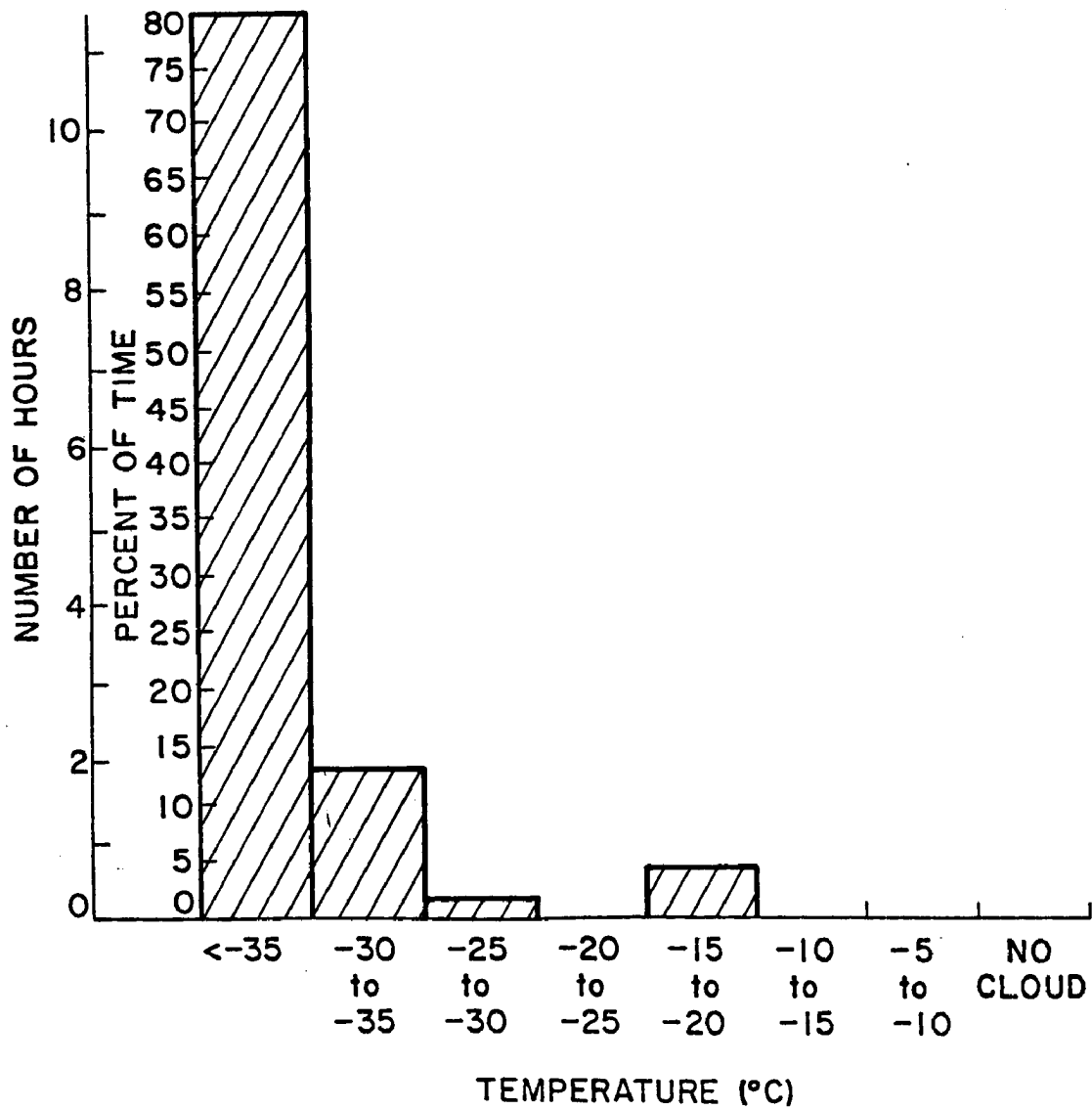


Figure 23. Cloud top temperature distribution for 22 December 1730 to 23 December 0930 MST, 1979.

the observation period contained cloud top temperatures below  $-35^{\circ}\text{C}$  (see Fig. 23).

Zones of high reflectivity are noticeably absent during this period. Reflectivity values exceeding 10 dBz only appear in a small region below 2.5 km starting 1739 and ending 1745. An upward gradient of reflectivity values again exists in the vertical from the lowest detectable range gate to approximately mid-cloud.

Continuous light precipitation was impacting the ground during this period at False Top and the Picnic Area. Light precipitation was also recorded at the other gauges although more intermittent in nature.

#### 7. Summary of Case Studies

A characteristic composite of the six cases studied would be difficult to construct; considering the variability of the cloud characteristics between cases. Instead, this section summarizes the major observations made in regard to general reflectivity patterns, cloud top height, cloud top temperatures, and zones of high reflectivity ( $> 20$  dBz). These observations are compared and contrasted to other orographic cloud studies.

One of the most striking characteristics of the general reflectivity patterns is the periodicity observed in the first stages of the first two cases. These observations may be indicative of mesoscale convective bands passing over the experimental area. Such convective bands were observed the Climax region using horizontally-scanning and vertically-pointing X-band radar (Furman, 1967). The period between the bands in the Climax area was approximately 165 minutes, which is roughly consistent with the periods observed in this study. Apparently the bands are not a consistent feature of all orographic cloud periods in

this region as they are observed less distinctly or not at all in the remaining cases.

An argument against the convective band explanation was provided by the analyses of Lee (1980) on the storm of 23-24 February 1979 (Case 2 in this study). Lee's equivalent potential temperature analysis revealed only shallow and weak convective instability during the storm at the times of rawinsonde launches. An alternative explanation for the observed periodicity may be the presence of travelling mesoscale gravity waves (Cotton, 1980).

In every vertical reflectivity profile displayed there always exists a positive reflectivity gradient upward from the lowest detected meteorological return (i.e., the maximum reflectivity level detected for each profile is never at cloud base or the minimum detectable range gate). This observation is rather surprising because reflectivity is most strongly dependent on average particle diameter, which one might have expected to be largest in precipitation zones near the ground. The phenomenon was so persistent (extending throughout the data set) that a systematic, range dependent, signal processing problem was suspected. The source of the problem was discovered by inputting time incremented power pulses directly onto the receiver data-system complex. Decreased sensitivity in the lower range bins was discovered, only manifested when the transmitter was operating (see Fig. 24). On the basis of these tests it was concluded that the nature of the reflectivity pattern was due to decreased sensitivity in the transmitter-receiver tube during the recovery time after the transmitted pulse. Preliminary tests indicated that the greatest loss in sensitivity was 12 dB at 600 meters. Sensitivity increased exponentially with height above that level (see Fig.

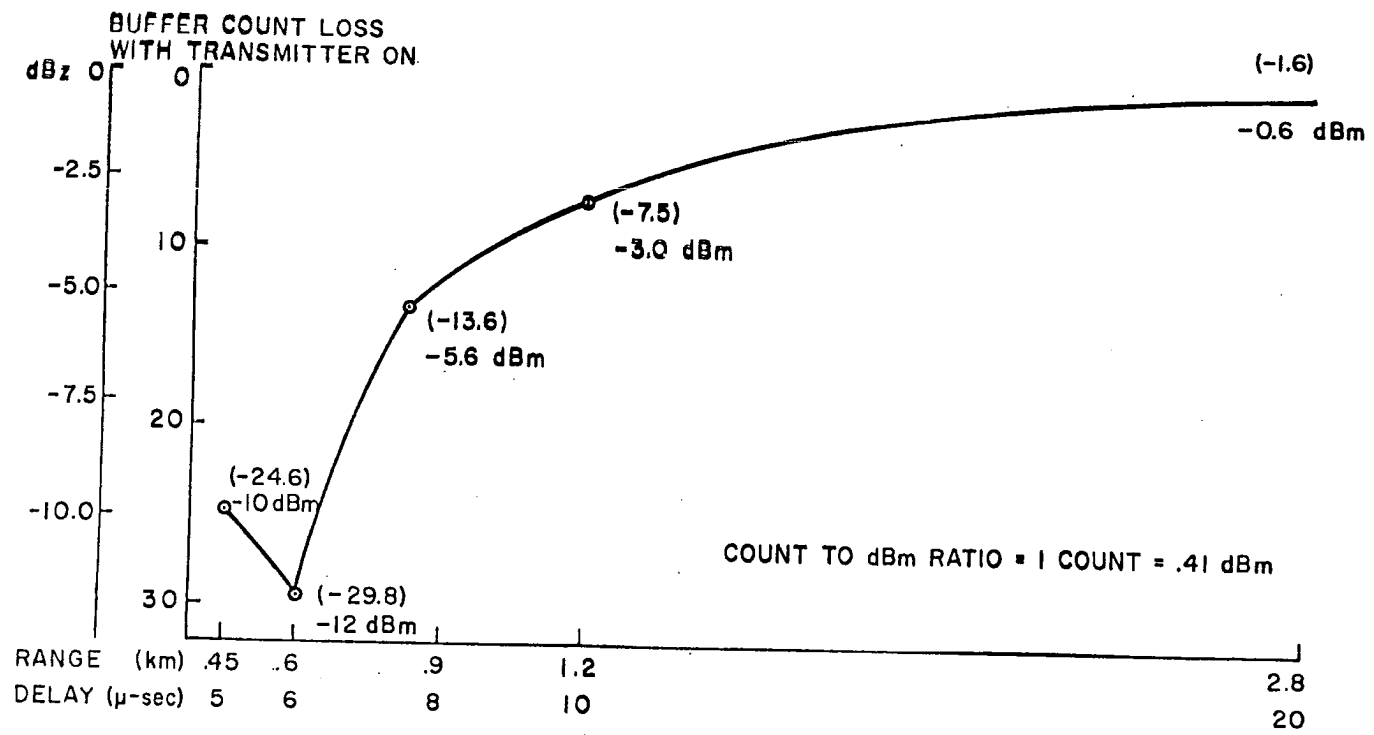


Figure 24. Sensitivity loss with height due to TR tube recovery in the Ku-band radar.

24). This means that the upward gradient in reflectivity from the lowest detectable range bin was artificial. Because of the exponential increase in sensitivity with altitude, the system effect is not thought to have impaired the ability of the Ku-band set to detect cloud top height. The effect most strongly obscured reflectivity magnitudes at lowest altitudes; and renders cloud base information below about 1.6 km unreliable, and likely to be lower in altitude than depicted.

The maximum cloud top height observed during the present study was 7 km AGL (9.1 km MSL) during case 6. Cloud tops usually were observed to attain maximum vertical altitude near the beginning of the observation periods, and generally lowered during the course of the storm; attaining minimum sustained altitude near the time of dissipation. These observations are in general agreement with the findings of Cooper and Marwitz (1980) who used rawinsonde, aircraft and ground observations from 12 case studies to create a generalized storm scenario for the San Juan region. They attribute the cloud top change to the changing thermodynamic structure of the storm; associating the deep clouds at the beginning of the storm with the synoptic disturbance, and noting that the shallower clouds in the latter stages of the storm were "more orographic". Although the behavior of cloud top in the present study followed this general trend, considerable shorter time scale variations in cloud top height existed.

This study also illustrates two distinct cases of persistent low cloud (case 4 and K-band data following case 5) following a deeper cloud regime. This phenomena was apparently not observed in the San Juan region, as the final storm stage ("dissipation") was characterized by



"isolated convective cells" in the University of Wyoming studies (Cooper and Saunders, 1980).

Cloud top temperatures during most of the periods observed were colder than  $-35^{\circ}\text{C}$ . Generally cloud top temperatures warmed as cloud tops lowered toward the end of the storm periods. Cloud top temperatures varied primarily with cloud top height changes, as the temperature levels at cloud top height changed only very gradually. Warmest prolonged cloud top temperatures occurred in case 4, where temperatures were mostly warmer than  $-20^{\circ}\text{C}$ .

Zones of reflectivity higher than 20 dBz appear most frequently in the first three case studies. The zones seem to be associated with a relative increase in cloud top height and appear in the lower center portion of roughly concentric isoechoes. The depth of the zones varies rapidly with time, and can extend over 3 km. No particular preferred temperature region for the appearance of the high reflectivity zones exists, except that the zones mostly reside at levels warmer than  $-30^{\circ}\text{C}$ . These high reflectivity zones probably extended to ground level in actuality, but were not detected because the Ku-band radar sensitivity problem (described previously) affected the lower range bins the most. The periodicity with which these zones appear, as well as their relation to cloud top height changes, suggest that they may represent embedded convection. Although contrary to equivalent potential temperature analysis, this interpretation would be consistent with the results of Moninger (1980) in the Sierras; in which high reflectivity zones were highly correlated to updraft regions. The increased reflectivity may be due to agglomerate particles existing in this region.

Zones of high reflectivity were noticeably absent during case 6, prior to which Ku-band radar set had been moved further westward from the ridge crest to the Milner site (see Fig. 5). Despite relatively high cloud top, reflectivity values during the period never exceeded 15 dBz and only briefly exceeded 10 dBz. If not due to decreased sensitivity from moving the radar, this decreased reflectivity may be due to an overall negative horizontal gradient of reflectivity upwind from the ridge crest, which would be consistent with the results of Furman (1967). Furman found maximum reflectivities at or near ridge crests in the Climax area while scanning horizontally with an X-band radar set. This gradient may be associated with the distribution of orographic lift upwind from ridge crest. Zones of high reflectivity were also absent from case 4 during the persistent low cloud regime.

No continuous well-defined gradient of precipitation rates with height was observed from the gauge records. During the onset of a short wave (case 5) precipitation first occurred on the lee and upper elevation stations, then began at lower elevations. No consistent distinct correlation was observed between precipitation patterns and cloud top height or zones of high reflectivity; however, no statistical tools were used in this study to determine such correlations.

## B. OBJECTIVE 2

### - Estimating Vertical and Horizontal Motions in Cloud

The most extensive Doppler coverage within the data set was during the storm of 12/10 - 12/11, 1979 (case 5 under the previous objective). The X-band radar operated in vertically pointing Doppler mode from 2256 to 2346 on 12/10; and 0104 to 0234 and 0409 to 0604 on 12/11. The

figures in this section represent vertical profiles of vertical velocities and reflectivities sampled at selected intervals during these periods. What the radar actually can measure is  $w$ , where  $w$  (vertical velocity) =  $v_T$  (precipitation vertical velocity) +  $w$  (air velocity). Each profile represents a five minute average. Vertical profiles of crystal fall velocities obtained from a crystal growth model are presented for storm conditions existing at 2300 on 12/10, and 0200 and 0500 on 12/11. Included with the presentation of graphics for each Doppler observation period is a written summary of the changes in vertical velocity and reflectivity. A discussion of the role of the dynamic component in the observed vertical velocity patterns is then presented.

Conical VAD scans with the dish tilted  $45^\circ$  from vertical were taken at 2249 on 12/10; and 0058 and 0622 on 12/11. The resulting profiles of vertical profiles of horizontal velocity and direction are presented, along with rawinsonde observations of wind speed and direction at 2300 on 12/10; and 0200, and 0500 on 12/11.

### 1. Vertically Pointing Doppler Observations

#### First Doppler Observation Period 2256 - 2346 10 December 1979

At lower levels, Doppler vertical velocity profiles ( $w$ ) taken during this period are characterized by relative maximums of downward velocity and rapid changes in profile shape between profiles (see Fig. 25). Maximum downward velocities in the first displayed profile (2300 - 2305) were over 1.7 m/s at 375 m AGL. In contrast, the second profile presented (2315 - 2320) shows maximum downward velocities of 1.3 m/sec at 1525 and 1700 m AGL. Although the data used to construct the second profile was taken only 15 minutes after the data used for the first profile, downward vertical velocities in the second profile are shown to

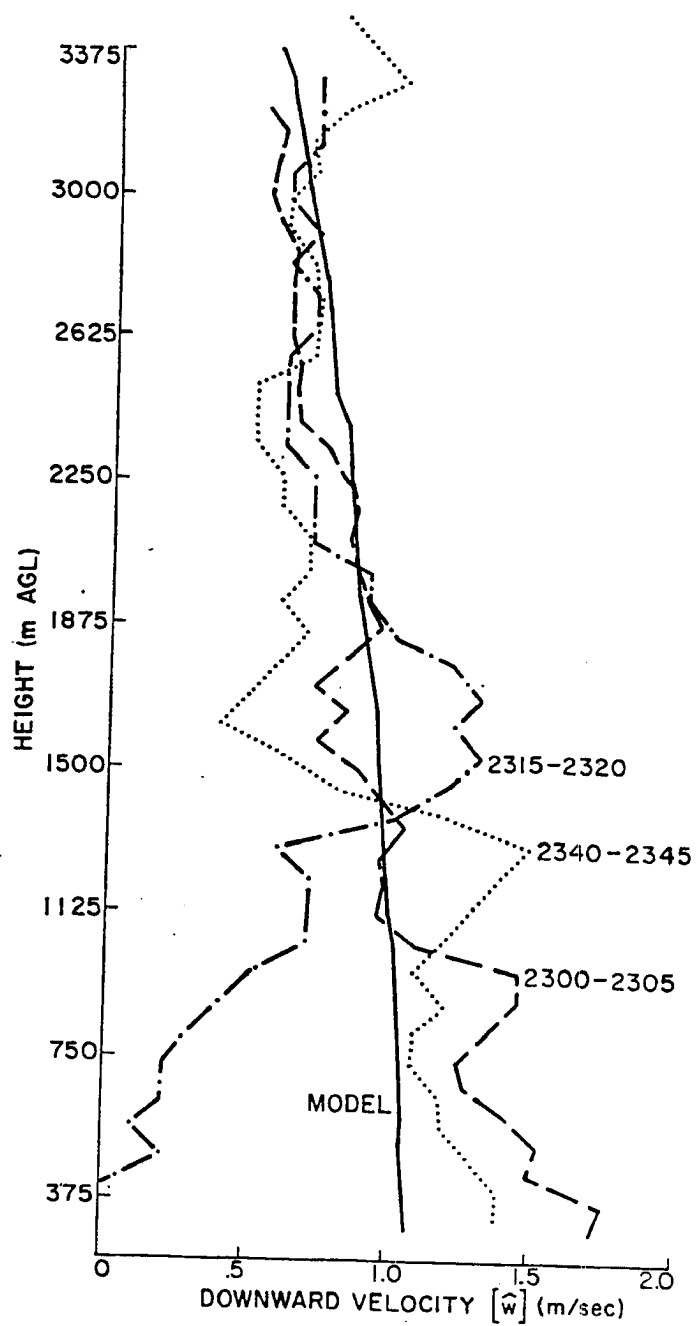


Figure 25. Vertical profiles of  $\hat{w}$  averaged over three 5-minute periods; 2300 - 2305, 2315 - 2320, and 2340 - 2345 MST on 10 December, 1979; as determined by vertically-pointing X-band Doppler radar; and model-predicted crystal fall velocity ( $V_T$ ) from 2300 MST 10 December rawinsonde data.

decrease below 1525 m AGL. The third displayed profile (2340 - 2345) shows sharply increasing downward velocities from about 1600 to 1300 m AGL where the maximum value of 1.5 m/sec exists. Above 1800 m AGL, the three profiles depict relatively consistent downward velocities around 0.6 m/s.

A vertical profile of model generated crystal fall velocities created from rawinsonde data at 06Z (2300 MST) is presented in Fig. 25. In the first vertical velocity profile displayed, the model represents observed downward velocities fairly accurately (within 0.2 m/s) above 1050 m AGL but underestimates observed downward velocities by as much as 0.7 m/s at 375 m AGL. The model is most representative of velocities observed in the second profile (within 0.2 m/s) above 1875 m AGL. At about 1700 m AGL the model underestimates downward velocities by about 0.45 m/s. At 375 m AGL observed average vertical velocity is zero, resulting in an overestimate of downward velocity in the model by its calculated value (about 1.1 m/s). The model overestimates observed downward velocities in the third profile by 0.35 m/sec at 2350 m AGL and by 0.5 m/s at 1650 m AGL; and underestimates observed downward velocities by 0.4 m/s at 3300 m AGL, 0.5 m/s at 1300 m AGL, and 0.3 m/s at 400 m AGL.

The three corresponding reflectivity profiles display a greater degree of homogeneity in time than the  $\hat{w}$  profiles (see Fig. 26). All three profiles show a positive reflectivity gradient directed upward from the minimum range level detected, culminating in a zone of highest reflectivities extending from about 1700 m AGL to about 2250 m AGL, above which reflectivity values generally decreased with height. Comparing only the reflectivity and vertical velocity profiles taken 2315

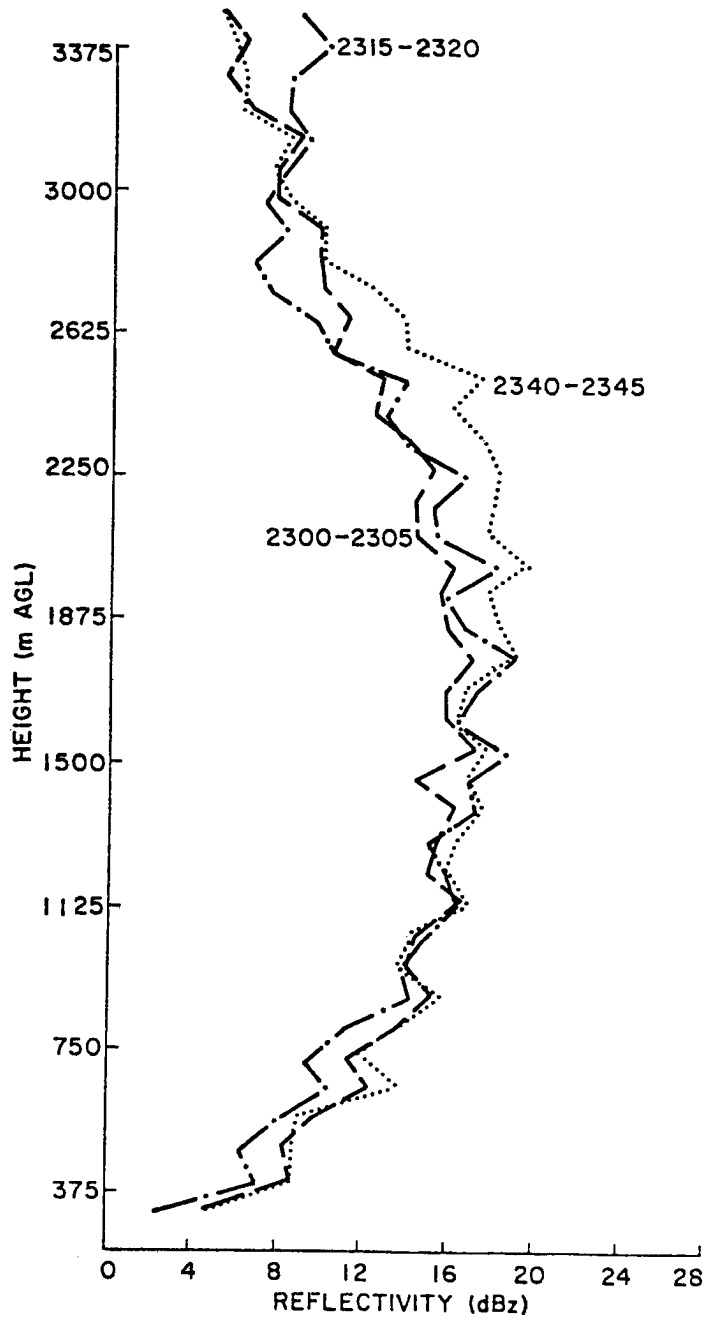


Figure 26. Vertical profiles of reflectivity averaged over the corresponding 5-minute periods displayed in fig. 25, as determined by vertically-pointing X-band Doppler radar.

to 2320, one might be tempted to conclude that a strong correlation exists between vertical profiles of vertical velocity and reflectivity. This correlation is not at all evident, however, during the other two sampling periods. Note, for example the region below 1125 m AGL in the first profile pair displayed, where an inverse relationship exists between downward vertical velocity and reflectivity. The shape of the average vertical velocity profile during 2340 - 2345 bears little resemblance to the shape of its corresponding average reflectivity profile in any region.

Second Doppler Observation Period 0104 - 0234 11 December 1979

By the second Doppler observation period, downward velocities above 1.8 km have increased, so that relative maxima in the individual profiles are shifted upward and now appear above 2000 m AGL (see Fig. 27). The maximum downward velocity observed for the period 0119 - 0124 was 1.65 m/s at 2100 m AGL. The minimum downward velocity observed for this period was about 0.95 m/s at 1500 m AGL; producing a relatively homogeneous profile of downward velocity with height. The profile representing the period 0209 - 0214 shows that downward velocities below 1500 m AGL have decreased relative to those in the previous display. At about 2500 m AGL, the maximum downward velocity of 1.5 m/s appeared. By 0224 - 0229 vertical velocities below 1500 m AGL had further decreased in magnitude, while velocities at upper levels have increased slightly creating a more pronounced maximum at 2300 m AGL of 1.85 m/s.

The crystal growth model taken from 09Z (0200 MST) rawinsonde data generally significantly underestimates observed downward velocities above 1875 m AGL during this period (see Fig. 27). The maximum downward velocity for 0224 - 0229 m AGL is 1.1 m/s greater than the model alone

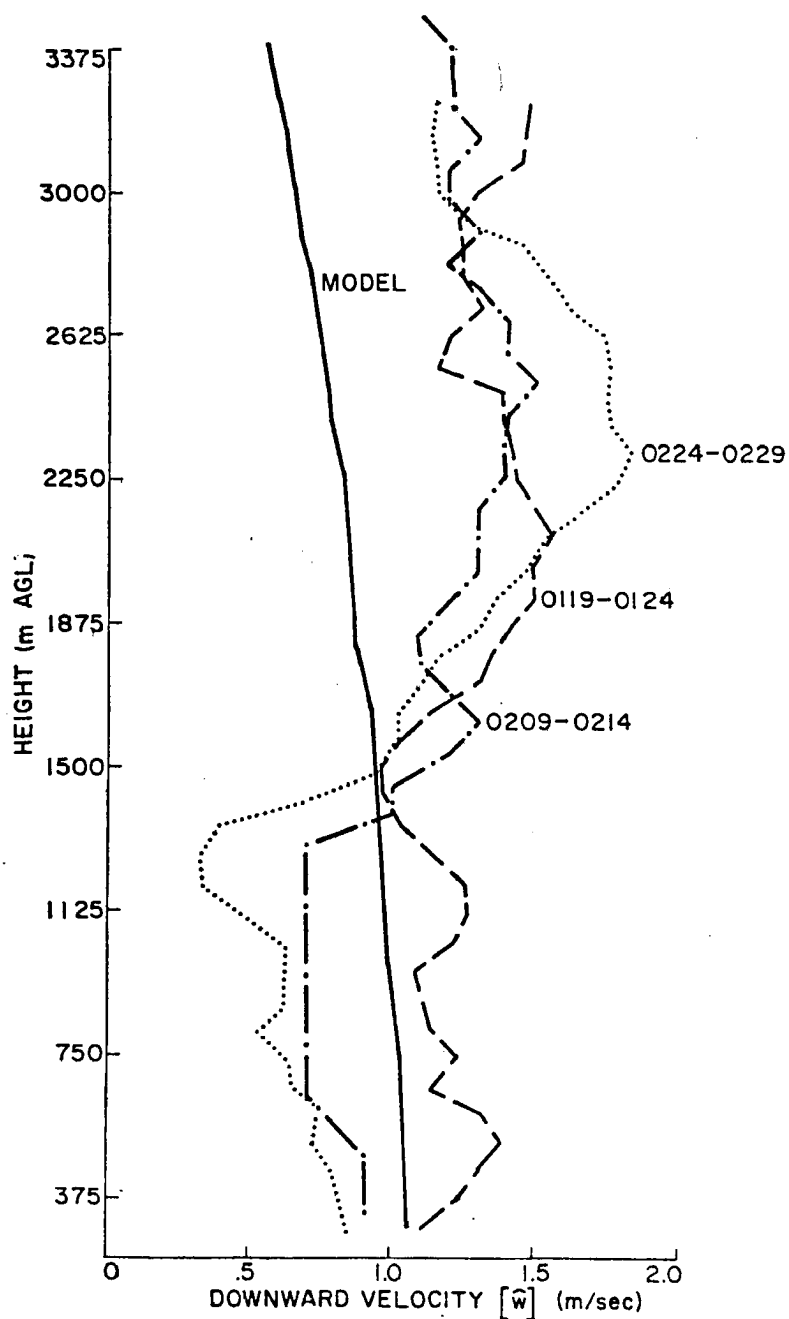


Figure 27. Vertical profiles of  $\hat{w}$  averaged over three 5-minute periods; 0119 - 0229 MST, 11 December, 1979; as determined by vertically pointing X-band Doppler radar; and model-predicted crystal fall velocity ( $V_T$ ) from 0200 MST 11 December rawinsonde data.



predicts. Below 1500 m AGL the model slightly underestimates the average downward velocities during 0119 - 0124, and overestimates by as much as 0.6 m/s the downward velocities observed by 0224 - 0229.

During the second Doppler observation period, the shape of the reflectivity profiles indicate little change, except that the magnitude of reflectivity is slightly higher in the region around 2250 m AGL in the profile for 0119 - 0124 (see Fig. 28). Again, no consistent correlation seems to exist between the shapes of the individual Doppler velocity profiles and their corresponding reflectivity profiles. In a more general way, however, both reflectivities and downward vertical velocities seem to have increased in the region from 2250 to 3000 m AGL between the first and second observation periods.

#### Third Doppler Observation Period 0409 - 0604 11 December 1979

The last period of Doppler observation during the storm is characterized by the development and persistence of a pronounced maximum in downward velocity centered in the region around 2250 m AGL (see Fig. 29). The distinct maximum in downward velocity (1.8 m/sec) at 2250 m AGL in the data set from 0409 to 0414 may indicate that this feature persisted after forming before 0224 - 0229. In the first profile, sharp increases in downward velocity appear below 500 m AGL. This increase in downward velocities at lower levels disappears in the interval between the first and second profiles, while the maximum at 2250 m AGL persists at 1.8 m/s. Downward velocities from 1200 m AGL to 2175 m AGL increase slightly between the first and second profiles. By the period from 0445 - 0449 the maximum at 2250 m AGL exceeds 2 m/s, while velocities below 1350 m AGL tend to increase with depth. In the fourth profile displayed (0524 - 0529) the feature at 2250 m AGL recedes to 1 m/s while

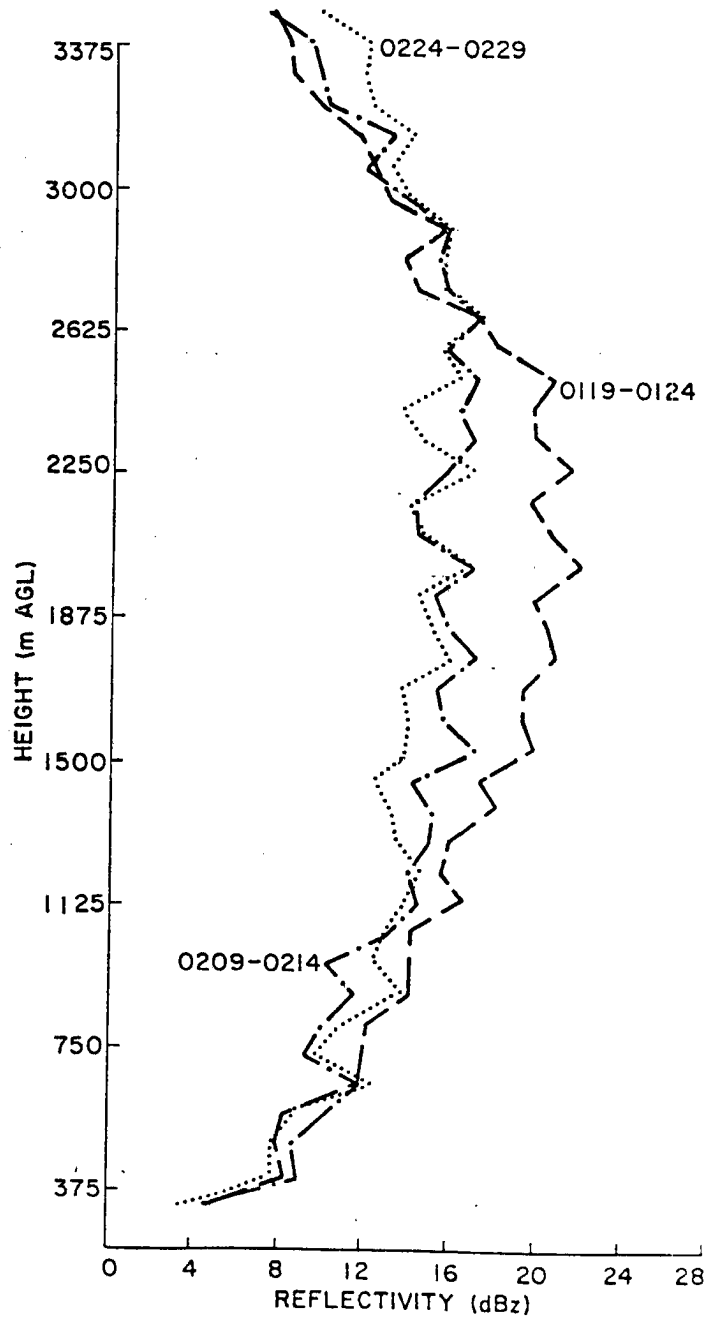


Figure 28. Vertical profiles of reflectivity averaged over the corresponding 5-minute periods displayed in fig. 27, as determined by vertically pointing X-band Doppler radar.

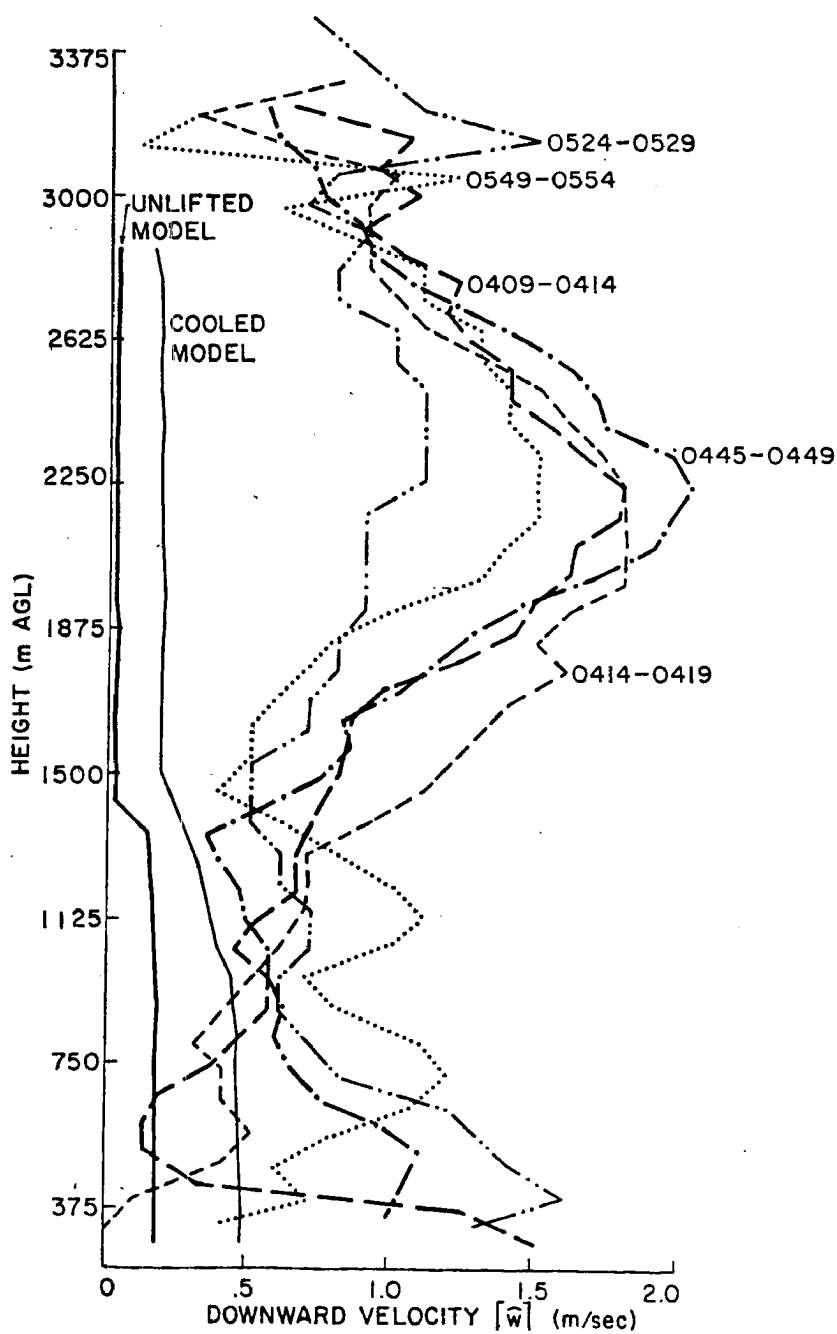


Figure 29. Vertical profiles of  $\hat{w}$  averaged over five 5-minute periods; 0409 - 0419, 0445 - 0449, 0524 - 0529, 0549 - 0554 MST on 11 December 1979; as determined by vertically-pointing X-band Doppler radar; and model-predicted crystal fall velocity profiles ( $V_T$ ) from the unlifted 0500 MST 11 December rawinsonde data, and from the rawinsonde data cooled  $2^\circ\text{C}$  at every level.

velocities at lower levels increase such that the maximum of 1.6 m/s occurs at about 400 m AGL. In the final profile displayed, the maximum downward velocity of 1.5 m/s is re-established at 2250 m AGL. During this period a double-peaked feature appears below 1500 m AGL; with submaxima of 1 m/s at 1125 m AGL and of 1.2 m/s at 750 m AGL.

The model constructed from 12Z (0500 MST) radiosonde data tends to underestimate observed downward velocities at all levels. The model was reconstructed using a scheme which represented  $2^{\circ}\text{C}$  cooling at all levels, although the resulting downward velocities still considerably underestimated observed downward velocities particularly in the region around 2250 m AGL (see Fig. 29).

Reflectivity profiles from 0409 - 0414 and 0414 - 0419 retain the general shape of reflectivity profiles from previous periods (see Fig. 30). No distinct increase in reflectivity appears at 2250 m AGL where the maximum downward velocity exists in these two periods. However, a corresponding maximum in reflectivity values does exist in the reflectivity profile for the period from 0444 - 0449 at 2250 m AGL. The general shapes of the reflectivity and velocity profiles correspond well above 1875 m AGL. Below 1125 m AGL a negative correlation exists between the reflectivity and velocity profiles. The final two profiles of reflectivity clearly indicate a double maximum shape, which roughly describes the shapes of their corresponding velocity profiles.

#### Summary of Observations in regard to the role of the Dynamic Component

If the air velocity component of downward velocity structure was negligible, one would expect that 1) The observed downward Doppler velocities could be fairly well modelled by simulating crystal fall velocities in the same growth environment and 2) The shapes of the profile of

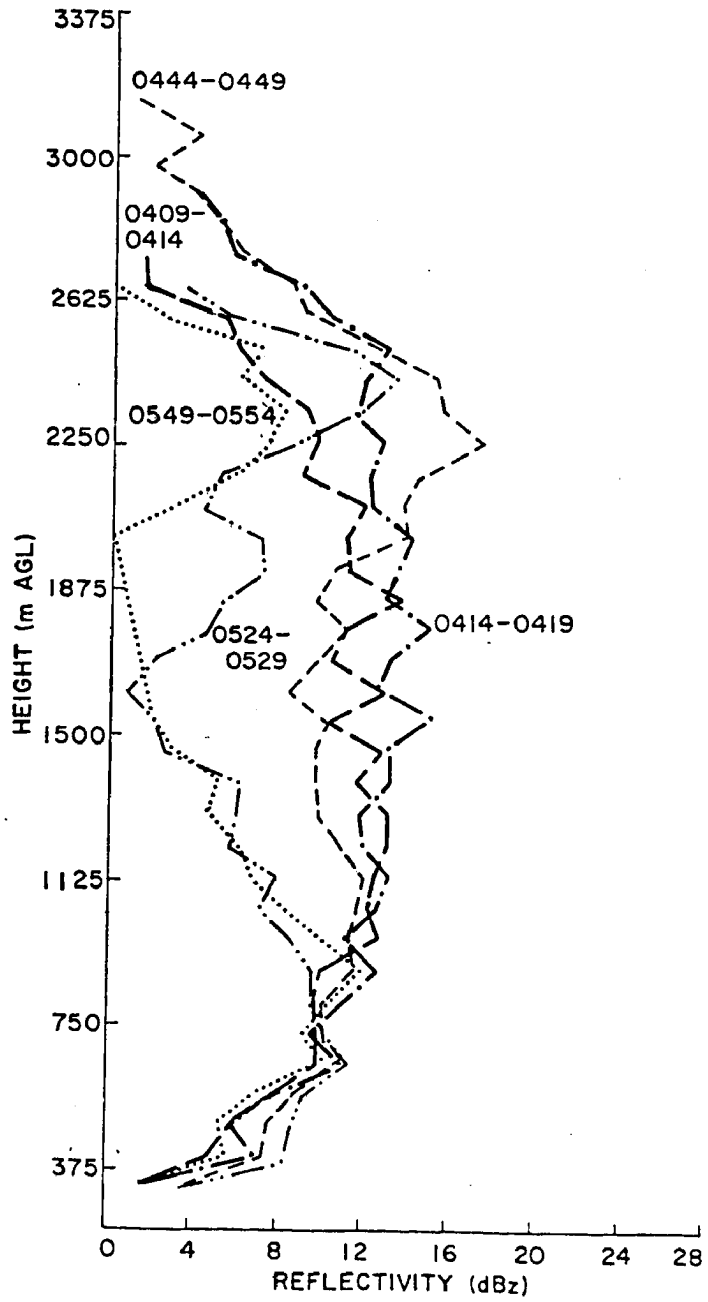


Figure 30. Vertical profiles of reflectivity averaged over the corresponding 5-minute periods displayed in fig. 29, as determined by vertically pointing X-band Doppler radar.

the observed downward velocities would be similar to the shapes of the corresponding reflectivity profiles, since both should be primarily a function of crystal size, shape and degree of riming. Generally, two regions in the vertical exist where these two criteria fail to be met; below 1300 m AGL and in the vicinity of 2250 m AGL.

Large fluctuations exist in the times between display periods in Doppler-assessed downward velocities below about 1300 m AGL. These variations are not seen in the corresponding reflectivity profiles. Instead the reflectivity profiles have consistent mid-cloud maxima. The most probable explanation for the disparity between the vertical profiles of reflectivity below 1300 m AGL, is a reduction in sensitivity to reflectivity detection in the lower range gates similar to the effect observed in the Ku-band set discussed previously. The decreased sensitivity (due to T-R tube switching recovery time) is at least plausible because the Ku and X-band sets each used a single antenna for transmitting and receiving. Comparison with K-band data is not possible during these periods because the data system configuration precluded recording K-band data while recording X-band data in Doppler mode. The decreased sensitivity at low levels may have affected the X-band radar's ability to measure vertical velocities as well.

After the first Doppler observation period, observed vertical velocities increased at upper levels, and a maximum at about 2250 m AGL persists in the storm after the period 0224 - 0229. Ice crystal fall velocity models from data at 09Z and 12Z indicate that this feature is not associated with more rapid diffusional growth above this level. Riming above this level is unlikely as temperatures were probably below  $-18^{\circ}\text{C}$ . A corresponding maximum in the reflectivity profiles is not observed

until the 0444 - 0449 period, after which the shapes of the reflectivity profiles reasonably match the shapes of the observed downward velocity profiles. The origin of this phenomenon is probably also rooted in air motions, possibly being the downward portion of a stationary wave. This persistent downward motion may have played a key role in the establishment of a low cloud regime following the last Doppler observation period (see presentation of results for case 5 under objective 1).

## 2. VAD Scan Observations

The VAD scan at 2249 indicates a general backing of the horizontal wind with height up to about 1875 m AGL (see Fig. 31). Above 1875 m the horizontal winds remained southwesterly to the top of the profile. VAD wind speeds are in the vicinity of 5 m/s below 1500 m AGL, and increase with height between 1500 and 2500 m AGL where a maximum value of 20 m/s is displayed (see Fig. 32). Velocities then decrease slightly with height, reach the maximum value again at 3160 m AGL, then decrease rapidly with height.

Wind direction as obtained by rawinsonde (2300 MST) agrees with VAD-derived wind directions to within  $10^\circ$ , except at about 1500 m AGL where the VAD shows winds from  $264^\circ$  and the rawinsonde shows winds from  $230^\circ$  (see Fig. 31). The VAD profile underestimates rawinsonde velocities by about 6.5 m/s at 374 m AGL, but the agreement becomes better above this level as rawinsonde velocities decrease with height while VAD velocities remain roughly the same with height (see Fig. 32). From 1500 to 2550 m AGL the horizontal velocities obtained at the two sites agree to within 2 m/s. Above 2550 m AGL, however, fluctuations of horizontal velocity exist in the VAD data which are not reflected in the steady acceleration with height in the rawinsonde data.

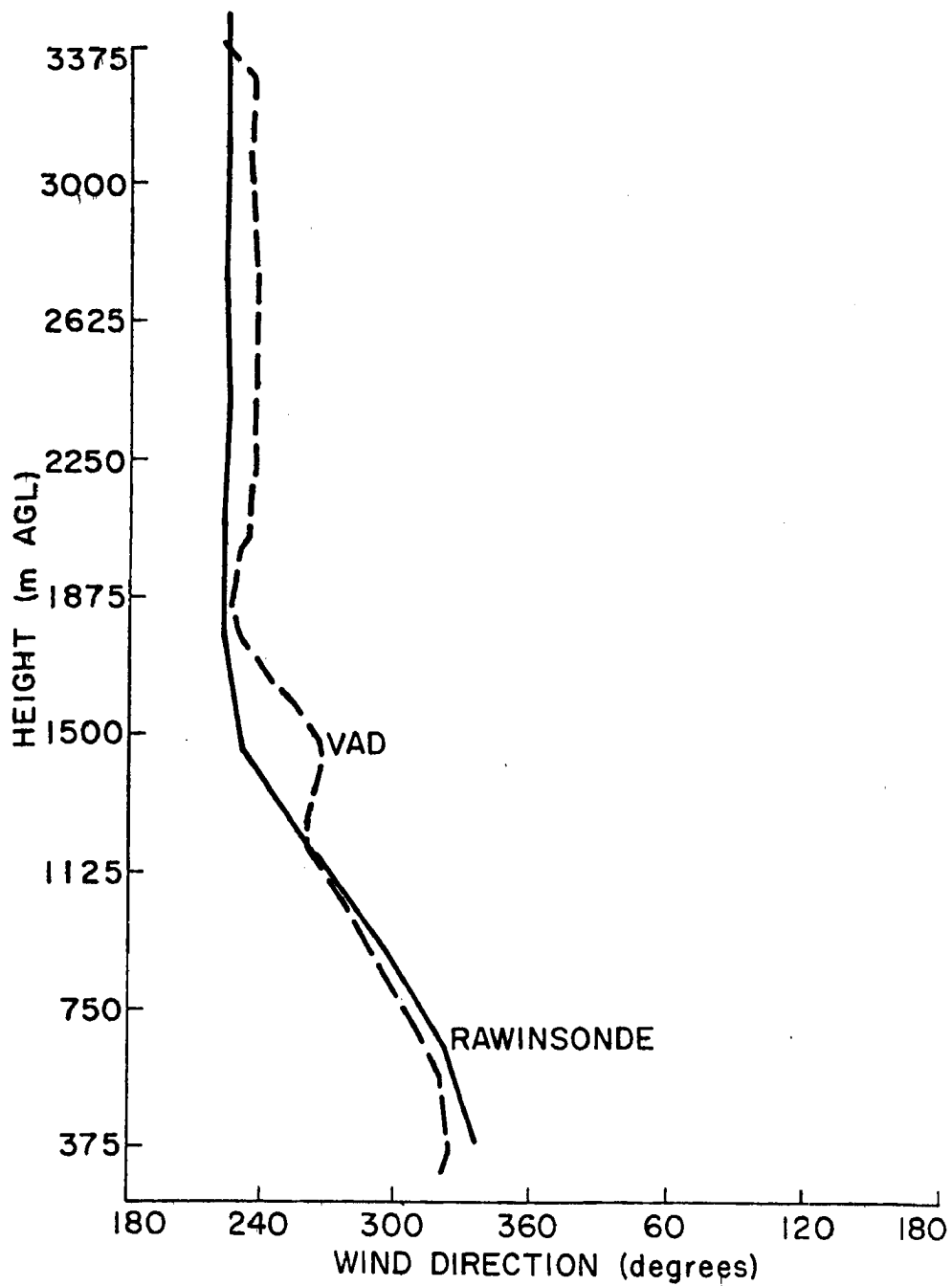


Figure 31. Vertical profiles of horizontal wind direction as assessed by X-band Doppler radar in VAD mode at  $45^{\circ}$  elevation 2249 MST 10 December 1979, (---), and by rawinsonde launched 2300 MST 10 December, 1979 (—).



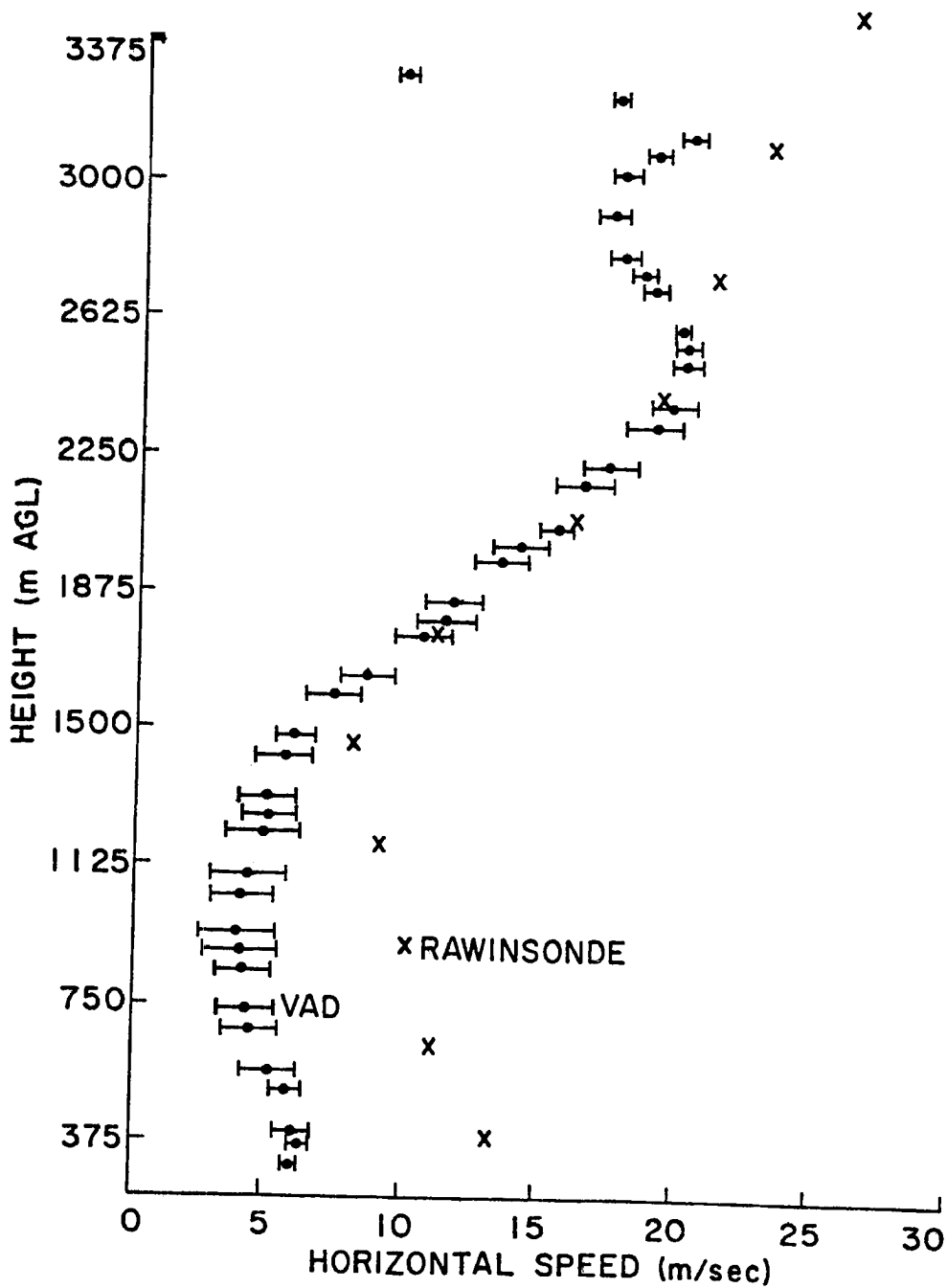


Figure 32. Vertical profiles of horizontal wind speed as assessed by X-band Doppler radar in VAD mode at  $45^{\circ}$  elevation 2249 MST 10 December, 1979 ( $\bullet$ ) and by rawinsonde launched 2300 MST 10 December, 1979 (X).

The VAD profile taken at 0058 again indicates a backing of the horizontal wind with height, although at this time the region over which backing occurs is from 750 to 2175 m AGL (see Fig. 33). Above 2175 m AGL, horizontal winds remain from a southwesterly direction as in the first VAD profile. VAD wind speeds at 375 m AGL are over 10 m/s, and observed velocities decrease with height to a value below 4 m/s at 1750 m AGL (see Fig. 34). Above 1750 m AGL horizontal velocities increase with height to a maximum value of about 20 m/s at 2600 m AGL. Above 2650 m AGL, the error bars on horizontal velocity fill the ordinate, so that neither direction nor velocity observations at these levels are reliable. Because the dish was tilted at 45° from vertical, the altitude levels are also indicative of the radius of the horizontal circumference around the radar over which the data was taken. Reflectivities in large portions of the circumferences with radii greater than 2650 m probably fell below threshold values, particularly because this region is near the cloud top detected directly over the radar before conversion to Doppler mode. This was probably the origin of errors in horizontal wind direction and velocity assessment above this level.

In the last 45° VAD scan taken at 0622, large error bars indicated non-reliability in the data above 1500 m AGL so that the data was not displayed above this level (see Fig. 35). VAD wind directions below 375 m probably contain an easterly component although wind velocities are less than 2 m/s at this level (see Fig. 36). Winds veer with height from the minimum detectable range bin to 1125 m AGL. Light drainage winds at the surface from a ridge crest to the east or south (see Fig. 5) would be consistent with these observations. Wind speeds at this time have reduced considerably; being under 10 m/s over the depth of the detectable cloud.

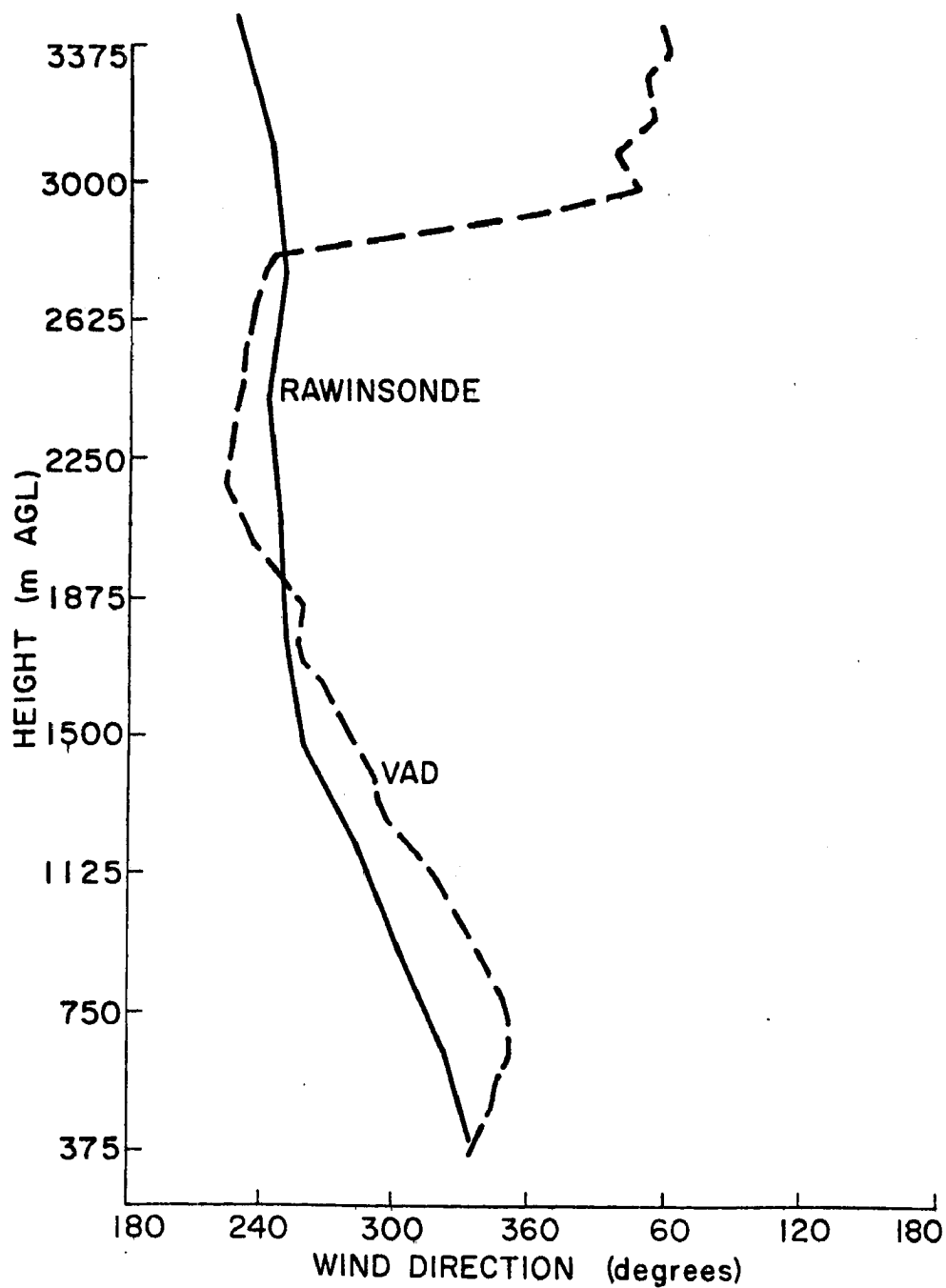


Figure 33. Vertical profiles of horizontal wind direction as assessed by X-band Doppler radar in VAD mode at  $45^{\circ}$  elevation 0058 MST, 11 December 1979 (---), and by rawinsonde launched 0200 MST 11 December (—).

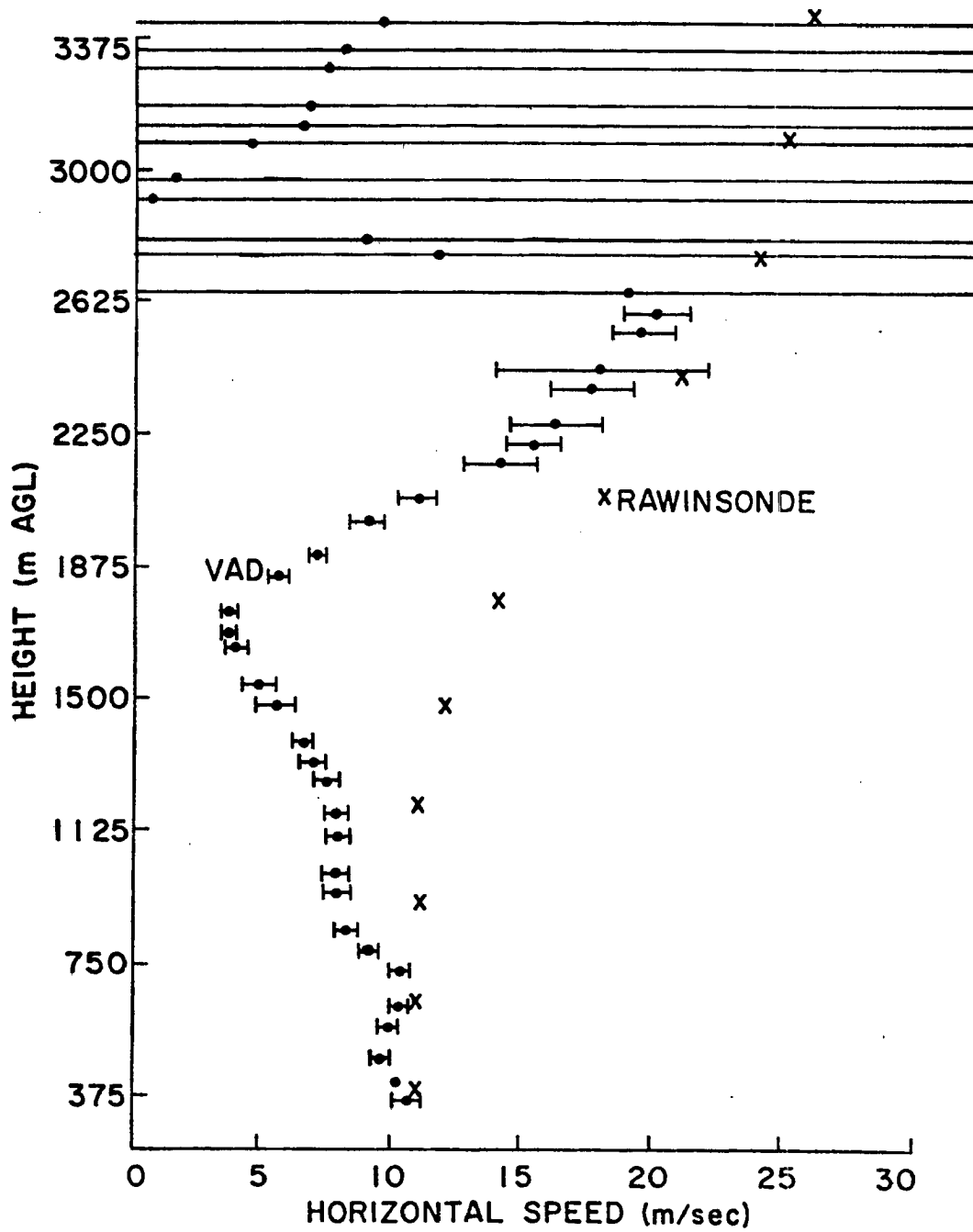


Figure 34. Vertical profiles of horizontal wind speed as assessed by X-band Doppler radar in VAD mode at  $45^{\circ}$  elevation 0058 MST 11 December, 1979 ( $\bullet$ - $\bullet$ ), and by rawinsonde launched at 0200 MST 11 December, 1979 (X).

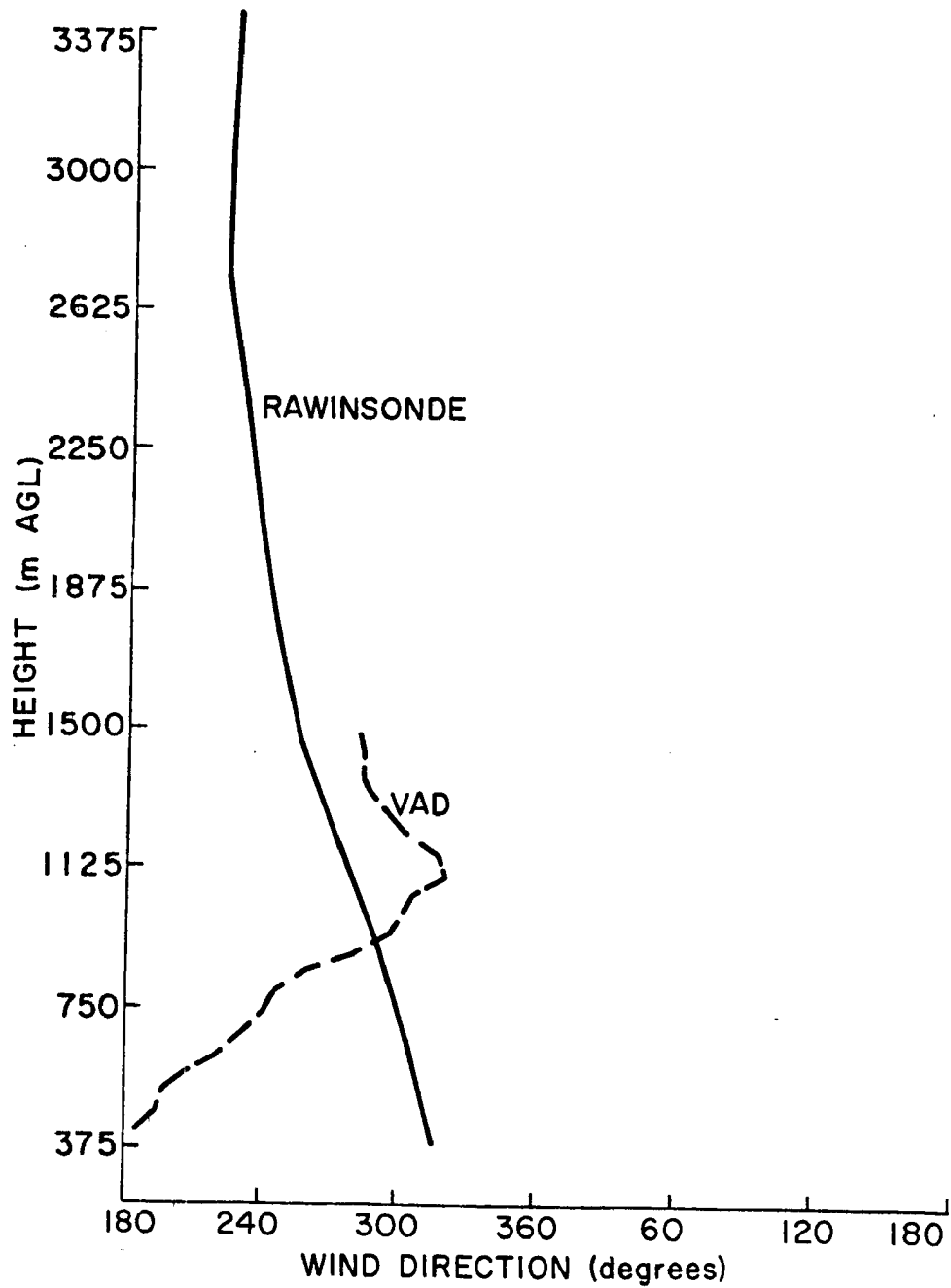


Figure 35. Vertical profiles of horizontal wind direction as assessed by X-band Doppler radar in VAD mode at  $45^{\circ}$  elevation 0622 MST, 11 December 1979, (---), and by rawinsonde launched 0500 MST 11 December, 1979, (—).

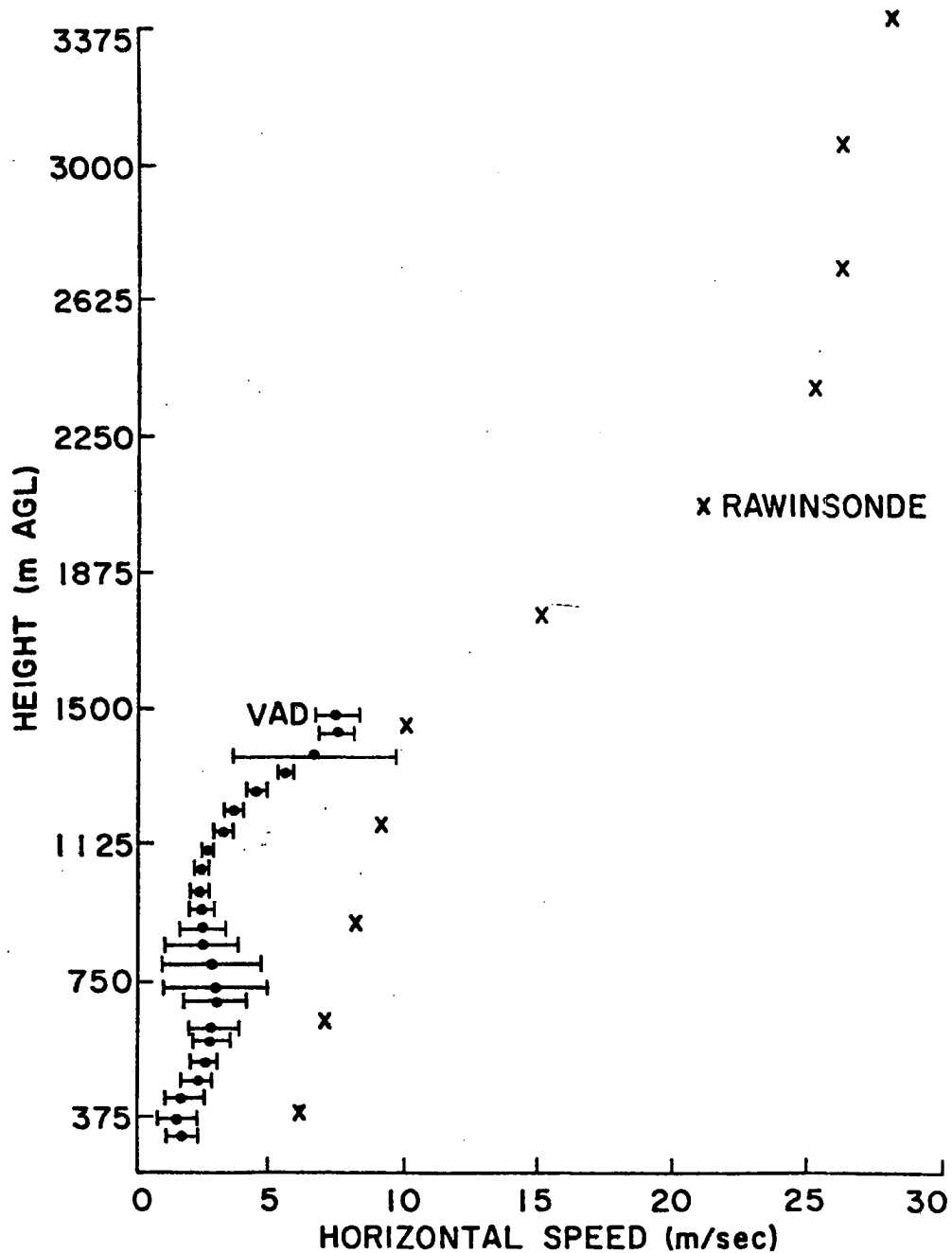


Figure 36. Vertical profiles of horizontal wind speed as assessed by X-band Doppler radar in VAD mode at  $45^\circ$  elevation 0622 MST, 11 December, 1979, ( $\bullet$ — $\bullet$ ), and by rawinsonde launched 0500 MST 11 December 1979 (X).

The 12Z rawinsonde data indicates wind direction backing with height at Craig from 375 m to 2400 m AGL (see Fig. 35). Rawinsonde detected horizontal wind speeds are greater than those observed by VAD as much as 5 m/s (see Fig. 36). The differences observed may be a function of time rather than location, because the observations were separated by about 1.5 hours.

### C. OBJECTIVE 3

#### - Differences in Echo Detection Patterns Among Different Wavelength Radars

This section describes the observed differences in level of cloud top detection among the three radar sets. Radar observations are compared with visual aircraft observation for four instances when COSE project aircraft were in the vicinity of the radars. Cloud top observations are then presented for the storm of 12/10 - 12/11, 1979 during periods when all three radars were co-located and the X-band radar set was operating in a non-Doppler mode. Some results from an assessment of the validity of the Rayleigh approximation for one case are presented.

##### 1. Aircraft Visual Comparisons

The comparisons between radar detected cloud boundaries and aircraft observed visual cloud boundaries are presented in Table 3. The aircraft observations were made by the pilots of the National Center for Atmospheric Research's Queen Air (in March) and Colorado International Corporation's Cloud Physics instrumented Lear Jet (in December). The first comparison displayed (3/01/79, 1531) indicates that the Ku radar detected cloud base was about 130 m below the visually estimated cloud base. The second comparison taken about 41 hours later indicates a

discrepancy in cloud top observation of about 70 m, with the Ku-radar set detecting higher cloud top than estimated visually. However, the third comparison taken only 0134 after the second, indicates that the visual estimate is higher than the Ku detected cloud top height by about 170 m. The last comparison presented shows that the K-band detected cloud top height was about 250 m below visually estimated cloud top height, and the X-band detected cloud top height about 100 m below that of the K-band set.

Table 4.

Cloud top height visual from aircraft compared to radar (all in m AGL)

Date/Time of Observation	NCAR Queen-Air Visual	CIC-Lear Jet Visual	Ku Radar	K Radar	X Radar
3/01/79* 1531	1730		1600		
3/03/79 0825	1939		2000		
3/03/79 0959	1670		1500		
12/11/79 0754		1900		1650	1550

\*The observations from 3/01/79 pertain to cloud base rather than cloud top.

From this limited set of comparisons, no clear trend is evident in the comparison of radar detected and visually estimated cloud boundary elevations. It can be observed, however, that K and Ku cloud top observation agree with the visually estimated cloud top to within 300 m. Note that all of these observations were taken below 2 km AGL.



## 2. Co-located Radar Cloud Top Observations

Observations of cloud top height on 10-11 December by all 3 radar sets taken in intervals of 12 minutes during the times when the X-band radar was operating in non-Doppler mode are presented in Fig. 37. Generally, shorter wave-length radar indicated higher cloud tops as expected. For the observations displayed, Ku-band radar cloud top heights were observed to be an average of 186 m below K-band cloud top heights. X-band detected cloud top heights, in turn, were an average of 197 m below cloud top heights detected by the Ku-band for the 28 cases displayed.

The discrepancies among cloud top heights on an individual basis were far from consistent; probably a reflection of high variability of gradients of reflectivity near cloud top height. The maximum discrepancy between K and Ku-band detected cloud top heights occurs at 2125, when K-band cloud top height is more than 1 km above Ku-band detected cloud top height. As can be seen in Fig. 18, this time corresponds to a short-lived minimum in Ku-detected cloud top heights. This change is represented as only a reduction in reflectivity values in the K-band record, although X-band detected cloud top heights remain below Ku cloud top heights during this time. The maximum discrepancy between Ku and X-band detected cloud top heights was 600 m, occurring at 1925 and again at 2025. At 1825 and 1849 the X-band radar did not detect the first advected cloud deck at 5 km, which was detected by both the K and Ku-band sets. The maximum discrepancy in the entire data set between the X and K-band radar sets occurred around 0455 on 22 December when K-band detected cloud top height was approximately 3 km above X-band cloud top height.

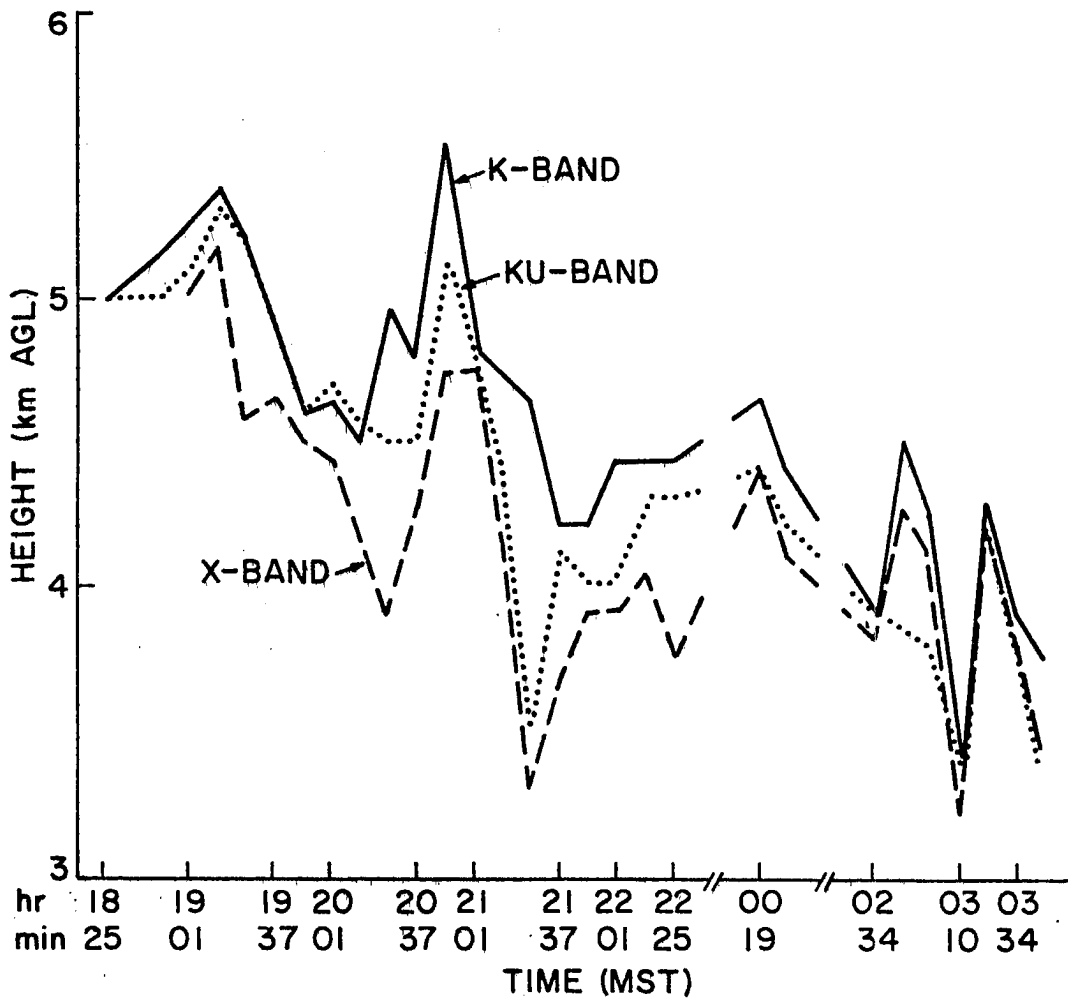


Figure 37. Cloud top heights as determined by K, Ku, and X-band co-located radars recorded at 12-minute intervals during 3 periods in the storm of 10 - 11 December, 1979.

### 3. Validity of the Rayleigh Approximation

The value Eta ( $\eta$ ) is the raw reflectivity making no assumptions about the scattering behaviour of the particles in the beam. If the Rayleigh approximation is valid for particles in the volume considered then the following equation holds

$$Z_E = \frac{\lambda^4 \eta}{\pi^5 |K|^2}$$

where  $Z_E$  is the effective radar reflectivity factor,  $\lambda$  is the wave length of the radar, and

$$K = \frac{M^2 + 1}{M^2 + 2}$$

where  $M$  is the complex index of refraction of the scattering substance.

The Rayleigh approximation is considered valid for ice particles less than 0.16 times the wavelength of the incident radion. Effective radar reflectivity factor values should be approximately equal for two radars of different frequency sampling a common volume when the Rayleigh approximation is valid for both radars and significant intervening attenuation does not exist for either radar. Under these conditions, the ratio of the reflectivity values should be equal to the inverse ratio of the fourth powers of their respective wavelengths; that is, for radars "a" and "b" of different frequencies:

$$\frac{\eta_a}{\eta_b} = \frac{\lambda_b^4}{\lambda_a^4}$$

In the case of the K and the X band radars, the Eta ratio should be a constant value of 256, or in terms of the display coding the alphabetic value "O" or "P". Because of uncertainties in signal processing and receiver drift, alphabetical values from "K" through "S" were

considered to represent regions where the Rayleigh approximation was essentially valid.

Figure 38 shows an example of this kind of analysis near the onset of the storm of 12/10/79. The period displayed (1905-1910) indicates high clouds existing before frontal passage (see Fig. 19A for the Ku-band record at this time and storm context). The data displayed represents alphabetic coding of Eta values for vertical profiles taken every 10 seconds, with dots indicating levels at which return power failed to exceed the threshold. The final row at the bottom is an average of the ratio of Eta values over the time in which they were detected during the 5-minute observation period.

Above 3 km, the K-band radar detects a deeper cloud deck than does the X-band radar, with generally higher tops and lower bases, as would be expected from the wavelength differences. Also the Eta values are relatively higher for the K-band set, which again is consistent with the difference in wavelength. The average ratios of Eta values detected run from "M" to "S", which would indicate that the Rayleigh approximation generally held true in this region. The gradual reduction in the average value of Eta ratio with height may be a result of some attenuation of the K-band beam.

Below 1.8 km, however, a different pattern is observed. The X-band set seems to detect continuous light return at levels which are below threshold for the K and vice-versa. For common levels of detection, the average Eta ratios are in the range "F" - "J" which would indicate non-Rayleigh scattering, at least for the K-band set. The data pattern is most probably the result of side lobe energy reflecting against the fairly rugged terrain in the vicinity of the radars.

MKG In AM	0.0	1.2	1.8	2.4	3.0	3.6	4.2	4.8	5.4	6.0
190419 y	.....	.....	.....	.....	.....	.....	.....	.....	.....	.....
190429 y	.....	.....	.....	.....	.....	.....	.....	.....	.....	.....
190439 y	.....	.....	.....	.....	.....	.....	.....	.....	.....	.....
190449 y	.....	.....	.....	.....	.....	.....	.....	.....	.....	.....
190459 y	.....	.....	.....	.....	.....	.....	.....	.....	.....	.....
190500 n	.....	.....	.....	.....	.....	.....	.....	.....	.....	.....
190510	.....	.....	.....	.....	.....	.....	.....	.....	.....	.....
190519	.....	.....	.....	.....	.....	.....	.....	.....	.....	.....
190529	.....	.....	.....	.....	.....	.....	.....	.....	.....	.....
190539	.....	.....	.....	.....	.....	.....	.....	.....	.....	.....
190549	.....	.....	.....	.....	.....	.....	.....	.....	.....	.....
190559	.....	.....	.....	.....	.....	.....	.....	.....	.....	.....
190609	.....	.....	.....	.....	.....	.....	.....	.....	.....	.....
190619	.....	.....	.....	.....	.....	.....	.....	.....	.....	.....
190629	.....	.....	.....	.....	.....	.....	.....	.....	.....	.....
190639	.....	.....	.....	.....	.....	.....	.....	.....	.....	.....
190649	.....	.....	.....	.....	.....	.....	.....	.....	.....	.....
190659	.....	.....	.....	.....	.....	.....	.....	.....	.....	.....
190709	.....	.....	.....	.....	.....	.....	.....	.....	.....	.....
190719	.....	.....	.....	.....	.....	.....	.....	.....	.....	.....
190729	.....	.....	.....	.....	.....	.....	.....	.....	.....	.....
190739	.....	.....	.....	.....	.....	.....	.....	.....	.....	.....
190749	.....	.....	.....	.....	.....	.....	.....	.....	.....	.....
190759	.....	.....	.....	.....	.....	.....	.....	.....	.....	.....
190809	.....	.....	.....	.....	.....	.....	.....	.....	.....	.....
190819	.....	.....	.....	.....	.....	.....	.....	.....	.....	.....
190829	.....	.....	.....	.....	.....	.....	.....	.....	.....	.....
190839	.....	.....	.....	.....	.....	.....	.....	.....	.....	.....
190849	.....	.....	.....	.....	.....	.....	.....	.....	.....	.....
190859	.....	.....	.....	.....	.....	.....	.....	.....	.....	.....
190909	.....	.....	.....	.....	.....	.....	.....	.....	.....	.....
190919	.....	.....	.....	.....	.....	.....	.....	.....	.....	.....
190929	.....	.....	.....	.....	.....	.....	.....	.....	.....	.....
190939	.....	.....	.....	.....	.....	.....	.....	.....	.....	.....
190949	.....	.....	.....	.....	.....	.....	.....	.....	.....	.....
190959	.....	.....	.....	.....	.....	.....	.....	.....	.....	.....

Figure 38. K-band assessed Eta values, X-band assessed Eta values, and the ratio of K/X Eta assessment for 12/10/79 190519 - 190959 MST.

Reflections from side lobes may pose less of a problem for the K-band set because cuffs were installed around both the transmitting and receiving dishes. The single X-band dish did not have such a cuff but the Ku-set was installed with one.

## IV. CONCLUSIONS

### A. Major Conclusions

1. The highest cloud tops and coldest cloud top temperatures for individual storms occurred near the beginning of the radar observation periods. Cloud tops consistently lowered during the storm sequence, usually attaining minimum heights and maximum temperatures just before the radar detection region cleared.
2. Semi-periodic pulses of reflectivity and cloud top height changes in the patterns of the storms are consistent with previously observed convective bands (Furman, 1967). As in the previous study, the pulses were on the order of 2 hours in frequency. Equivalent Potential Temperature analyses, however, did not indicate the existence of deep or strong convective instability for the storms examined (23-24 February in Lee (1980), and 1 March in this study). Moving gravity waves may be an alternative explanation for this phenomenon.
3. Two cases (2-3 March; 11 December) were observed when low clouds with relatively warm cloud top temperatures ( $> -25^{\circ}\text{C}$ ) in the later stages of the storm sequence persisted more than 8 hours. In the case of the storm on 2-3 March the low cloud persisted more

than 24 hours and produced significant precipitation at the radar site.

4. Zones of reflectivity  $>20$  dBz did not correspond well with any particular temperature level. Such zones did seem to be associated with the periodic changes in cloud top height.
5. Downward velocities were observed using Doppler radar which could not be explained in terms of crystal fall velocities and were probably the result of downward air motions. The inferred downward air motions were on the same order of magnitude as the predicted crystal fall velocities.
6. Horizontal wind vectors assessed using a VAD technique generally agreed well with horizontal wind vectors derived from rawinsonde. Below ridge top, horizontal speeds above the radar site were about 5 m/s slower than horizontal wind speeds detected above the rawinsonde launch site. This suggested the presence of barrier blocking or the presence of an inversion decoupling low-level flow from flow aloft.
7. For a period when all three radars operated at the same location, the Ku-band radar underestimated cloud top heights as assessed by the K-band radar by an average of about 200 m. The X-band radar underestimated Ku-band radar assessed cloud tops heights also by an average of about 200 m.



## B. Additional Observations

1. The changes in cloud top during the storms generally were consistent with the thermodynamic "storm stages" described by Cooper and Marwitz (1980), for storms in the San Juans. Their study did not, however, note existence of convective bands (they do indicate the presence of smaller scale waves) or persistence of low cloud during the "dissipation stage.
2. Vertical profiles of downward velocity did not correspond well to reflectivity profiles or model predicted crystal fall velocity profiles. A model of the crystal downward velocities which neglected components of air motion led to serious errors in this case, when compared to radar observed downward components of crystal trajectory.
3. The highest relative reflectivities as detected by the Ku-set for individual profiles were never in the lowest detectable range bin or at cloud base. Precipitation records did not indicate a consistent gradient in elevation of precipitation rate. Later tests revealed a decrease in sensitivity in the lower range bins which was probably the result of T-R tube recovery. The effect exponentially decreased with height and amounted to a loss of 12 dB in the lowest displayed range bin in the worst case. A similar trend was present in the X-band reflectivity profiles.

4. When the Ku-band radar was moved west about 15 km no high reflectivity zones were observed ( $> 10$  dBz) although the clouds were very deep (above 6 km). If not indicative of decreased radar sensitivity, this observation would be consistent with the results of Furman (1967) who concluded that highest reflectivities occurred near ridge tops in the Climax experimental area.
5. In a VAD profile taken 0630 MST on 11 December, evidence exists for light downvalley flow at low levels. The easterly component diminishes with height.
6. Comparison of four aircraft pilot observations with radar assessed cloud boundaries reveals no consistent trend. K and Ku heights were within 300 m of pilot reported height in these cases.
7. Ratios of Eta values as detected by the X and K-band sets indicate no serious departure from the Rayleigh approximation existed in cloud regions, when both sets were operating properly. Light return from what is thought to be side lobe energy reflecting on ground features exhibited non-Rayleigh characteristics at lower levels.

#### C. Suggestions for Future Research

This study primarily examined mesoscale features and motions in orographic clouds. Among the points which deserve further attention are the following:

- 1) Periodic bands - A more exhaustive data set might reveal under what synoptic conditions these periodic fluctuations are likely to occur. Aircraft data may reveal more of their microphysical structure. Satellite confirmation would also be of value.
- 2) Low persistent Clouds - Again, a more substantial data set may indicate under what conditions this regime sets up. Detailed exploration of these clouds by aircraft would be difficult due to the low altitudes of interest.
- 3) Air motions - Scanning Doppler radar observations may reveal the pattern of atmospheric motions and their relationship to topography.

Another general approach would be to attempt to use the radars to explore the orographic clouds on a microphysical level. In order to achieve this, the radar data would have to be "microphysically calibrated", or compared with aircraft cloud particle data. While it is true that reflectivity is a function of crystal diameter, crystal density and habit, and crystal concentration; limits or possible ranges could be set on two of these parameters in order to derive the third parameter. For example, assuming plate-like crystals of a certain density, and assuming the maximum number of crystals observed by aircraft under conditions where ice multiplication is unlikely, one could use the reflectivity value to make a statement about the minimum possible average crystal diameter within the volume sampled. While these kinds of conclusions are clearly inferior to actual crystal and droplet spectra obtained by aircraft, the radars could sample continuously throughout the storm and instantaneously throughout the depth of the cloud.

From a weather modification point of view establishing radar-precipitation covariates would be extremely useful. Among the possible

correlation variables would be cloud top height, maximum detected reflectivity in the vertical, or Z value in the lowest detectable range bin.

## REFERENCES

- Battan, L. J., 1973: Radar Observation of the Atmosphere. University of Chicago Press, Chicago, Illinois, 324 pp.
- Bergeron, T., 1933: On the physics of clouds and precipitation. Proc. 5th Assembly U. G. G. I., Lisbon, p. 156-178.
- Bergeron, T., 1949: The problem of an artificial control of rainfall on the globe; I. General effects of ice-nuclei in clouds. Tellus, 1, p. 32-50.
- Byers, H. R., 1965: Elements of Cloud Physics, University of Chicago Press, Chicago, Illinois, 191 pp.
- Chappell, C. F., 1970: Modification of cold orographic clouds. Ph. D. Thesis, Department of Atmospheric Science, Colorado State University, Fort Collins, Colorado 196 pp.
- Cooper, W. A., and J. D. Marwitz, 1980: Winter storms over the San Juan Mountains. Part III: Seeding potential. J. Appl. Meteor., 19, p. 942-949.
- Cooper, W. A., and C. P. R. Saunders, 1980: Winter storms over the San Juan Mountains. Part II: Micro-physical processes. J. Appl. Meteor., p. 927-941.
- Cotton, W. R., 1972: Numerical simulation of precipitation development in supercooled cumuli. Part II, Monthly Weather Review, 100, p. 764-784.
- Davis, C. I., and A. H. Auer, 1974: Use of isolated orographic clouds to establish the accuracy of idiffusional ice crystal growth equations, Preprints from the Conference on Cloud Physics, Oct. 21-24, 1974 Tucson, Arizona, p. 141-147.
- Douglas, R. H., K. L. S. Gunn, and J. S. Marshall, 1957: Pattern in the vertical of snow generation, J. Met., 14, p. 95-114.
- Elliott, R. D. and E. L. Hovind, 1964: On convection bands within Pacific Coast storms and their relationship to storm structure. J. Appl. Meteor., 3, p. 143-154.
- Elliott, R. D., R. W. Shaffer, A. Court, and J. F. Hannaford, 1978: Randomized cloud seeding in the San Juan Mountains, Colorado, J. Appl. Meteor., 17, p. 1298-1318.

- Furman, R. W., 1967: Radar characteristics of wintertime storms in the Colorado Rockies, Master's Thesis, Department of Atmospheric Science, Colorado State University, Fort Collins, Colorado. 53 pp.
- Grant, L. O., J. D. Marwitz, and C. W. Thompson, 1965: Application of radar to snow surveying. Proceedings of the 33rd Annual Meeting of the Western Snow Conference, April 20-22, 1965, Colorado Springs, Colorado. p. 42-48.
- Grant, L. O. and P. W. Mielke, Jr., 1967: A randomized cloud seeding experiment at Climax, Colorado, 1960-1965, Proceedings of the Fifth Berkeley Symposium in Mathematical Statistics and Probability, Vol. 5, University of California.
- Gunn, K. L. S., M. P. Langleben, A. S. Dennis and B. A. Power, 1954: Radar evidence of a generating level for snow. J. Meteor., 11, p. 20-26.
- Hallett, J., and B. J. Mason, 1958: The influence of temperature and supersaturation on the habit of snow crystals from the vapor, Proceedings of the Royal Society of London, Ser. A. 247, Oct. 1958, p. 440-453.
- Hartzell, C. L. and L. W. Crow, 1976: Western Scientific Services, Inc., Final Report for the Colorado River Basin Pilot Project, Report Fr-359-46, United States Department of the Interior, Bureau of Reclamation, Division of Atmospheric Water Resources Management, Contract No. 14-06-D-6644, 39 pp.
- Hobbs, P. V., L. F. Radke, R. R. Weiss, D. G. Atkinson, J. D. Locatelli, K. R. Biswas, F. M. Turner, and C. E. Robertson, 1974: 'Use of a vertically-pointing Doppler radar in the Cascade Project' in Research Report VIII: The structure of clouds and precipitation over the Cascade Mountains and their modification by artificial seeding, Contributions from the Cloud Physics Group, Department of Atmospheric Sciences, University of Washington, Seattle, Washington, p. 85-104.
- Kobayashi, T., 1957: Experimental Researches on the snow crystal habit and growth by means of a diffusion cloud chamber, J. Meteor., Soc. of Japan, 75th Anniversary Volume, p. 38-47.
- Kobayashi, T., 1960: Experimental researches on the snow crystal habit and growth using a convection-mixing chamber, J. Meteor., Soc. of Japan, Ser. 2, Vol. 38, p. 231-238.
- Langleben, M. P., 1956: The plan pattern of snow echoes at the generating level. J. Meteor., 13, p. 554-560.
- Lee, R.R., 1980: Wintertime Cloud Systems over the Colorado Rockies: Three Case Studies. Atmospheric Science Paper #331, Department of Atmospheric Science, Colorado State University, Ft. Collins, CO.

- Ludlam, F. H., 1955: Artificial snowfall from mountain clouds, Tellus, 7, 277-290.
- Marshall, J. S., 1953: Precipitation Trajectories and Patterns. J. Meteor., 10, p. 25-29.
- Moninger, W. R., 1980: Doppler radar studies during the Sierra Cooperative Pilot Project, NOAA Technical Memorandum ERL WPL-50, NOAA Environmental Research Laboratories, Wave Propagation Laboratory, 107 pp.
- Vardiman, L., 1974: The generation of secondary ice particles in clouds by crystal-crystal collision, Ph. D. Thesis, Department of Atmospheric Science, Colorado State University, Fort Collins, Colorado, 117 pp.
- Walsh, P. A., 1977: Cloud droplet measurements in wintertime clouds, Master's Thesis, Department of Atmospheric Science, University of Wyoming, Laramie, Wyoming, 170 pp.
- Weiss, R. R., J. D. Locatelli, and P. V. Hobbs, 1979: Simultaneous observations of cloud and precipitation particles with vertically-pointing X-band and K-band radars, IEEE Transactions on Geoscience Electronics, GE-17, p. 151-153.
- Yaw, R. H., 1974: A radar examination of the small scale structure of winter orographic precipitation, Preprints from the 15th Radar Meteorology Conf., 10-12 Oct. 1972, Champaign-Urbana, Illinois, p. 124-131.

## Appendix I

### Derivation of the Radar Equation (Following Battan, 1973)

#### A. General Case

For an electro-magnetic energy source radiating isotropically, the amount of power at a point at a distance "r" away from the source is

$$P_P = \frac{P_T}{4\pi r^2} \quad (1)$$

where  $P_P$  is the amount of power at the point, and  $P_T$  is the power originally transmitted.

Radars utilize feed horns and reflective dishes to focus the transmitted energy into a conical "beam". The "Gain" is a measure of this beam focusing, and is defined as the ratio of the power per unit area along the axis of the beam to the isotropic value:

$$P_B = P_P G = \frac{P_T G}{4\pi r^2} \quad (2)$$

where  $G$  is the Antenna gain, and  $P_B$  is the power at a point in the axis of the beam a distance "r" away from the antenna.

The amount of power intercepted by a target of cross-sectional  $A_X$  in the radar beam ( $P_\sigma$ ) is

$$P_\sigma = P_B A_X = \frac{P_T G A_X}{4\pi r^2} \quad (3)$$



If no power is absorbed but all power is scattered isotropically (in fact this is never the case but this is corrected for later in the derivation through knowledge of the target's complex index of refraction and back-scattering behaviour) then the power intercepted by the radar system will be

$$P_R = \frac{P_\sigma}{4\pi r^2} A_E \quad (4)$$

where  $A_E$  is the effective cross-section of the antenna; theoretically

$$A_E = \frac{G \lambda^2}{4\pi}$$

where  $\lambda$  is the wavelength of the incident radiation. Substituting for  $P_\sigma$  (eqn. 3) and  $A_E$

$$P_R = \frac{P_\sigma}{4\pi r^2} A_E = \frac{P_T G^2 \lambda^2 A_X}{(4\pi)^3 r^4} \quad (5)$$

## B. Meteorological Targets

Meteorological targets would almost always be composed of a number of individual targets (crystals or droplets) within the sample volume, each with backscattering cross-section (the cross-section which the particle would have if no power was absorbed and all intercepted power was scattered isotropically) equal to  $\sigma_i$ :

$$P_R = \frac{P_T G^2 \lambda^2}{(4\pi)^3 r^4} \sum_{\text{sample volume}} \sigma_i \quad (6)$$

Equation 6 can also be expressed in terms of average backscattering cross-section per unit volume times the sample volume at an instant in time:

$$P_R = \frac{P_T G^2 \lambda^2}{(4\pi)^3 r^4} V_m \Sigma_{\text{unit volume}} \bar{\sigma} \quad (7)$$

where  $V_M$  is the measured volume at a distance "r" from the antenna.

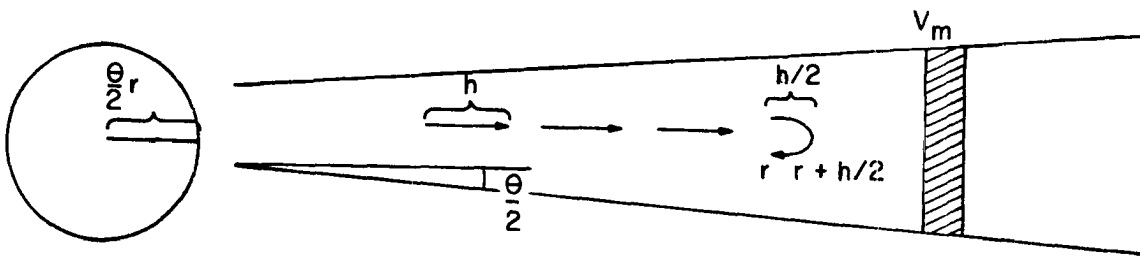


Fig. I-1 Cross-sectional and plan view of the dimensions of a radar sampling volume ( $V_M$ ).

As can be seen from the above figure depicting the cross-sections of a radar beam from 2 aspects,

$$V_M = \pi \left( r \frac{\theta}{2} \right)^2 \frac{h}{2} \quad (8)$$

where  $\theta$  is the beam width and  $h$  is the pulse length.

Substituting eqn. 8 into eqn. 7:

$$P_R = \frac{P_T G^2 \lambda^2 \theta^2 h}{512 \pi^2 r^2} \Sigma_{\text{unit volume}} \bar{\sigma} \quad (9)$$

Equation 9 was derived assuming constant power across the beamwidth.

A more exact form of the radar equation assuming a Gaussian distribution of power across the beamwidth and noting the difference between one and two-way power density patterns for an antenna is

$$P_R = \frac{P_T G^2 \lambda^2 \theta^2 h}{512 (2 \ln 2) \pi^2 r^2} \Sigma_{\text{unit volume}} \bar{\sigma} \quad (10)$$

Equation 10 relates the power returned to the average backscattering cross-section per unit volume. In order to relate power returned to actual average particle diameter, the complex index of refraction and backscattering behaviour of the target particles must be specified. Unfortunately the equations describing the backscattering behaviour of the scattering of a plane wave by a spherical particle (Mie equations) are rather complex and not a unique function of particle diameter except when the ratio of the particle diameter to the wavelength of the incident radiation is under a certain value. In this region ( $D < 0.16\lambda$  for ice) the higher order terms can be neglected so that

$$\sigma_i \approx \frac{\pi^5}{\lambda^4} |K|^2 D_i^6 \quad (11)$$

is a close approximation to reality where  $K = \frac{m^2 - 1}{m^2 + 2}$  and  $m$  is the complex index of refraction of the target substance, and  $D_i$  is the actual diameter of the particle. This approximation is known as the "Rayleigh approximation". For detection of ice particles  $|K|^2 = 0.197$  and  $D_i$  is the diameter of the equivalent water droplet if the ice particle were melted.

The value Eta ( $\eta$ ) is equivalent to the average backscattering cross-section per unit volume and is called the "reflectivity". From eqn.

$$\eta = \sum_{\text{unit volume}} \bar{\sigma}_i = \frac{\pi^5}{\lambda^4} |K|^2 \sum_{\text{unit volume}} D_i^6 = \frac{\pi^5}{\lambda^4} |K|^2 Z_e \quad (12)$$

where  $Z_e = \sum D_i^6$  is the effective radar reflectivity factor, assuming the the Rayleigh approximation is valid for the volume sampled.

Substituting equation 12 into equation 10,

$$P_R = \frac{\pi^3 P_T G^2 \theta^2 h}{\lambda^2 512 (21n2) r^2} |K|^2 Z_e \quad (13)$$

Note that in this final form of the radar equation, the power returned is proportional to  $\lambda^{-2}$  and  $r^{-2}$ . Thus, sensitivity decreases with wavelength and range.

**Appendix II**

**Synoptic Charts and Satellite  
Photographs for the Six Case  
Studies under Objective 1**

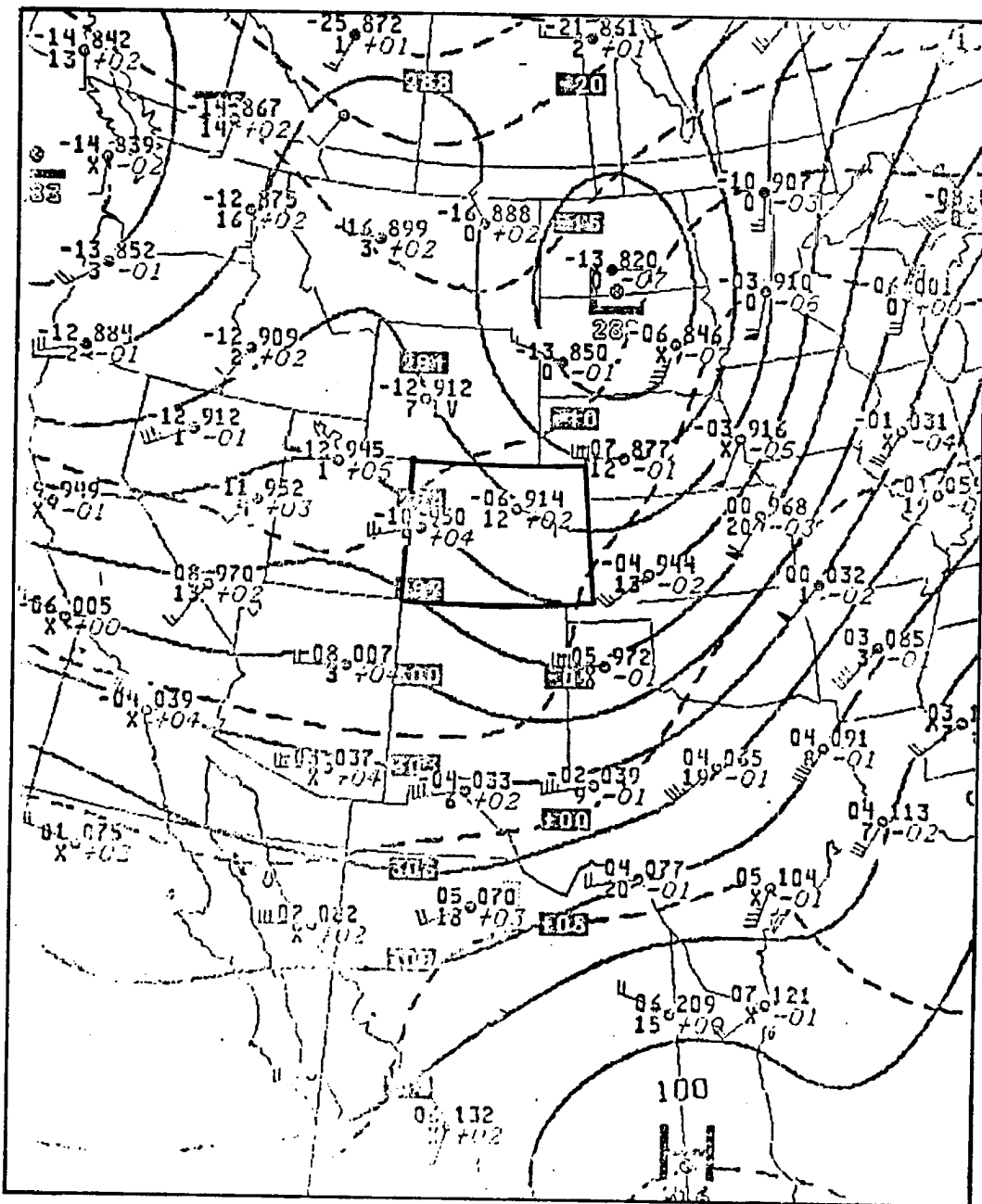


Fig. II-1 Case 1. 2/23/79 OZ (2/22/79 1700 MST) 70 KPa chart.

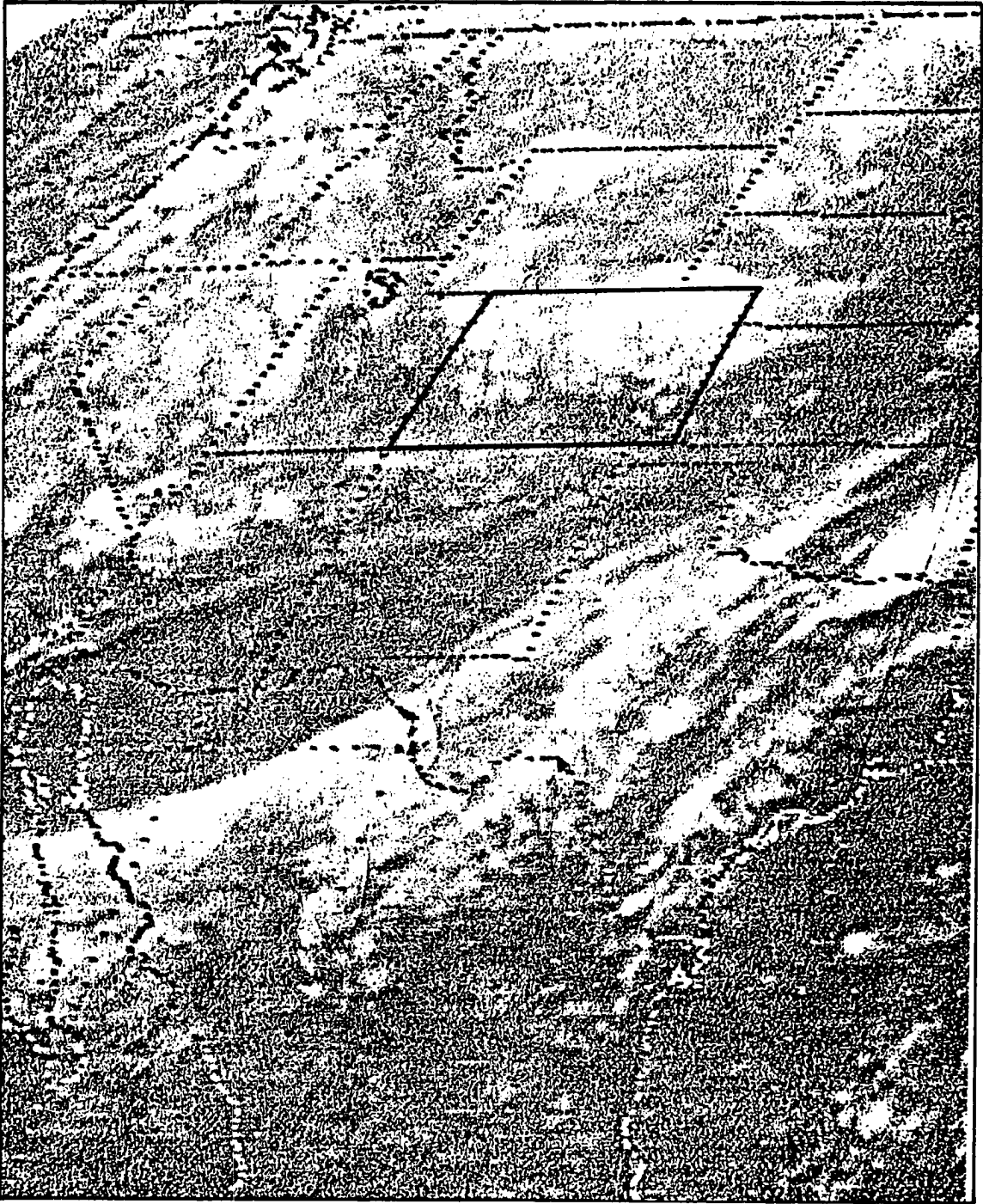


Fig. II-2 Case 1. 2/23/79 3Z (2/22/79 2000 MST) satellite photograph.

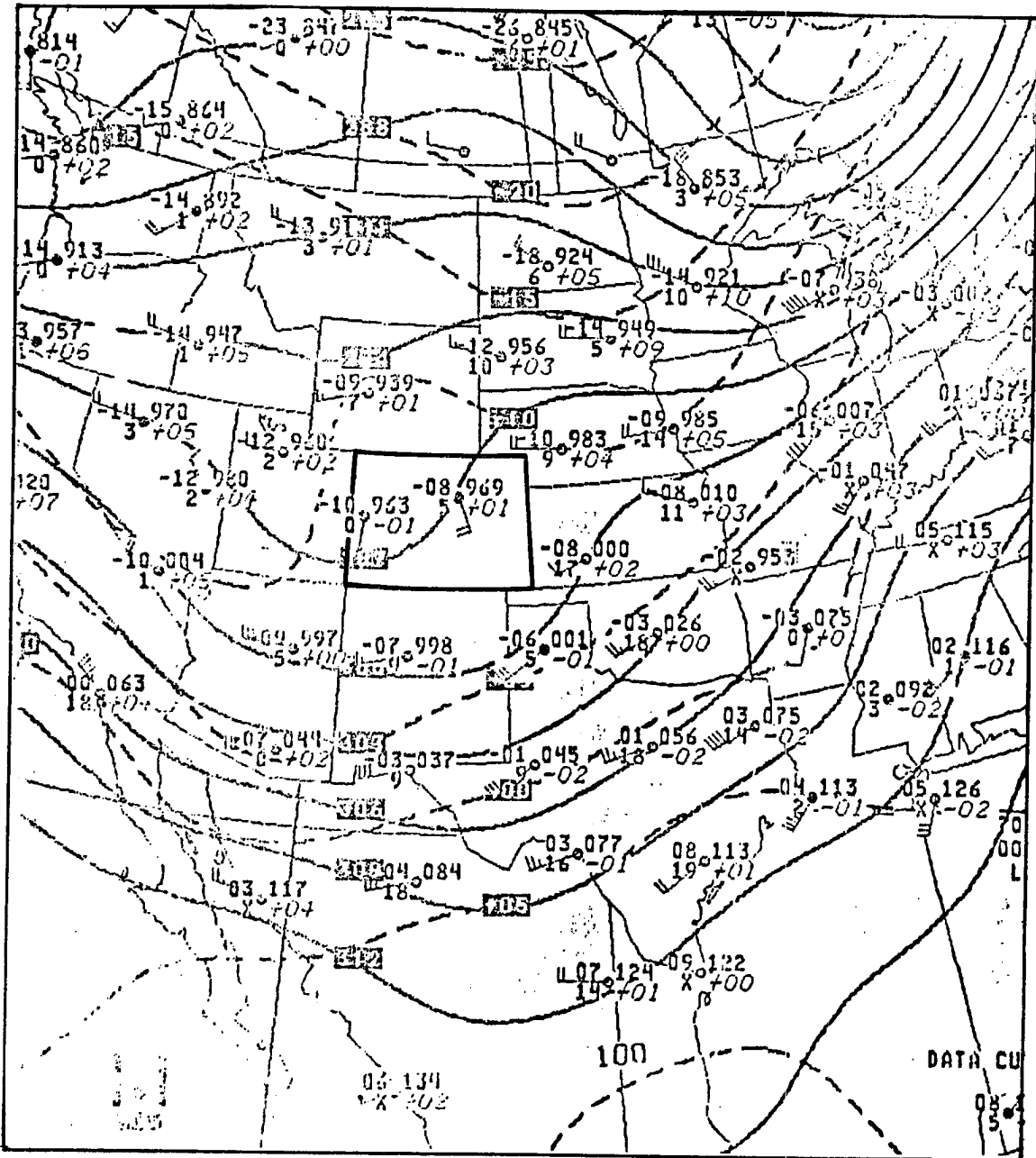


Fig. II-3 Case 2. 2/24/79 9Z (2/24/79 1700 MST) 70 KPa chart.



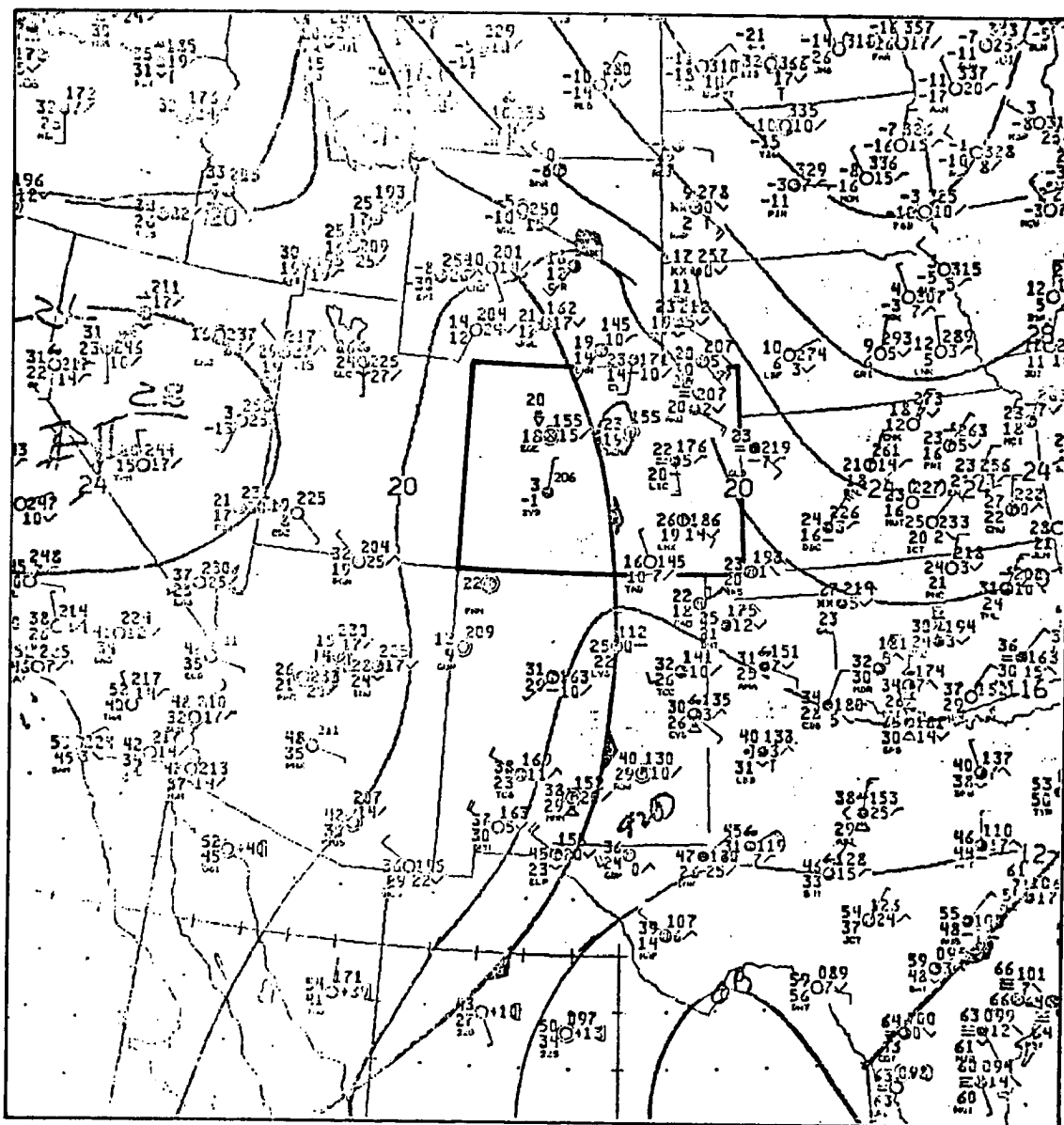


Fig. II-4 Case 2. 2/24/79 OZ (2/24/79 0200 MST) surface chart.

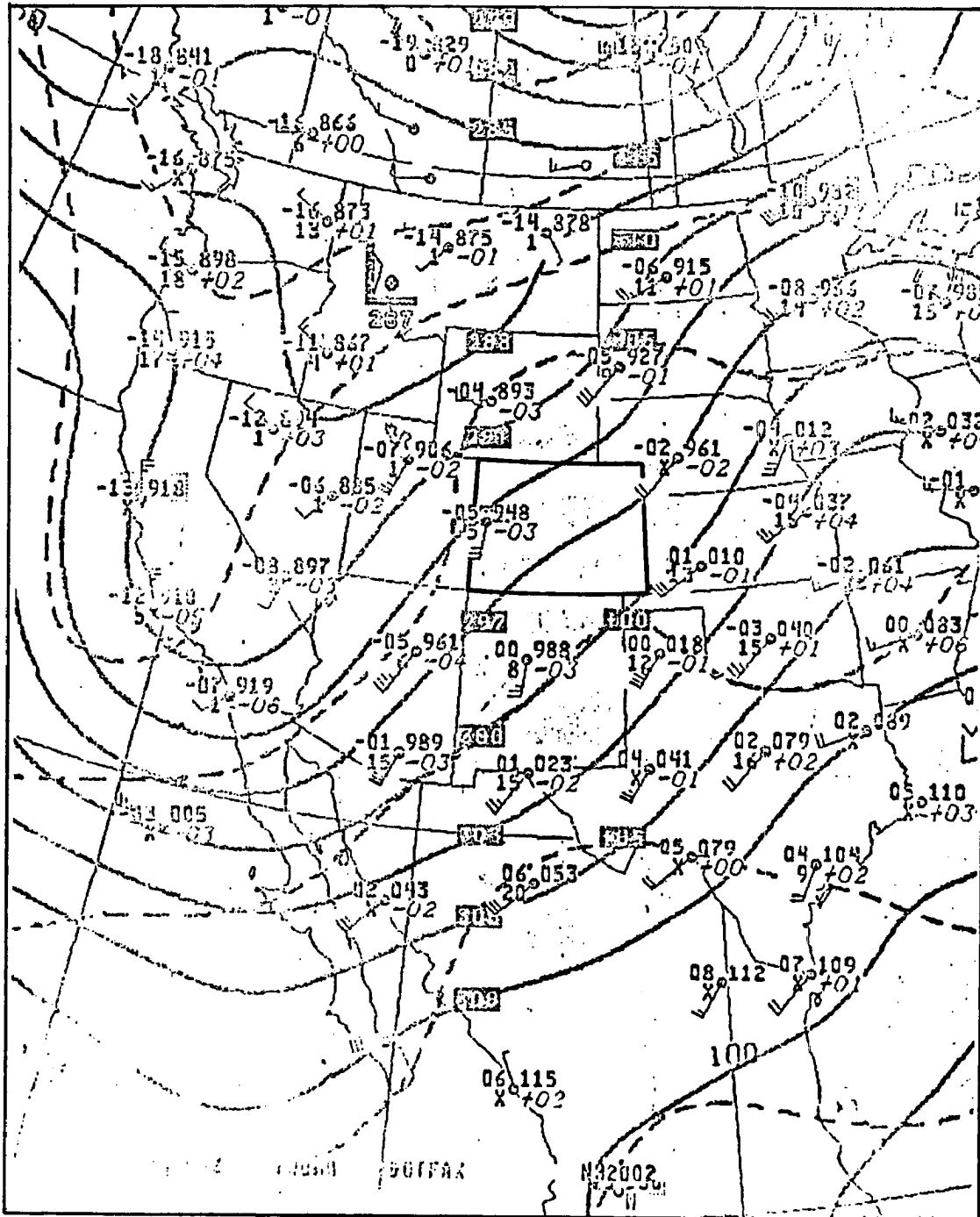


Fig. II-5 Case 3. 3/2/79 0Z (3/1/79 1700 MST) 70 KPa chart.

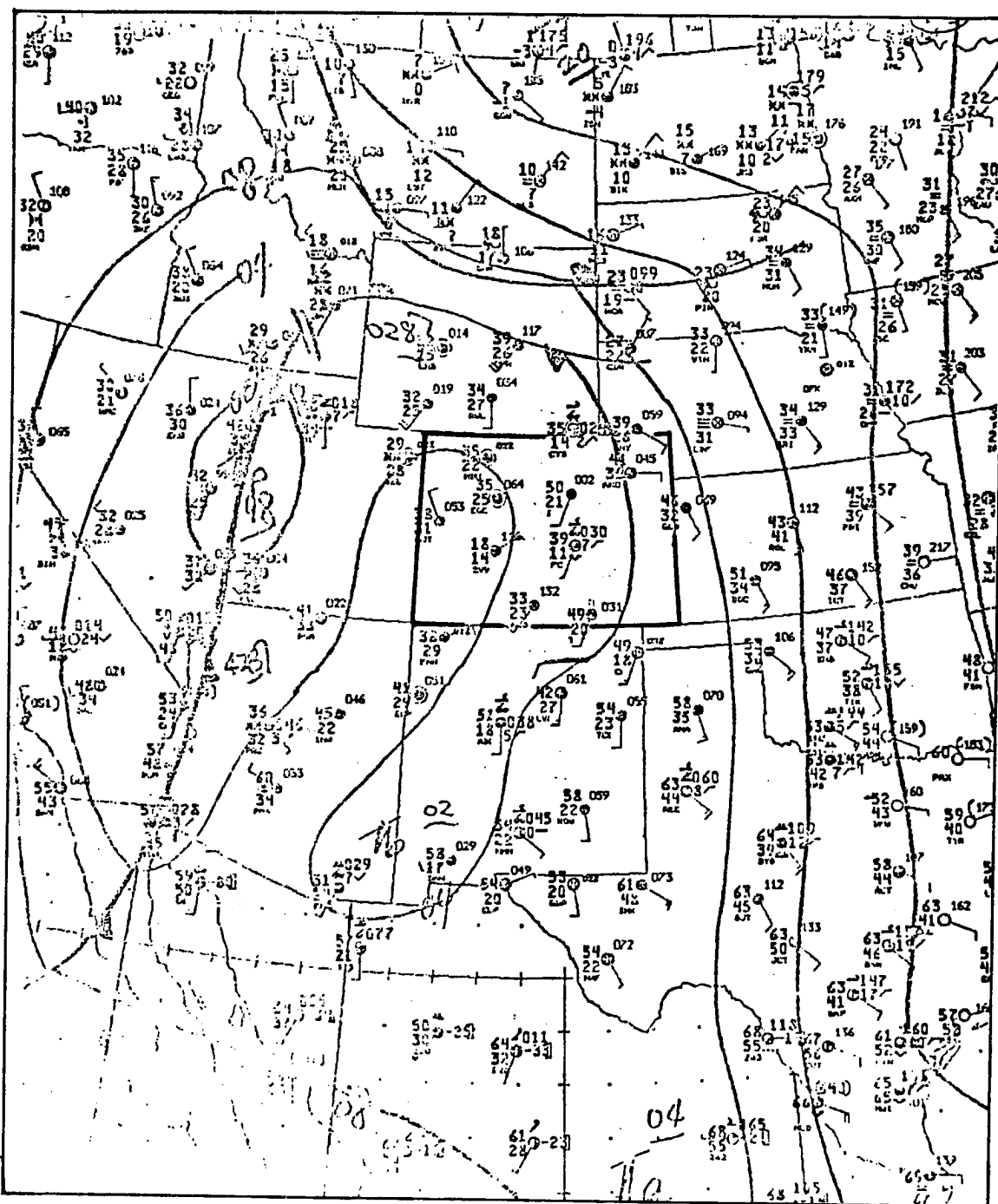


Fig. II-6 Case 3. 3/2/79 3Z (3/1/79 2000 MST) surface chart.

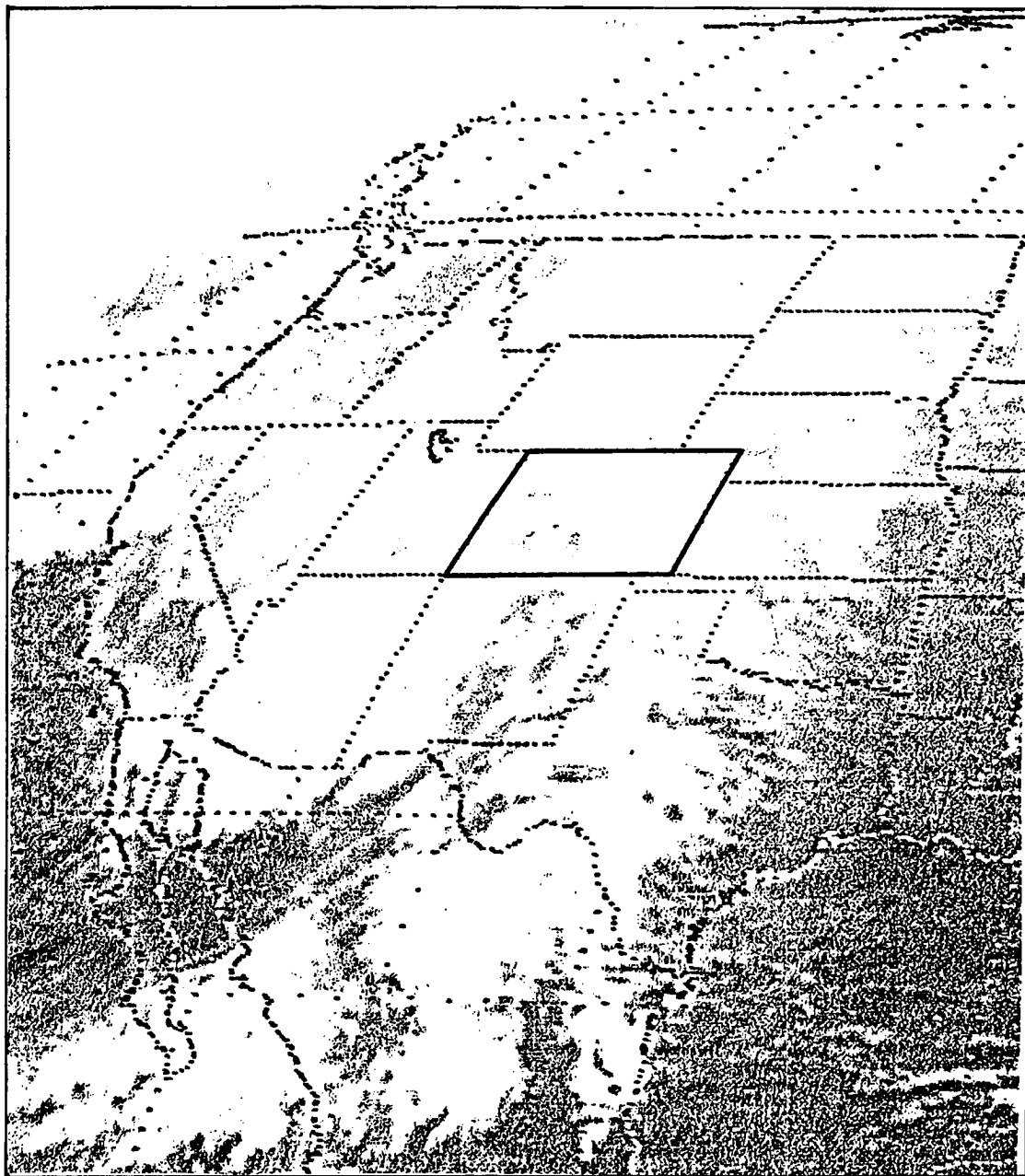


Fig. II-7 Case 3. 3/2/79 3Z (3/1/79 2000 MST) satellite photograph.

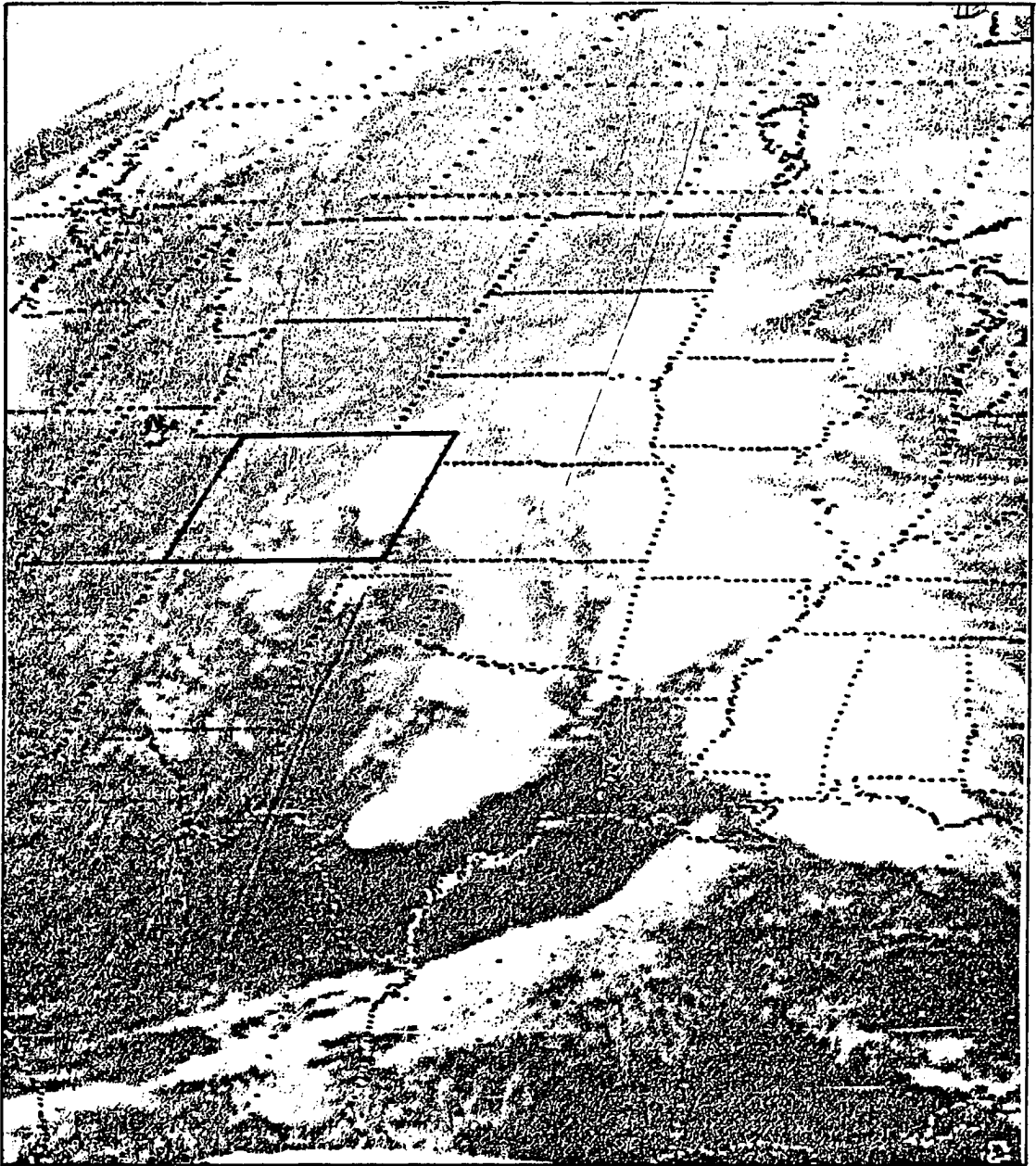


Fig. II-8 Case 4. 3/3/79 3Z (3/2/79 2000 MST) satellite photograph.

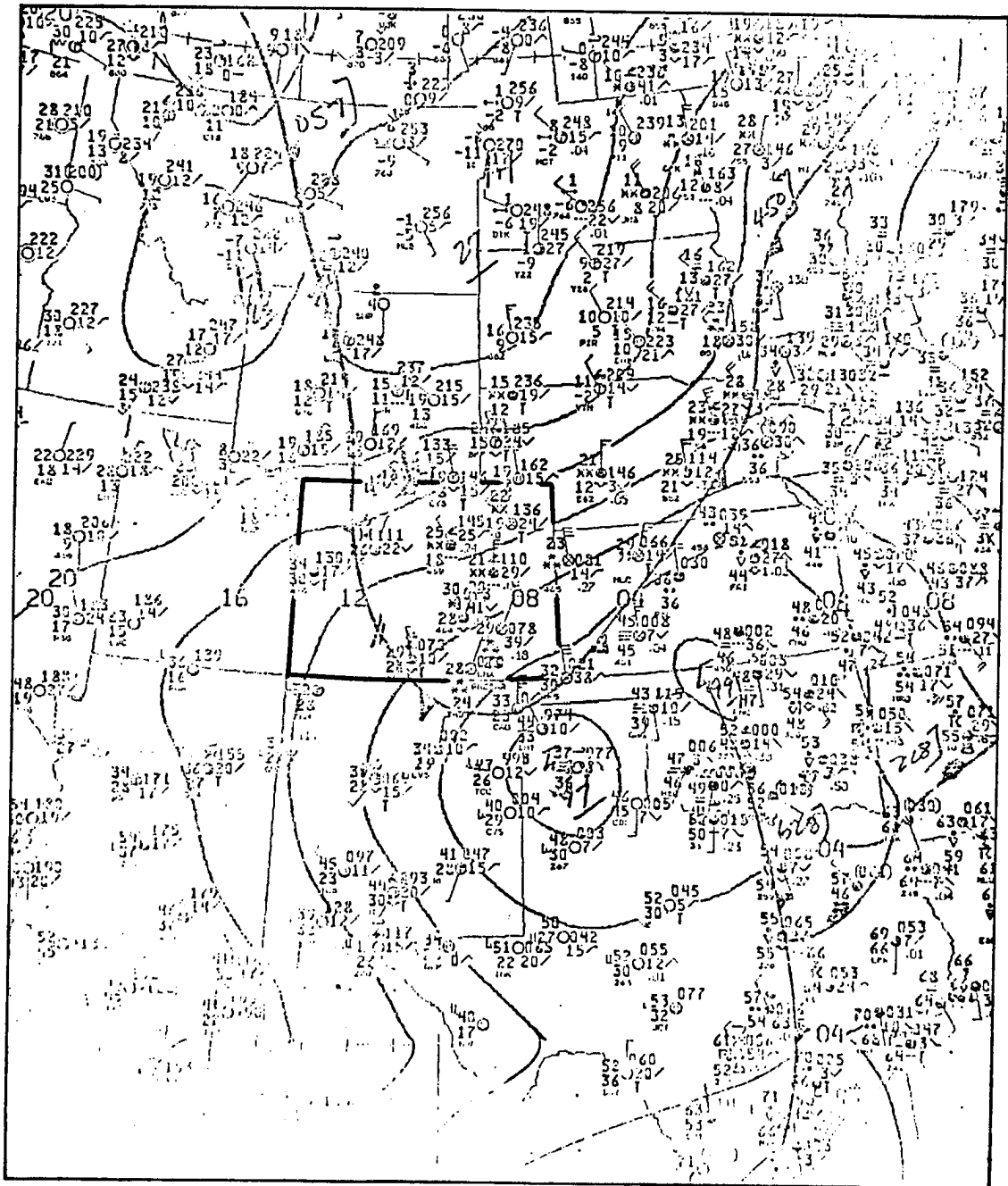


Fig. II-9 Case 4. 3/3/79 6Z (3/2/79 2300 MST) surface chart.

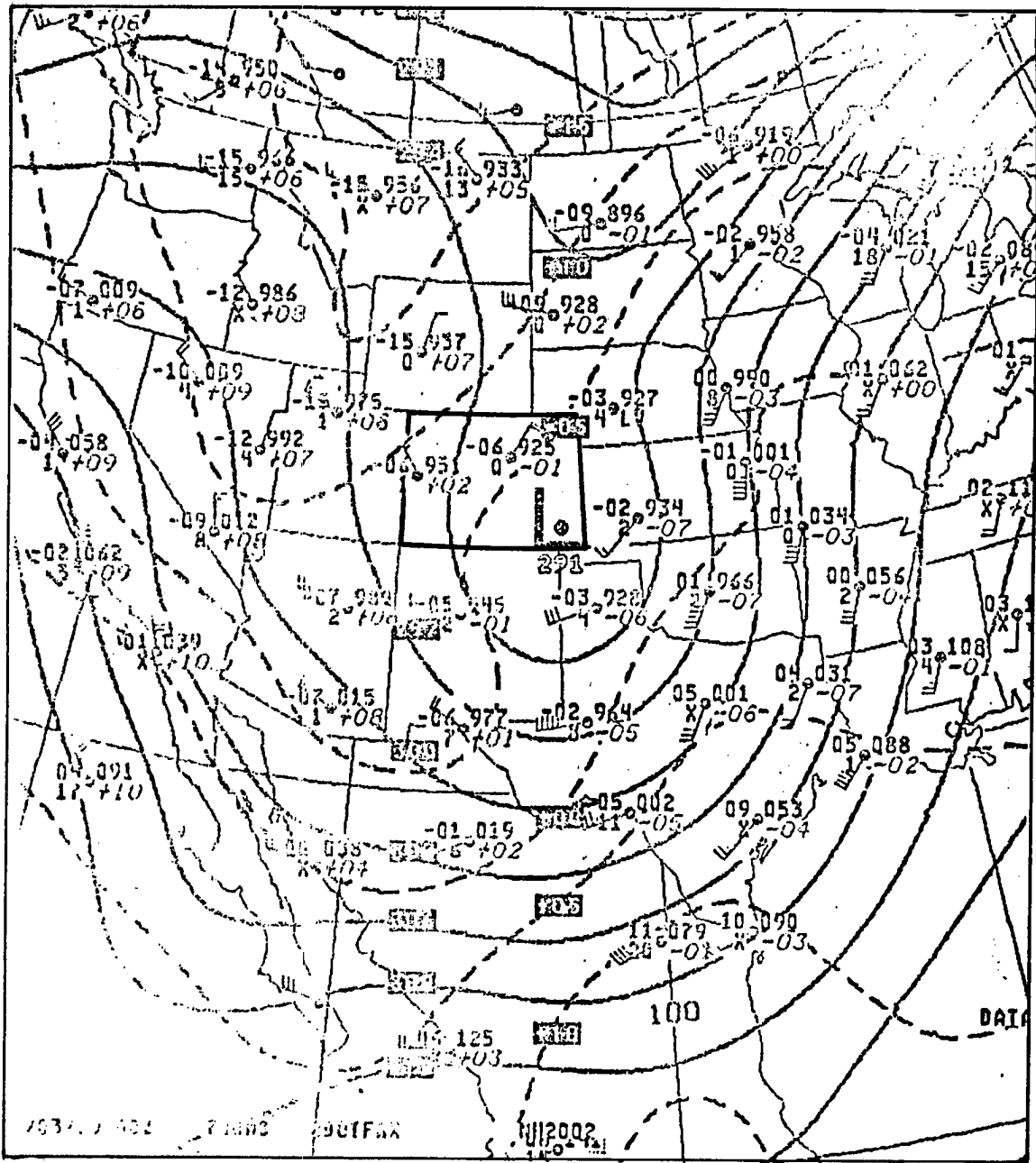


Fig. II-10 Case 4. 3/3/79 OZ (3/2/79 1700 MST) 70 KPa chart.

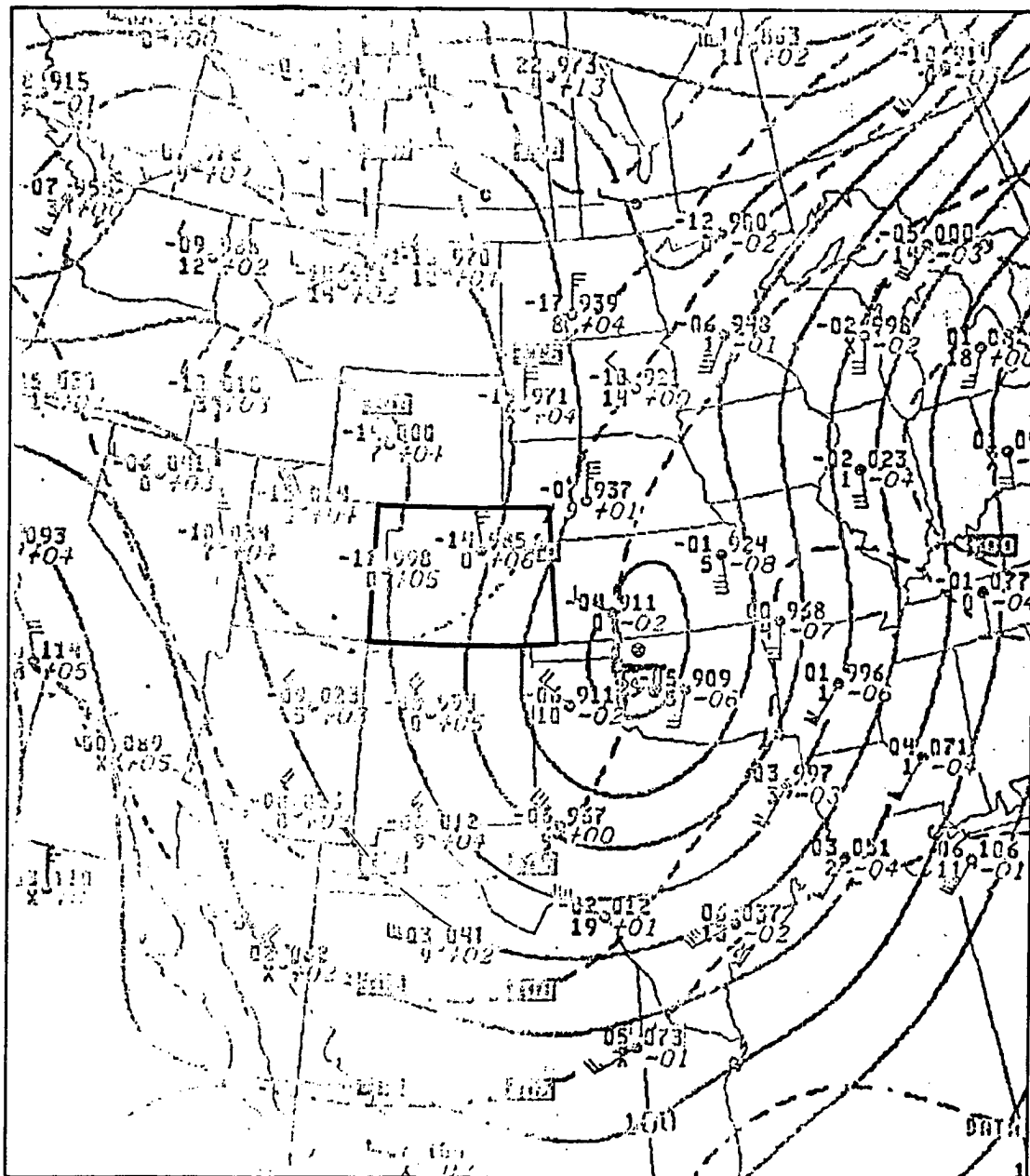


Fig. II-11 Case 4. 3/3/79 12Z (3/3/79 0500 MST) 70 KPa chart.



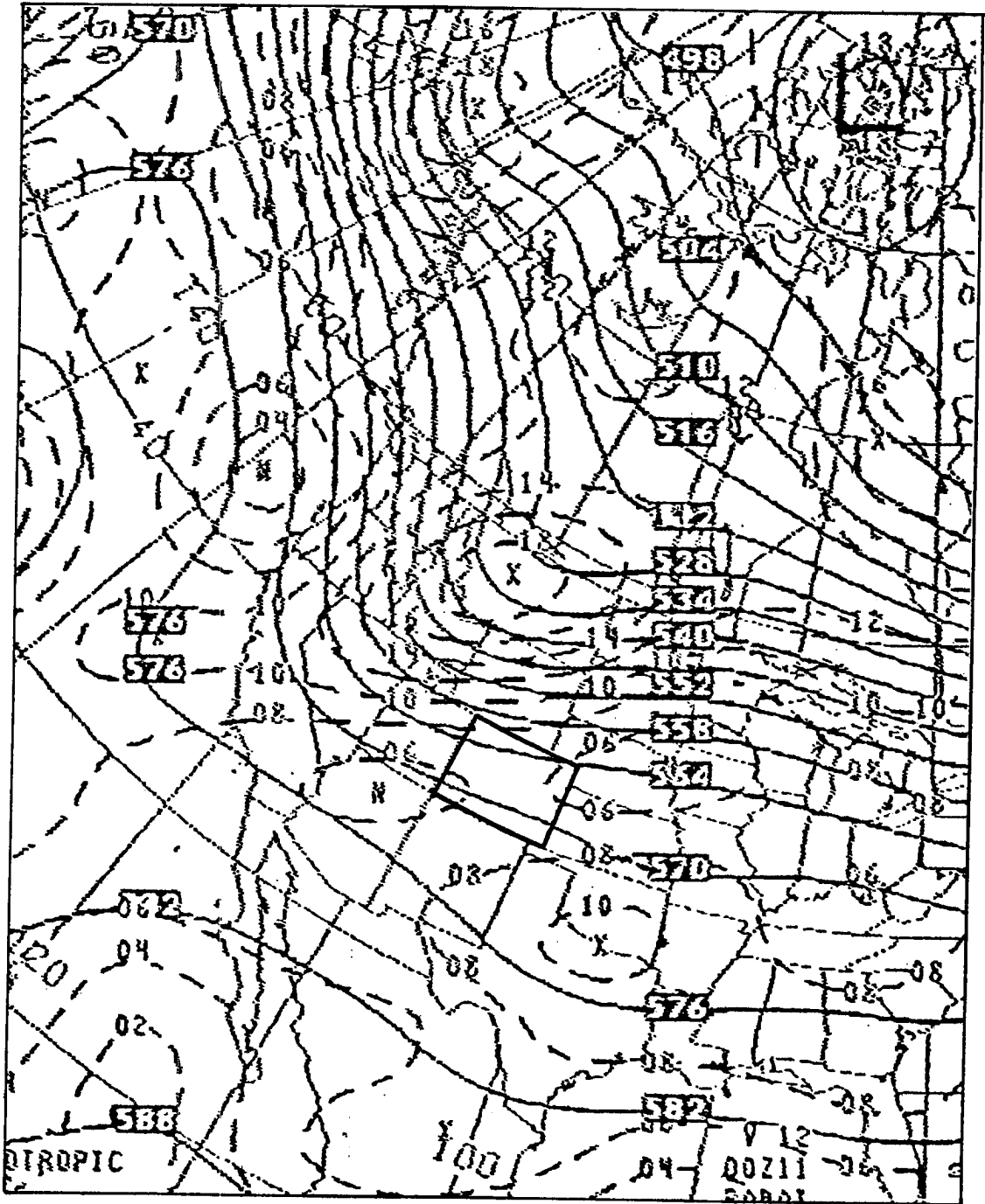


Fig. II-12 Case 5. LFM 50 KPa Heights/Vorticity 12 hour forecast valid 12/11/79 0Z (12/10/79 1700 MST).

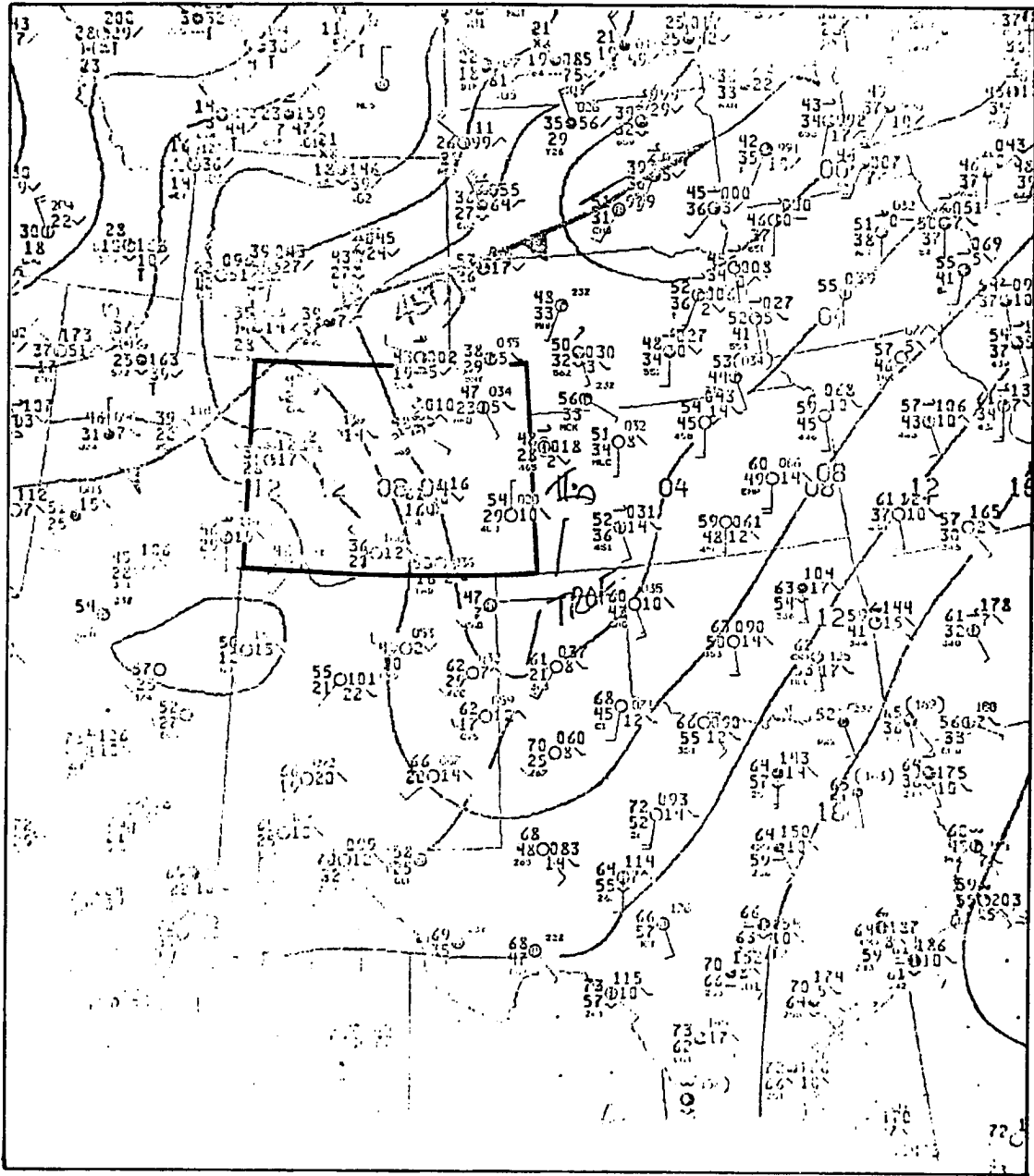


Fig. II-13 Case 5. 12/11/79 0Z (12/10/79 1700 MST) surface chart.

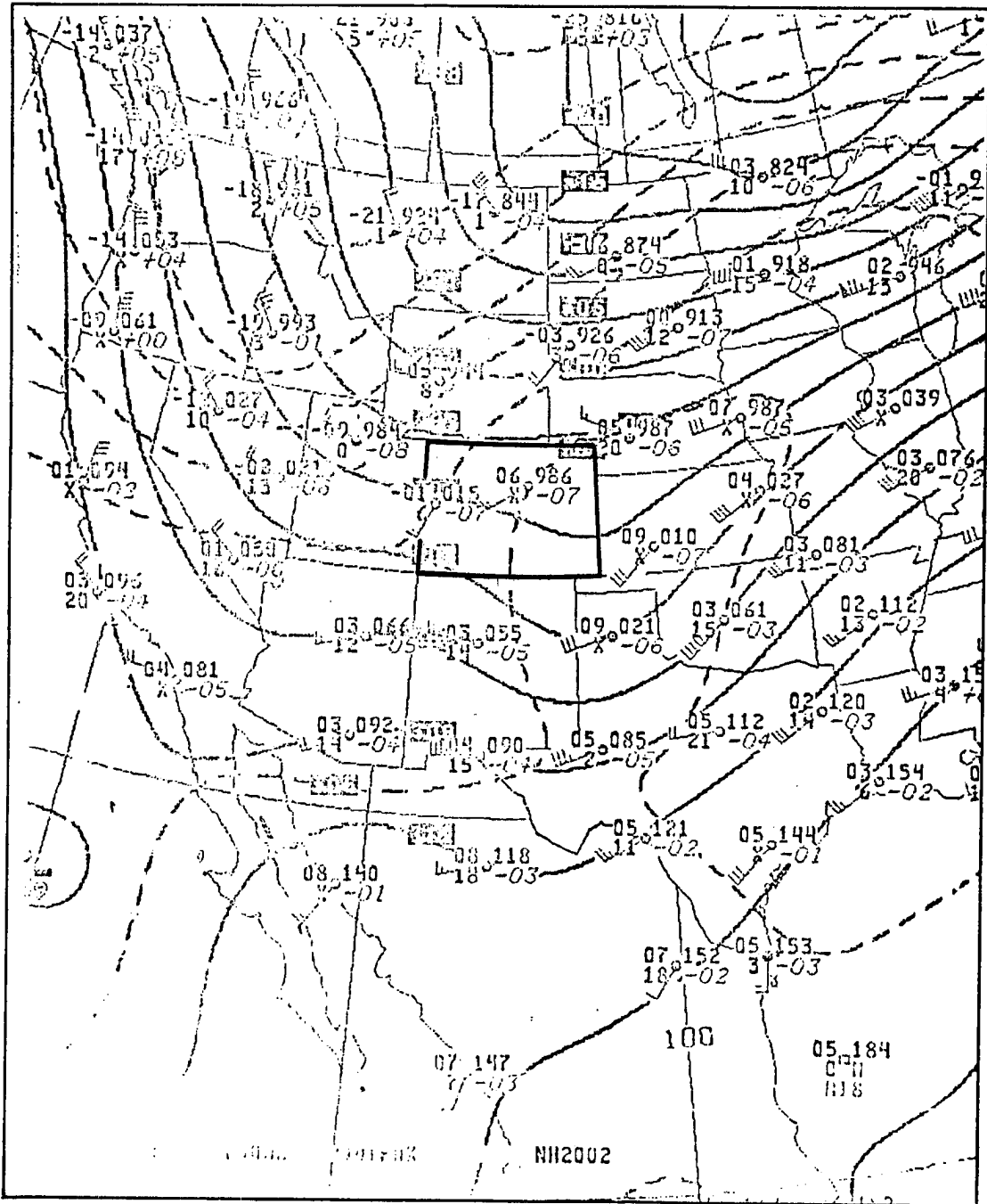


Fig. II-14 Case 5. 12/11/79 OZ (12/10/79 1700 MST) 70 KPa chart.

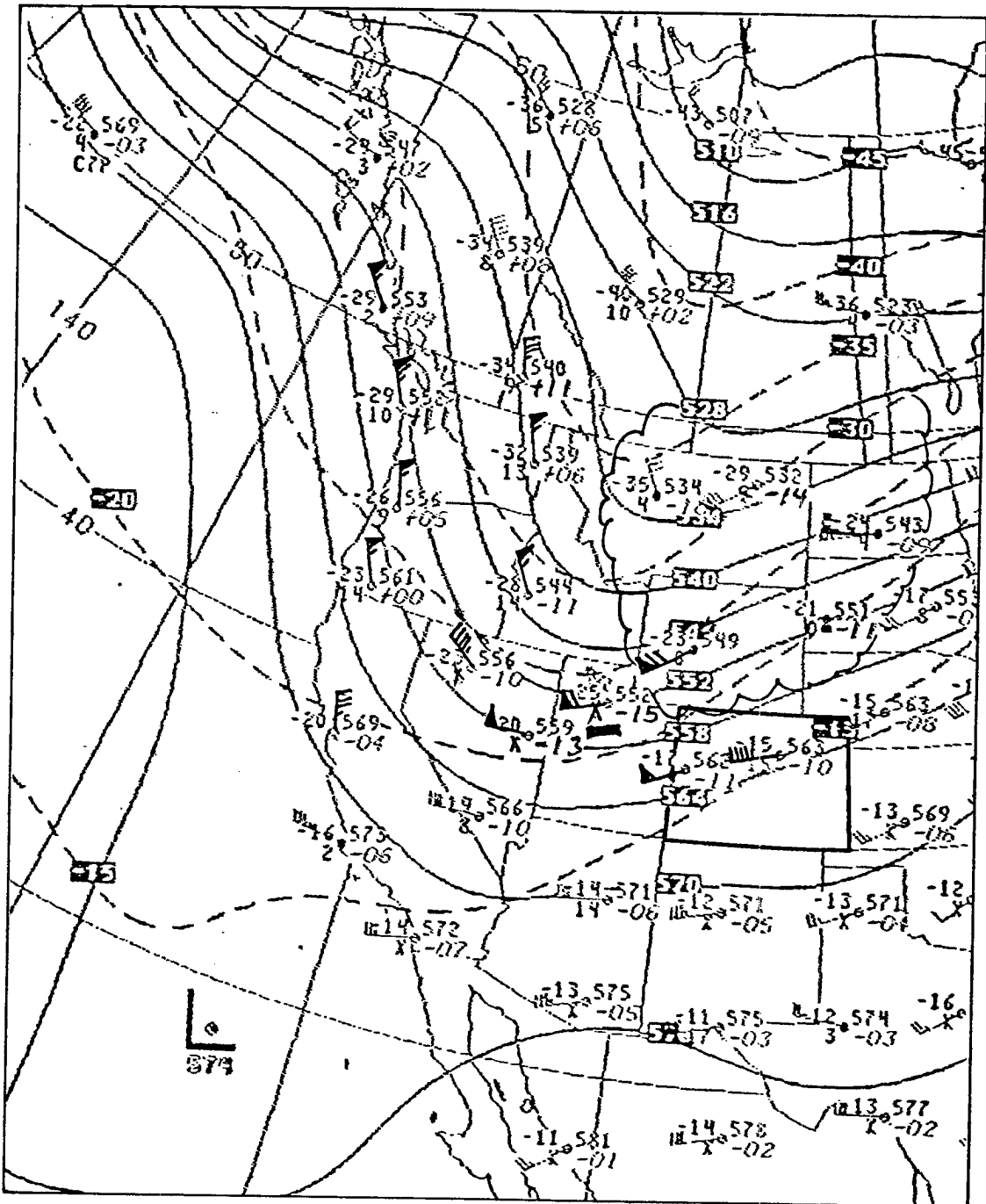


Fig. II-15 Case 5. 12/11/79 OZ (12/10/79 1700 MST) 50 KPa chart.

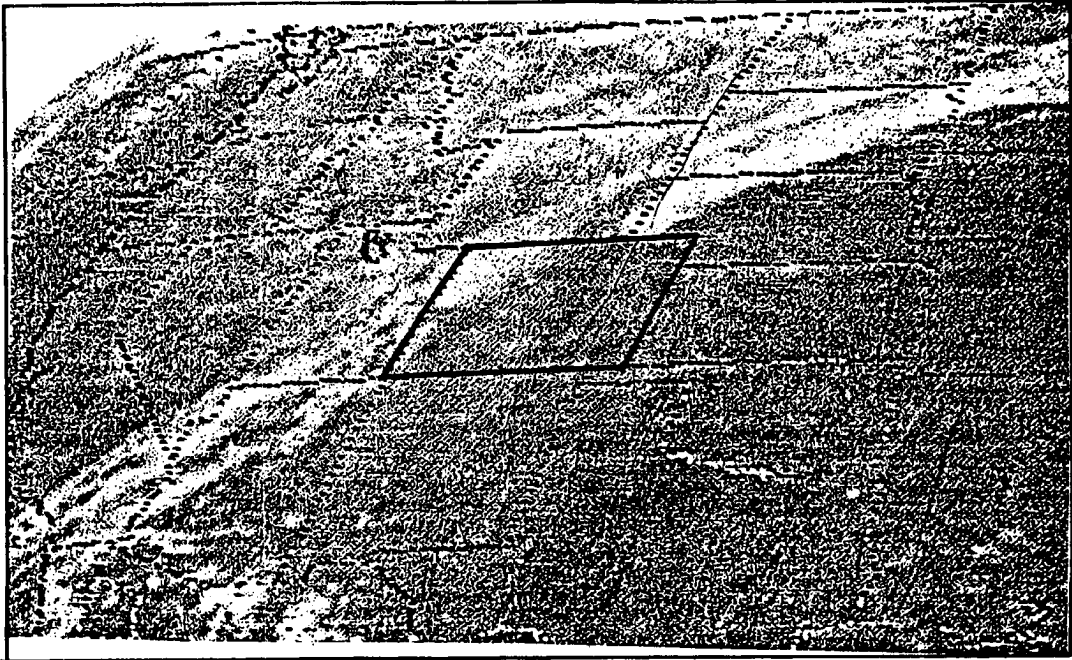


Fig. II-16 Case 5. 12/11/79 3Z (12/10/79 2000 MST) satellite photograph.

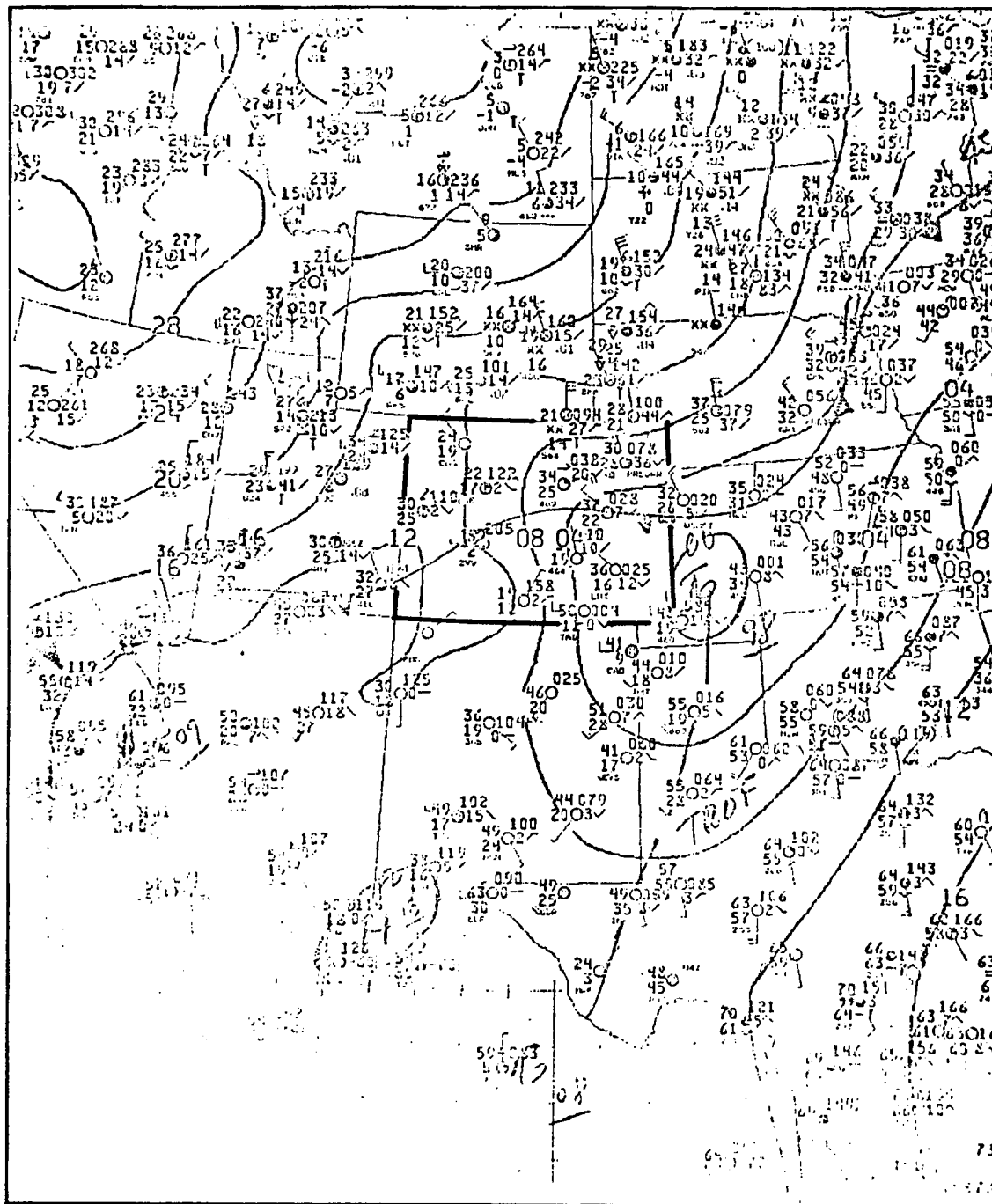
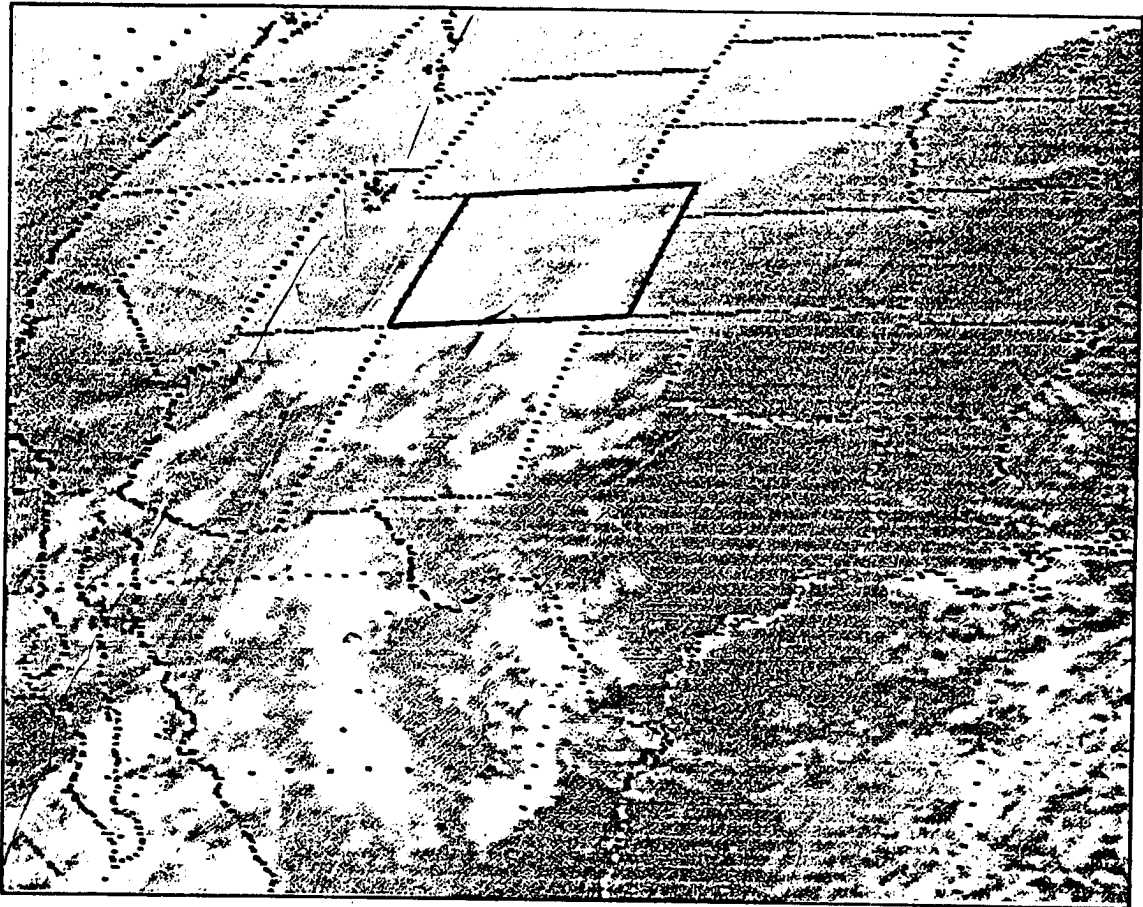


Fig. II-17 Case 5. 12/11/79 6Z (12/10/79 2300 MST) surface chart.





**Fig. II-19 Case 5. 12/11/79 12Z (12/11/79 0500 MST) satellite photograph.**



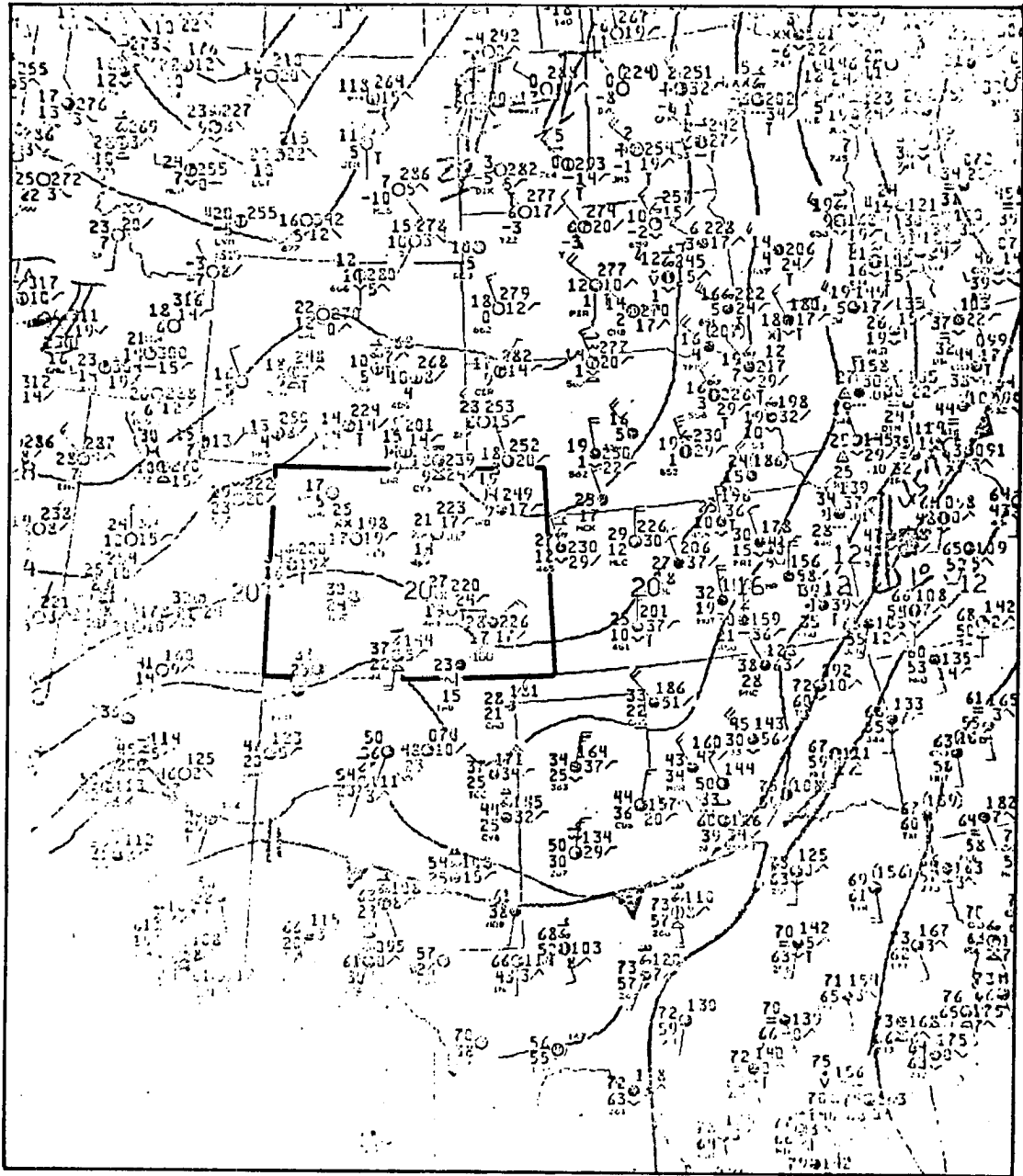


Fig. II-20 Case 5. 12/11/79 18Z (12/11/79 1100 MST) surface chart.

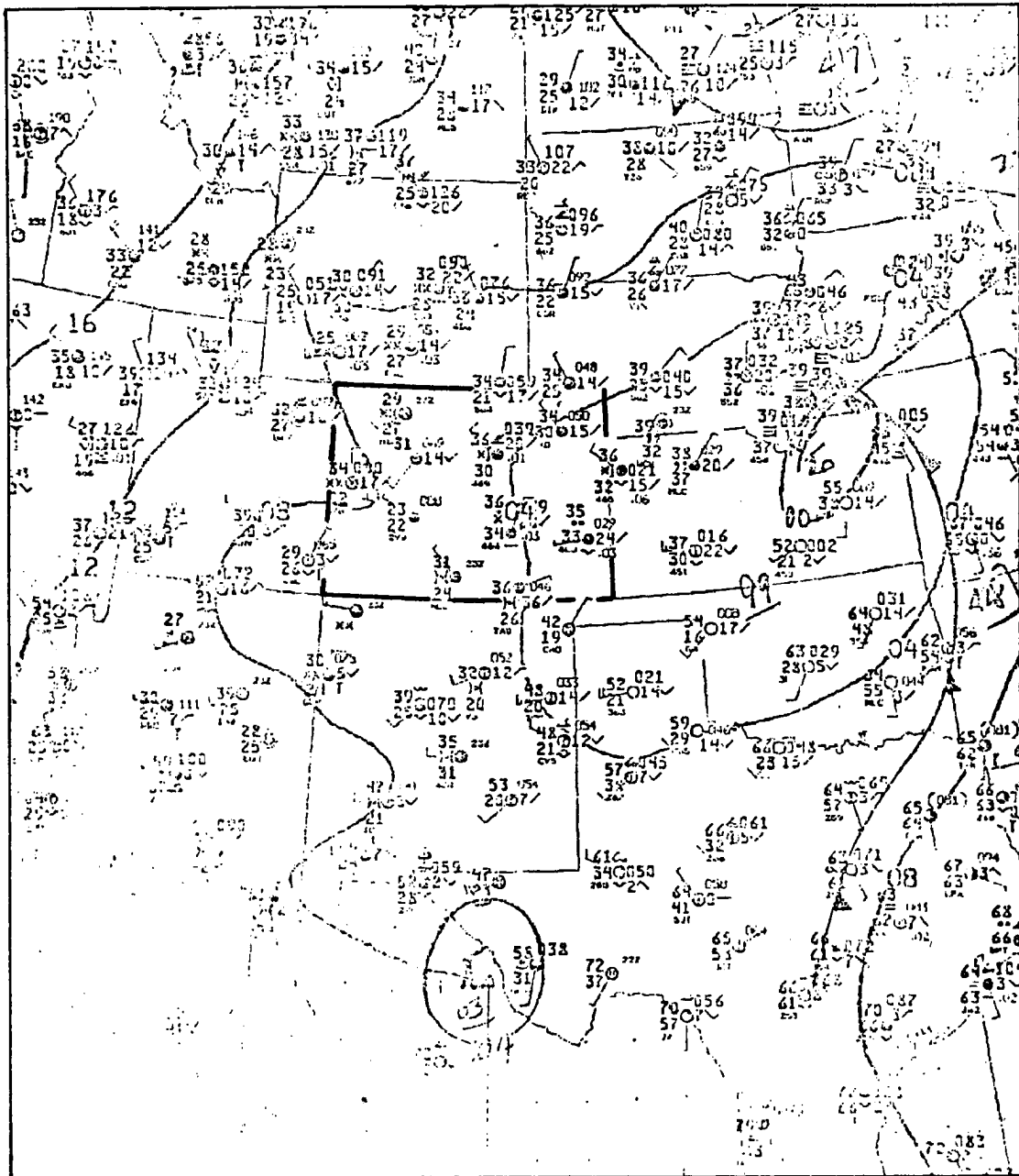
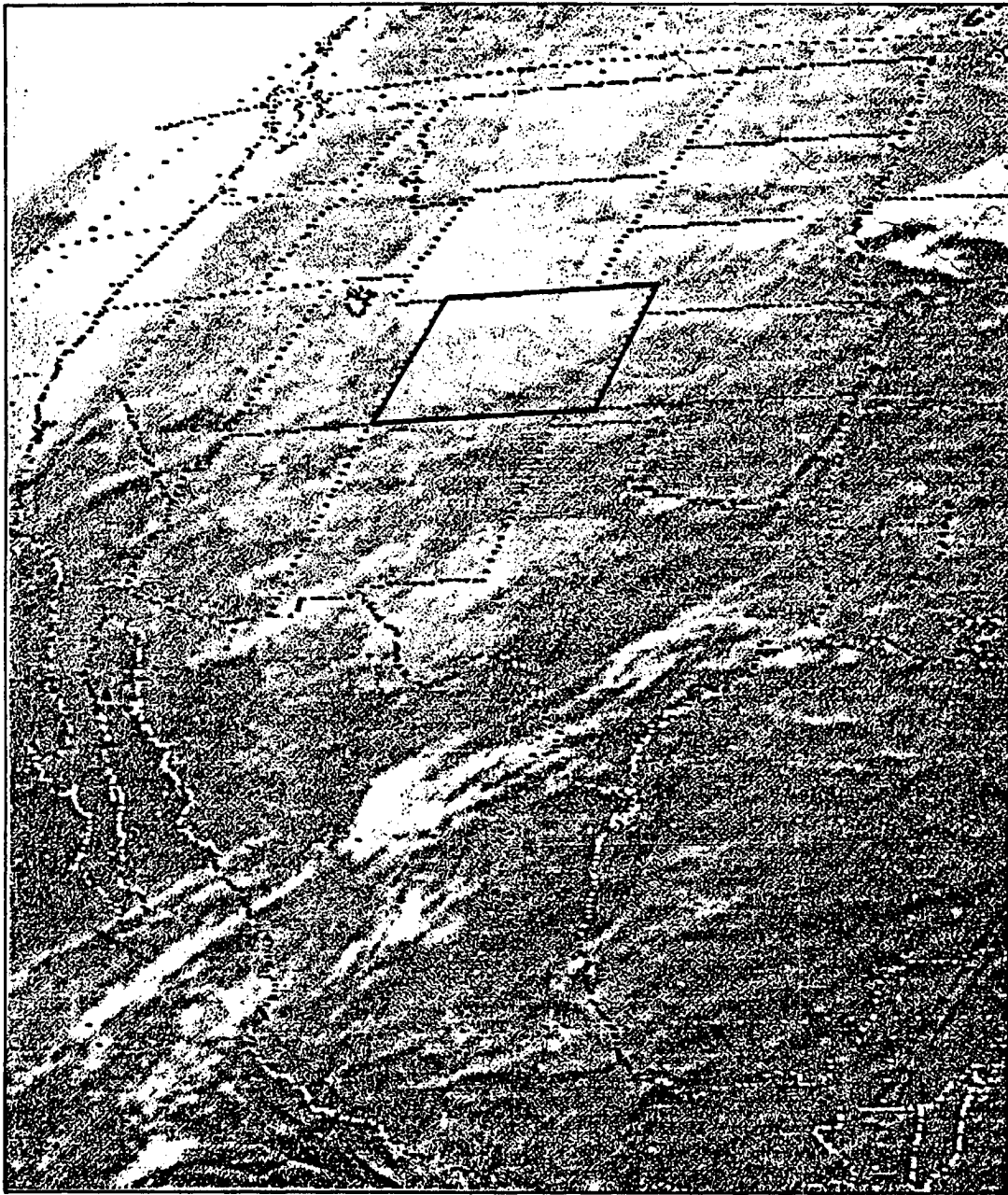


Fig. II-21 Case 6. 12/23/79 0Z (12/22/79 1700 MST) surface chart.





**Fig. II-23 Case 6, 12/23/79 3Z (12/22/79 2000 MST) satellite photograph.**

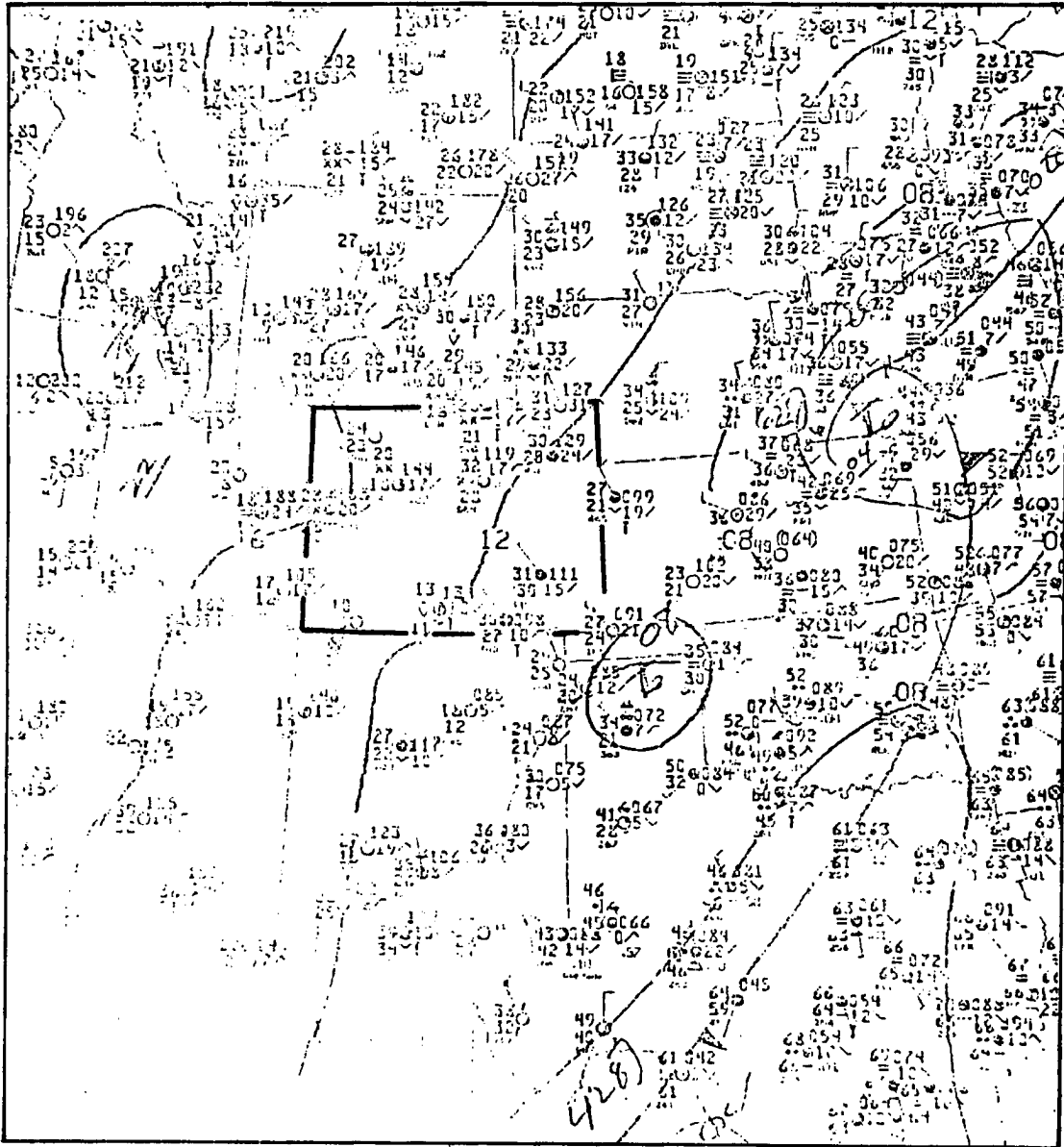


Fig. II-24 Case 6. 12/23/79 12Z (12/22/79 0500 MST) surface chart.

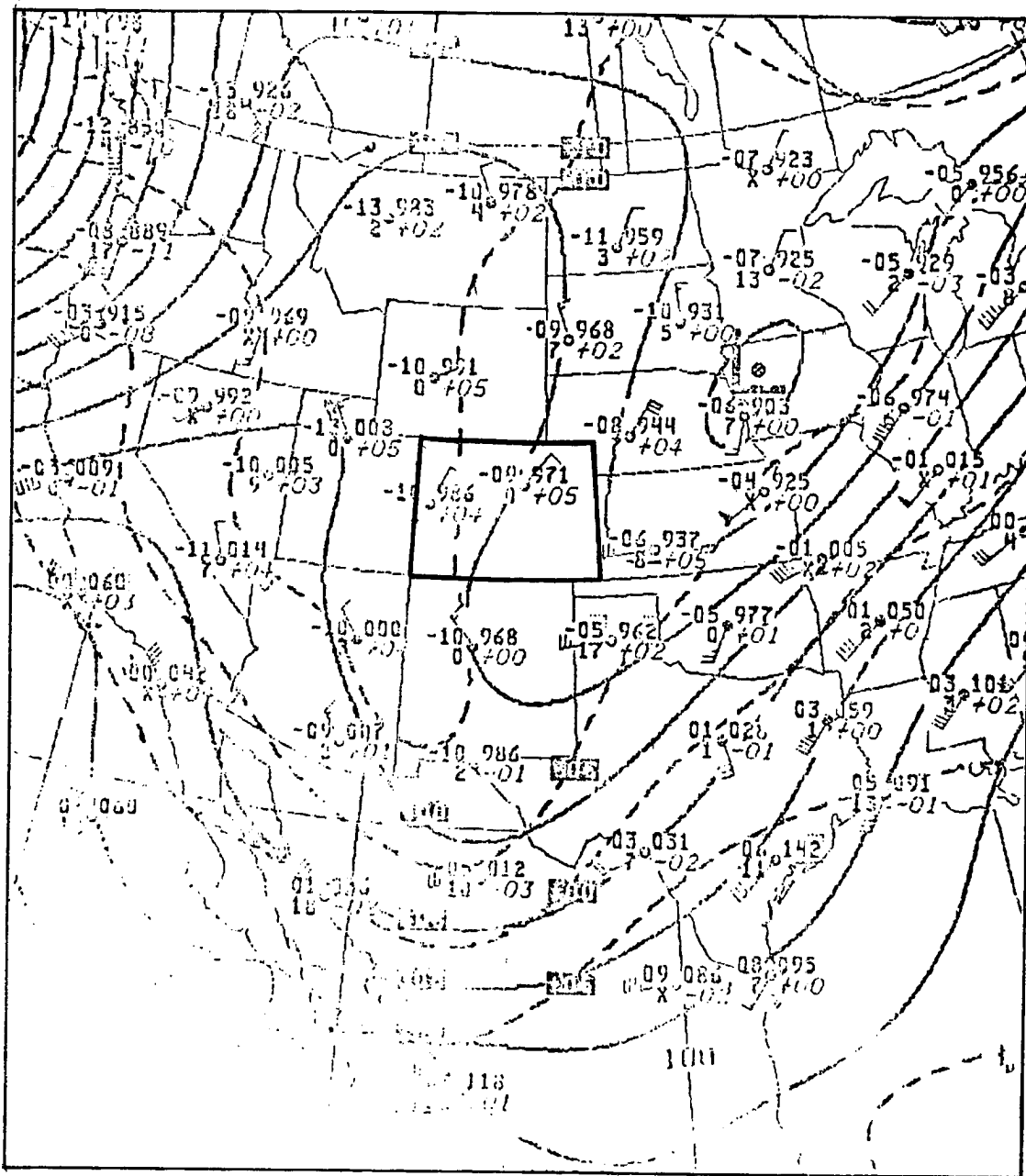


Fig. II-25 Case 6. 12/23/79 12Z (12/23/79 0500 MST) 70 KPa chart.

### Appendix III

#### Description of the Model Used for Objective 2. B.

The model used in estimating theoretical crystal fall velocity profiles in the absence of environmental motion is described in this section. Essentially, the model simulates the growth of a hex-plate crystal in an environment described by rawinsonde data taken at Craig (see Fig. 5) and monitors the fall velocity of the crystal as it falls from the level of Ku- radar detected cloud top height to ground level at the radar site (2075 m AGL). Although the model contains many assumptions and simplifications which may have been non-representative, it is probably adequate for the purpose of estimating non-dynamic crystal velocity components.

##### A. Choice of Habit

A single-habit growth mode was selected to simplify the model; although, in reality, the habit of crystal growth is highly dependent on the temperature of the growth environment. Cotton (1972) synthesized the work of Hallett and Mason (1958) and Kobayashi (1957, 1960) to produce the following relations:

Environmental Temperature (°C)	Crystal Growth Habit
0 > T > -3.0	Hexagonal plates
-3.0 ≥ T ≥ -5.0	Needles
-5.0 > T > -8.0	Prisms
-8.0 ≥ T > -12.0	Hexagonal plates
-12.0 ≥ T ≥ -16.0	Hexagonal plates, Dendrites
-16.0 > T ≥ -25.0	Hexagonal plates
-25.0 >	Prisms

Based on these relationships hexagonal plate growth was considered to be the most representative single habit for the cloud temperatures during the case described (12/10 - 12/11, 1979).

#### B. Basic Equations

Following Byers (1965), the mass added to a crystal growing by diffusion in the absence of riming and assuming the ventilation factor effecting thermal effusion to be unity can be described by the following equation:

$$\frac{dM}{dt} = 4\pi C(S_e - 1) G(T,P) \quad (1)$$

where  $dM$  is the change in crystal mass

$C$  is the capacitance factor

$S_e$  is the cloud saturation ratio

and  $G(T,P)$  is a thermodynamic function defined as follows

$$G(T,P) = \left[ \frac{M_w L_s^2}{K_i R_a T^2} + \frac{R_a T}{M_w D_v e_s(T)} \right]^{-1} \quad (2)$$

where  $M_w$  is the molecular weight of water



$L_s$  is the latent heat of sublimation

$K_i$  is the molecular thermal conductivity

$R_a$  is the gas constant of air

$T$  is the cloud temperature

$D_v$  is the diffusivity of water vapor in air

and  $e_s(T)$  is the saturation vapor pressure for the ambient temperature

For the model developed by Cotton (1972), the bulk density used for hex-plates was 0.9 and the capacitance factor for hex-plates was defined as follows:

$$C = \frac{ae}{2\sin^{-1}e} \quad C < 30\mu \quad (3a)$$

$$C = \frac{a}{\pi} \quad C \geq 30\mu \quad (3b)$$

where  $c$  is the length of the basal plane axis

$a$  is the length of the prism axis

and

$$e = (1 - \frac{c^2}{a^2})^{\frac{1}{2}}$$

The distribution of mass added to the growing crystal was governed by the following relation:

$$\frac{dc}{dt} = 0.12 \frac{da}{dt} \quad (4)$$

The equation used for the terminal velocity of an unrimed hex-plate was taken from Davis (1974)

$$V_t = 296.0 (a)^{0.824} \quad (5)$$

### C. Model Algorithm

The input into the model consisted of Ku-detected cloud top height for the period of interest, and temperature, pressure, and relative humidity for all mandatory and significant levels below cloud top height from the Craig rawinsonde.

A  $30\mu$  crystal was initially considered at the Ku-cloud top level. The crystal was simulated to fall at it's terminal velocity for 5 seconds then a new altitude position was determined. The growth environment for that altitude was determined by linearly interpolating temperature and specific humidity, and logarithmically interpolating pressure between the nearest altitudes for which rawinsonde data was available. The crystal was then simulated to grow for 5 seconds in that environment usng eqn. 1, and the change in the a axis was determined using eqn. 4. A new terminal velocity was calculated (eqn. 5) and outputted at every time step. The process was then repeated until the crystal was simulated to have impacted the ground. The resulting vertical profiles were then graphed for comparison with actual Doppler-radar observed crystal velocity profiles.

## Appendix IV

### CSU's APS-104 Ku-band Radar Calibration

#### Transmitted Frequency

To calibrate the radar frequency control settings on the Ku-band radar, output from an HP 628A Ku-band signal generator set for continuous wave at 1 watt was mixed with output from the APS-104 transmitter and displayed on an HP-180A oscilloscope. The frequency of the signal generator output was adjusted until the oscilloscope indicated 'zero beat' such that the mixed frequencies were identical. The procedure was repeated for each Ku-set frequency setting.

RF Tuning Setting	Transmitter Frequency (GHz)
000	17.50
100	17.36
200	17.22
300	17.08
400	16.94
500	16.80
600	16.78
700	16.54
800	16.40
900	16.30
1000 (max cw)	16.20

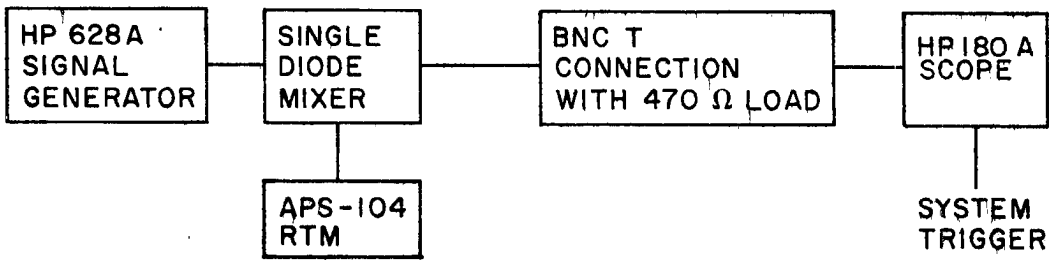


Fig. IV-1 Set up for APS-104 Frequency Calibration.

### Local Oscillator

A similar signal mixing routine was used to calibrate the Ku radar's local oscillator frequency. Radar signal was drawn from the Air Tube part which allowed Local Oscillator leakage to be sampled.

Repeller settings were adjusted at each local oscillator setting to maximize crystal current.

LO Setting	Optimum Repeller Settings	Frequency (GHz)
000	1000/370	17.10
100	800/320	17.00
200	1000/040	16.90
300	820/240	16.75
400	850/040	16.64
500	720	16.50
600	850	16.41
700	700	16.30
800	770	16.21
900	600	16.08
1000	700	16.02

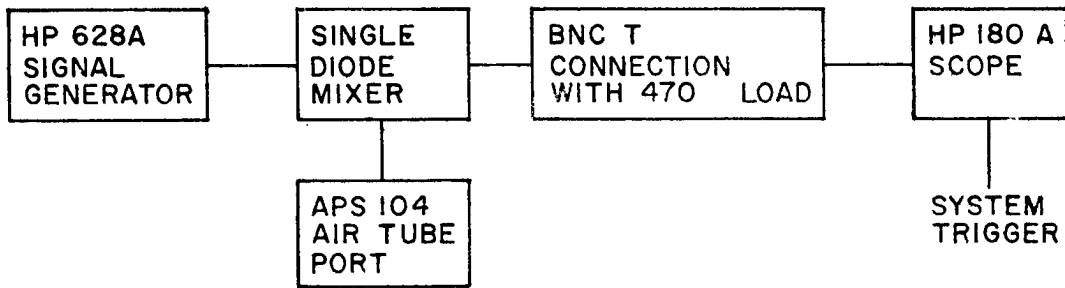


Fig. IV-2 Set up for APS-104 Local Oscillator Calibration.

#### Receiver

The HP-628A signal generator was used at frequency setting 16.67 GHz transmitting at 1 mW cw to inject signal directly into the receiver complex after passing through an in-line 10dB attenuator. After passing through the IF amplifier, the power was sampled using an HP 2401 C Integrated Digital Volt meter. After passing through the A/D convertor, the integrator buffer was then dumped from the computer. In this way the digital values recorded by computer could be compared with the actual power received at the feedhorn. The process was then repeated as the source power was progressively attenuated.

Transmitted Power (dBm)	IF Power (mv)
-20	2603
-25	2503
-30	2352
-35	2203
-40	2063
-45	1941
-50	1810
-55	1680
-60	1550
-65	1414
-70	1286
-75	1167
-80	1037
-85	916
-90	804
-95	725
-100	685
-105	655
max attn.	654
off	654

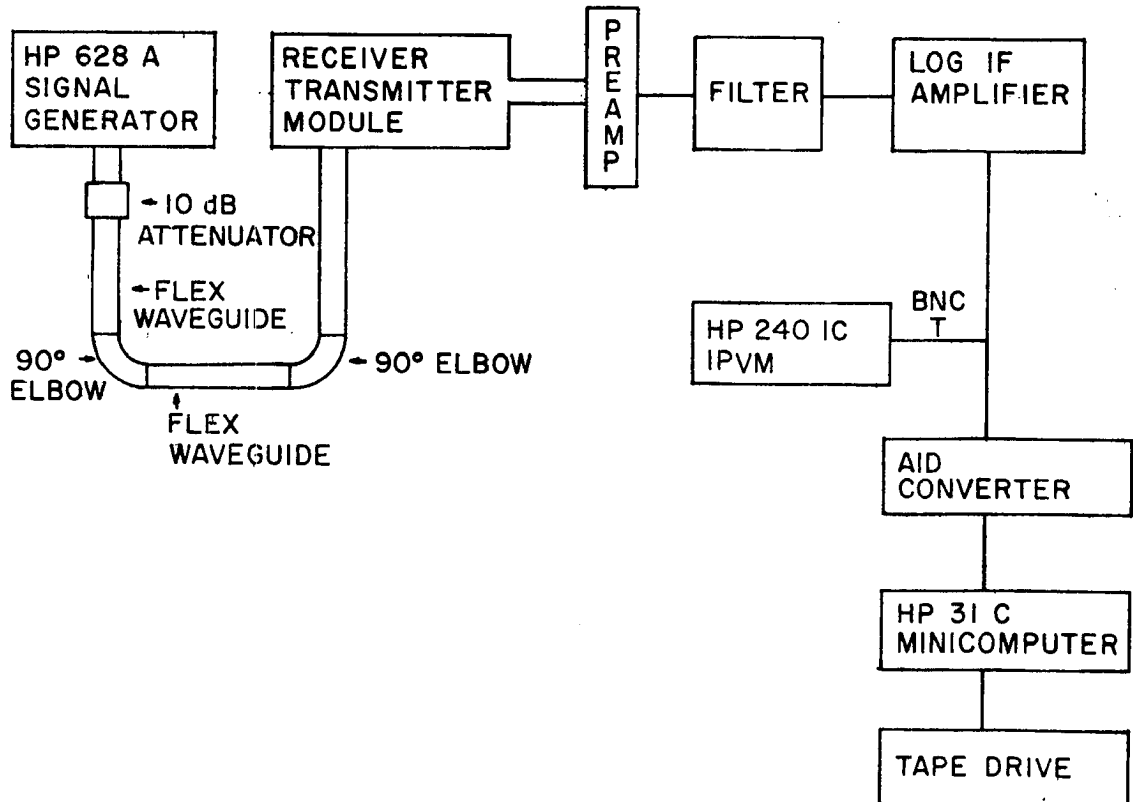


Fig. IV-3 Set up for APS-104 Receiver Calibration.

### Dish-Feedhorn complex

The HP-628A signal generator was fit with a 15 dB broadcast horn tilted downward at an angle at  $26.3^{\circ}$  from horizontal, and set to maximum output in continuous wave mode. The generator was then mounted on a mobile platform on NOAA's Boulder Atmospheric Observatory's meteorological tower and elevated so that the beam would be intercepted by the Ku-band radar dish approximately 500 m from the other at the ground. At that point, the signal was intercepted by a standard 15 dB feedhorn pointing toward the signal generator and guided into the receiver system. The received signal was then monitored as it emerged from the IF amplifier by the HP 2401C Integrated Digital Power meter. The wave feedhorn complex with an in-line attenuator, and the dish oriented to receive maximum power. The signal from the dish-feedhorn complex was then progressively attenuated until the power meter indicated equivalent received power with the previous test. The attenuator setting corresponded to the gain above 15 dB attributable to the dish-feedhorn complex. In this manner it was determined that dish and feedhorn provided 49.8 dB gain.



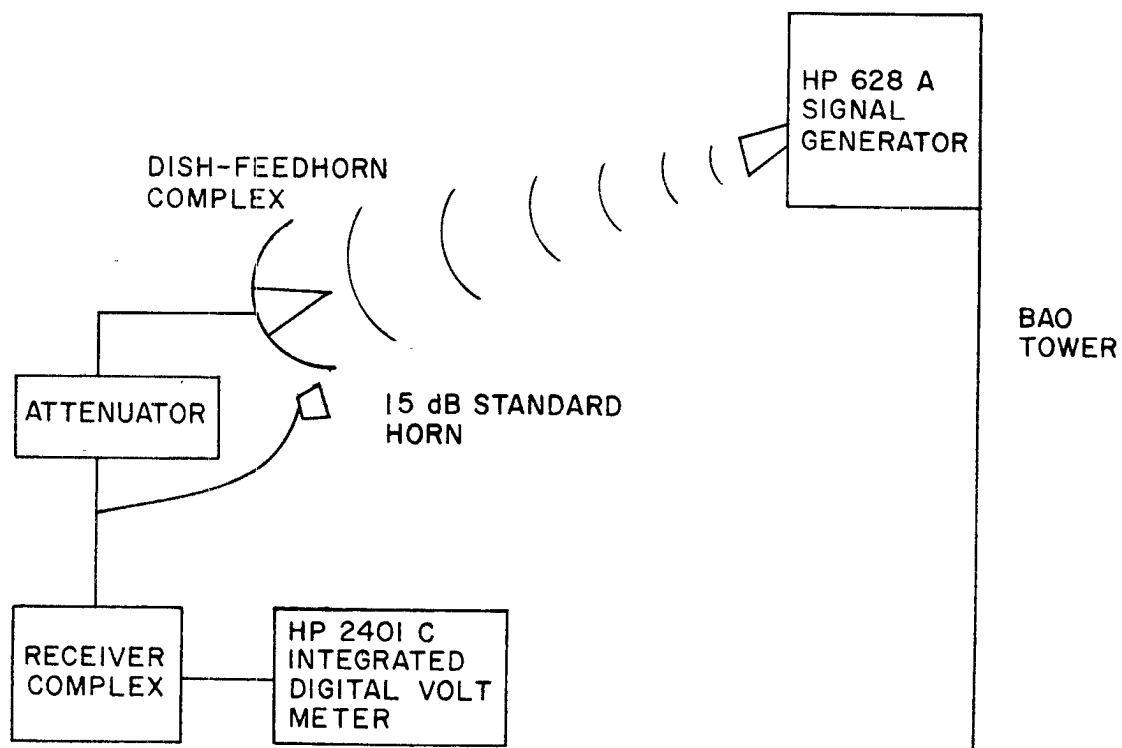


Fig. IV-4 Set up for APS-104 Dish-Feedhorn Complex Calibration.